Summer 9-1-2014

Large-scale Cellular Imaging of Neuronal Activity: a Study of Neural Individuality and a Method for Imaging Mouse Cortex

Pei Sabrina Xu
Washington University in St. Louis

Follow this and additional works at: https://openscholarship.wustl.edu/etd

WASHINGTON UNIVERSITY IN ST. LOUIS

Division of Biology and Biomedical Sciences

Neurosciences

Dissertation Examination Committee:
Timothy E. Holy, Chair
Yehuda Ben-Shahar
Joseph P. Culver
Erik D. Herzog
Karen L. O'Malley
Paul H. Taghert

Large-scale Cellular Imaging of Neuronal Activity:

a Study of Neural Individuality and

a Method for Imaging Mouse Cortex

by

Pei Sabrina Xu

A dissertation presented to the
Graduate School of Arts and Sciences
of Washington University in
partial fulfillment of the degree
of Doctor of Philosophy

August 2014
St. Louis, Missouri

CONTENTS

LIST OF FIGURES

vi

ACKNOWLEDGMENTS

A PhD that easily takes us six years in the gold time between twenty to thirty is one of our most important decisions in the whole life. Now when I look back my past six years, I feel fortunate about my decision of moving here and joining in this program and this laboratory to pursue my PhD. It brings me to the fascinating sciences as well as happy life on each single day even when somethings go awry. I know that is because of a group of wonderful people that I meet here, and I sincerely thank them for all their help.

First, I appreciate the patient guidance from my advisor Professor Tim Holy. Working with him exposed me to a wide range of science from olfaction, imaging to computation; without the time and effort he devoted into my study, I would not be able to complete this dissertation. I am especially grateful for his enthusiasm to share and carefully explain good things in work and even in life to us. I not only benefit from the specific skills and ideas he shares, but also learn an altitude that will positively influence me in my life. Thanks to Tim for giving me support as well as considerable freedom in research, which helps me learn to be independent and also preserve the original curiosity and imagination in science.

I am grateful to my thesis committee. They always gave me constructive suggestions in my update meetings, which helped consolidate my research data along the way towards publication. In the meantime their critiques helped me grow more mature in research. When I was facing difficulties, I also got strong support from my committee.

An unexpected encounter with Professor O'Malley outside campus brought me plenty of extra insightful words. My lovely professors not only teach me in sciences, but also help be me become confident and independent in life.

My PhD study never got boring because of the accompany of all the members of Holy lab. Thanks to this large family. Thanks to everyone for giving me valuable suggestions. I also want to specially thank Diwakar Turaga, Ningdong Kang, Xiaoyan Fu for training me in special techniques, Kara Janiszak for taking care of my mice, and also Donghoon Lee who helped me treat mice when I was out of town. Particularly, two undergraduate students Mark Xu and Jack Chong helped me collect a portion of the behavioral data. Without their hard work on the nights in SIRF-west, I would not have accomplished everything presented in this dissertation. I also remember those days and weekends when I worked together with Zhongsheng Guo and Jian Wang to make the computer software control the newly developed microscope. On the new microscope, I am also collaborating with Maiko Kume in the mouse brain imaging. Thanks for their collaboration.

My acknowledgments also go to people of the WashU community. Yue Yang from Bonni lab and the members of the Kerschensteiner lab gave me valuable feedback when I presented my work in joint lab meetings. Tracy and Water at East McDonnell, and Eric and Wendy in SIRF-west provided superior technical support for my mice housed in the unconventional stacking-cages. John, Charlie and David in the machine shop made the custom parts for optics and mouse cages for my research. Dr. Kelly Monk gave me the HuC:GFP zebrafish for imaging. The Cavalli lab provided the space and technical help when I worked on ESP-1 purification. Dennis Oakley in the Bakewell neuroimaging

ABSTRACT OF THE DISSERTATION

Large-scale Cellular Imaging of Neuronal Activity:

a Study of Neural Individuality and

a Method for Imaging Mouse Cortex

by

Pei Sabrina Xu

Doctor of Philosophy in Biology and Biomedical Sciences

in Neurosciences

Washington University in St. Louis, 2014.

Associate Professor Timothy E. Holy, Chair

The brain contains an enormous number of neurons with diverse gene expression, morphology, and connectivity. These neurons exhibit distinct activity in the course of behaviors. The study of neural coding of a specific behavior necessitates recording activity from multifarious neurons in the circuit.One appealing approach is to simultaneously image the activity of a very large neuronal population at cellular resolution. However, recording calcium signals from tens of thousands of neurons at one time is not trivial. The gold standard technique, two-photon laser-scanning microscopy, typically permits recording from hundreds of neurons. Recently, we developed objective-coupled planar illumination (OCPI) microscopy, which uses thin sheets of light to image whole volumes of $\sim 10,000$ neurons within 2 seconds. My dissertation includes an application and a further methodological development of such a fast large-scale imaging technique:

1) Large-scale functional imaging reveals **individuality, dimorphism, and plasticity of mouse pheromone-sensing neurons.** Different individuals exhibit distinctive behaviors, which is presumably attributed to the neuronal differences between brains. However, studying neural individuality, especially at the level of the function of single neurons, requires an effective approach to measure cellular activity of a diverse neuronal population in a circuit. Here using OCPI microscopy, I performed calcium imaging of pheromone-sensing neurons in the intact mouse vomeronasal organ. Exhaustive recording enabled robust detection of 17 functionally-defined neuronal types in each animal. Inter-animal differences were much larger than expected from random sampling, and different cell types showed distinct degrees of variability. One prominent difference was a neuronal type present in males and virtually absent in females, and animals exhibited a corresponding dimorphism in investigatory behavior. Surprisingly, this dimorphism was not innate but generated by plasticity, as exposure to female scents led to both the elimination of this cell type and alterations in behavior. The finding that an all-or-none dimorphism in neuronal types is controlled by experience—even in a sensory system devoted to "innate" responses—highlights the extraordinary role of "nurture" in neural individuality.

2) A new generation of OCPI microscopy enables unprecedented **large-scale *in vivo* imaging of mouse brain activity by light-sheet microscopy.** I have built a new variant of OCPI microscope, horizontal scanning objective-coupled planar illumination (hsOCPI) microscope, with enhanced imaging volume and speed by ~ 15 fold compared to OCPI, thereby capable of recording $\sim 100,000$ neurons simultaneously. Using this technique, I imaged the entire nervous system of the larval zebrafish (including the

spinal cord) and a square-millimeter patch of mouse cortex *ex vivo*. The miniaturized optics around the specimen allowed *in vivo* imaging through a cranial window of a head-fixed mouse. This technique is the first application of light-sheet microscopy in calcium imaging of mouse cortex *in vivo*. The exceptional large-scale sampling of cortical activity with cellular resolution should usher new insights into the functions of brain circuits.

Chapter 1

Introduction

1.1 The motivation to record large-scale neural activity with cellular resolution

We are fascinated by the *brain* because it is the physical basis of our mind. It processes information we receive to form perceptions, sends commands to generate movement, stores our memories, harbors intelligence and emotion, etc. In order to understand how these neural events are created and unfold, a straightforward approach is looking into the brain to see what is there (structure) and what happens (activity).

1.1.1 An ongoing but urgent mission: recording neuronal activity

Knowing the brain structures provides the prerequisite to investigate brain activity. From the legendary Cajal drawings of brain cells with delicate arborizations, to the modern synaptic connectome of C. elegans [1, 2] and more recently of mouse miniature circuits [3, 4], our comprehension of the static brain structure promises to be accomplished in only a matter of time. On the other hand, for each neuron in the brain, it

is the precise pattern of electricity coursing through it at a given time that determines what it is actually doing. Since the birth of the Hodgkin and Huxley model [5], electrophysiologists [1] have made marvelous findings regarding neuronal activity, complemented with the growing imaging-based techniques. However, a major challenge still exists for the study of dynamic brain activity. It has been highlighted as a new Presidential focus, namely the BRAIN (Brain Research through Advancing Innovative Neurotechnologies) Initiative by the Obama government in February 2013.

1.1.2   Why we need recordings from large numbers of cells

The brain contains an enormous number of neurons. In the human brain, that number is at the level of a hundred billion. To examine the activities of those neurons, one can look at one neuron at a time or a population of neurons simultaneously. Now we are driven towards the latter direction, for several plausible reasons as listed below.

- Neurons do not operate individually. They are wired together — sequentially or laterally connecting to each other to form circuitry. During the course of a neural event, from the input to the output of the circuitry, there is a sequential neuronal activation pattern. Ideally, if one knows the precise timing, duration and amplitude of each individual neuron's responses throughout the event, one can delineate the circuit design, understand the computation, and thereby ultimately decipher the "biological intelligence." It is noteworthy to mention that a pure map of the static structure of the circuit is not sufficient to predict how the signal is flowing among

---

[1]To be precise, electrophysiology predates the birth Hodgkin-Huxley (HH) model. Galvani discovered the neural electrical activity in the 1790s [6]. Another typical example is that Hartline performed the extracellular recording of individual retinal ganglion cells in the 1930s, which is still 20 years earlier than the HH. Yet the mathematical HH model is a theoretical pillar of modern neurophysiology.

the neurons. The structure of synaptic/electrical connection does provide insight about the signal transmission locally at *the* connection, but not necessarily over multiple relay stages. In fact, the nonlinearity of the neural circuit introduced by the inhibitory connections makes that task almost impossible. A typical example is that after the C. elegans connectomic structure became available [2], there was still a need for functional connectomic study to map the activity pattern in order to understand how those 302 neurons work together.

To obtain the sequential activation pattern, in theory, one can record individual neurons one by one by repeating the same event multiple times, and then pool all the responsive neurons together and recapitulate the information flow according to the distinctive time delayed. However, even if one dared to set off that time-consuming adventure, there is another immediate challenge — the activation delays are at the level of millisecond or even smaller, and the variation of timing system in each recording will inevitably introduce inconsistency for the pooled neurons. The advantage of recording simultaneously is that systematic timing deviation will be consistent for all the neurons, and one-time recording of a large number of neurons is a much more efficient approach.

- Empirical evidence suggests that neuronal activities are not that "reproducible". Although the trial-to-trial variation has been treated as "noise" for decades, emerging awareness of the existence of waves, synchrony, and oscillation in circuits has changed the view. On the one hand, one can not deduce these features by examining the activity of individual neurons; on the other hand, one-by-one measurement of many individual neurons will not detect these holistic phenomena that only

3

happen at particular times. Therefore, one has to gain the dynamic activity patterns of a sufficient number of neurons simultaneously to evaluate the population features.

- Neurons in the circuit are *heterogeneous*. The "type" of a given neuron can be defined by the genetic identity (gene expression), wiring identity (connection), and functional identity (response). It turns out that, no matter how the type is defined, diverse types, easily more than one hundred, co-exist in a local circuit, normally spatially distributed without an explicable pattern. All theses neurons are typically co-activated in the circuit, requiring *cellular resolution* to extract activity patterns of individually distinctive neurons. For a particular neural type, the initial discovery of the type necessitates a sufficient number of those particular neurons, which must come from an exhaustive sampling.

1.1.3 Potential recording approaches

During the past half century, the most feasible approach is recording the activity from a single neuron at a time, like whole cell recording, or up to tens of neurons using multi-electrode single unit recording. The recent imaging-based approaches like calcium imaging allow investigators to sample hundreds to thousands of neurons simultaneously. Other approaches like fMRI, as well as optical imaging based on slow, intrinsic signals, such as haemodynamic or light-scattering signals [7], are able to record large-scale population signals, but they lack cellular resolution. Nowadays, electrode recording and fluorescent imaging approaches represent the most practical methods for cellular recording of neural activity. Focusing on the theme "how many cells they can record," each

technique will be introduced, and the strengths and limits of each technique regarding temporal/spatial resolution and potential for improvement will be also covered.

Electrode-based methods

The nature of the neuronal activity is the change of membrane potential, which generates electrical signals capable of transmitting among cells in a circuit. This electrical activity was first discovered by Galvani over 200 years ago [6]. Since then, the natural way to record activity of neurons is by instruments capable of measuring the electric changes. Since the electrophysiologists were able to obtain reliable signals from each single neuron, they have been working in different ways to increase the number of neurons in a recording. Here are the two most commonly used techniques:

Whole-cell recording Whole-cell patch-clamp recording is currently the most precise away to query intracellular ion activity of a neuron. The unprecedented sensitivity and temporal resolution allow one to study the "smallest" changes associated with neuronal activity, like the single ion channel action, quantal events of synaptic transmission ("minis"), etc. In patch-clamp experiments, each glass electrode is controlled by an individual manipulator, so the space around the tissue limits the number of electrodes that can be placed there. It is said that a 12-electrode setup can be managed, and the reported maximum number of successful simultaneous whole-cell recordings is 7-8 neurons [8]. Although robotic patch-clamping is being developed, due to the spatial constrains, it will be hard to increase that record further.

Single unit recording Extracellular recording of neurons normally detects the "compound" electrical activity of multiple neurons around the electrode [2]. However, the mixed signal can be "separated" to extract signals from individual neurons. Basically, the more electrode probes, the more cells one can detect. To increase the number of probes, a multi-electrode array that arranges up to 256 electrodes laterally can be used for flat neural tissues. For deep neurons that require insertion of the shank-shaped electrode, one can increase the number of probes arranged in a single shank or even increase the number of shanks in the assembly. The most recent silicon electrode assembly contains 512 probes, which covered ~ 1000 neurons within a radius of $140\,\mu$m area in the rat cortex, and successfully recorded 163 neurons simultaneously [9]. One can infer the rough spatial distribution of all these neurons according to the probes' position in the recording. One of the major limits is that the signals from adjacent neurons are normally impossible to obtain in this recording, because they are most likely "mixed" together in the same probes. On the other hand, the challenge to compact thousands of electrodes in a miniature device also restrains the further increase of the electrode number.

Temporal resolution of the electrode-based approaches is simply determined by the readout rate of electronics that can be easily achieved at 10KHz level. This sampling rate can sufficiently capture the dynamics of action potential that normally lasts for milliseconds. The merit of high temporal resolution makes electrode-based techniques the most favorable tool when timing information is of most concern, such as dynamic rhythm or noise analyses. However, the intrinsic limits on the cell number and lack of spatial information limit its potential in large-scale recording.

---

[2]The purity of signals is related to the size of the electrode tip.

Fluorescence imaging-based methods

The nature of electrical activity has driven generations of neuroscientists to invest immense effort to build electric instruments to record changes in membrane potential. In the meantime, a minority of investigators also took advantage of voltage-sensitive dyes (optical membrane-voltage probes) to detect membrane potential changes by means of imaging. Similarly, the discovery of calcium fluctuation during the action potential and the availability of calcium fluorescent indicators, drove the rapid advancement of imaging approaches for recording neuronal activity. Nowadays many laboratories use fluorescence imaging-based methods to routinely measure the activity from tens and hundreds of neurons [10]. Combining the most state-of-the-art fluorescent probes with optical instruments with high speed and large field-of-view, a recent study achieved whole-brain imaging of neural activity of an organism [11–13].

Besides the remarkable advantages regarding the number of neurons, compared with electrode-based approaches, optical recording is minimally invasive. It avoids physical contact to neurons, though the potential for interference with cellular function due to calcium buffering. It is noteworthy to mention that the superior temporal resolution of electrode-based techniques is generally hard to beat. Although current functional indicators are fast and sufficiently sensitive to single action potentials, and fast optics allow sampling at millisecond resolution, yet that is attained with considerably compromised spatial capacity. In a typical population calcium imaging experiment, tens to hundreds of neurons are sampled every 2-3 seconds to follow the calcium fluctuation.

The detail of using fluorescent imaging approaches to measure neural activity will be introduced in the next section.

1.2 Large-scale fast fluorescent imaging

The implementation of fluorescent imaging of neuronal activity necessitates two elements: a fluorescent indicator that reports activity of the cells, and a microscope that detects the fluorescence change. With the aim to record many neurons in a circuit at high speed over periods of minutes to hours, I will focus on the most advanced indicators and imaging technologies that meet, or have promise to meet the goal. Additionally, as the enormous growth of imaging volume (cell number) as well as recording time, the imaging data size has reached a level that greatly challenges our capability to handle big data, as briefly touched on at the end of this section.

1.2.1 Fluorescent indicators of neuronal activity

Back in the 1970s, two categories of chemical dyes were introduced to neuroscientists for monitoring neuronal activity. One is merocyanine dye that senses voltage changes [14]; the other one is a synthetic compound based on the well-known chelator EGTA, capable of detecting free calcium, namely BAPTA (1,2-bis(o-aminophenoxy)ethane-N,N,N',N'-tetraacetic acid) [15]. Upon voltage change or calcium bindings, both dyes increase their quantum yield of fluorescence, thereby allowing quantitative [3] imaging of neuronal activity.

Inspired by the chemical-based indicators, with the idea of fusing a voltage/calcium sensor with a fluorescence reporter, a series of protein-based indicators have been developed, namely genetically encoded voltage indicator (GEVI) and genetically encoded

---

[3] For quantitative measurement, one would prefer sensors with a linear relationship between fluorescence response and firing activity [16]. Nonlinearity in sensor can prevent precise spike quantification during action potential bursts [17].

calcium indicator (GECI). Many different calcium or voltage sensors have been discovered and used in designing new probes. As for the reporter, most of the GEVIs and GECIs adopt on of two strategies — either based on the single GFP's fluorescence change, or through fluorescence resonance energy transfer (FRET) between two fluorescent molecules. One exception in the recently developed voltage indicator Arch, a microbial rhodopsine protein derivative, that itself is responsible for both voltage sensing and fluorescent emission.

For population cellular recording, currently the most commonly used probes are the calcium indicator GCaMP series. The GCaMP protein consists of a calcium-binding domain from calmodulin (CaM), a short linking region called M13, and a circularly permuted enhanced GFP (cpEGFP). On calcium binding, the conformational changes in the calmodulin-M13 [4] complex induce the fluorescence changes of GFP. Based on this same general structure, in the past decade, mutations at certain amino acids that changed the protein properties [5], especially those that remarkably enhanced the extent of fluorescence change, produced different generations of GCaMPs. While larger fluorescence change normally means higher signal-to-noise ratio, a definite merit in physiological recording, along with that regard, there are multiple factors that need to be considered to choose the right indicators [6] for imaging neuronal activity at large-scale and cellular resolution.

---

[4]M13 is the conformational actuator that is fused between CaM and GFP to enhance the conformational change and induced fluorescent signal.

[5]Properties like calcium binding affinity and kinetics, the extent of binding induced protein conformational change thereby fluorescence change, baseline GFP fluorescence level, dynamic range of the fluorescence etc..

[6]A detailed guide for GECI selection in different application has been reviewed by Hires et al. [18] and Tian et al. [19].

Delivery   A chemical-based indicator has to be experimentally delivered into the neurons right before the imaging, either by bulk loading ("multi-cell bolus loading") [20], or facilitated by electroporation [21] or "gene-gun" [22]. It is technically challenging to get a large population of neurons effectively and relatively equally labeled in those procedures [7]. On the contrary, a protein-based indicator can be introduced into the cells by transgenesis or viral constructs, so the labeling is much more efficient. Another advantage of genetic labeling is that it can target to specific neurons in the circuit that normally contain multifarious cells. At present, the Cre-dependent GCaMP transgenic mice and virus have been widely used in combination with existing Cre-lines [23], allowing specific recording from a variety of neuronal populations, and even within the specific subcellular compartments. It is worth noting that there are also studies that are beginning to look for strategy that allows facile targeting of dyes and drugs into specific cell classes [24, 25]. One of the ideas is screening fluorogenic ester resistant to endogeous esterases but hydrolysed by genetically controlled exogenous esterase [25].

Brightness   In practice, in order to visualize responsive cells in the tissue, one needs a fluorescent probe that is sufficiently bright, which is related to the fluorescent quantum yield [8] of the indicator. The canonic fluorescent proteins GFP and its derivatives [9] normally have high quantum yield ~ 0.7, so those GECIs/GEVIs based on these flu-

---

[7]Despite quite a few successes [20–22], more empirical data suggest that many cell types or tissues do not take these dyes well, regarding penetration into the tissue as well as permeability across the cell membrane (even with the membrane permeable version).

[8]The definition of quantum yield is $\Phi = \frac{\#\ \text{photons emitted}}{\#\ \text{photons absorbed}}$. The actual brightness is determined by extinction coefficient $\times$ quantum yield.

[9]GFP derivatives are engineered GFP mutants that have different excitation/emission spectrums, such as the yellow fluorescent protein (YFP) and cyan fluorescent protein (CFP) that are often employed for FRET-based GECI and GEVI. Red fluorescent proteins (RFP) like mCherry, is based on DsRed, a fruit fluorescent protein belonging to a different family to GFP. However, RFPs are erroneously referred to as GFP derivatives due to nomenclature convenience.

orescent proteins normally appear bright in the image. However, a recently developed GEVI, Arch [26], that is based on a microbial rhodopsin, has extremely low the fluorescence quantum yield ($\sim 10^{-3}$), therefore it is very challenging to detect its fluorescence signal.

Sensitivity   In an imaging experiment, the neuronal activity is quantified as $\Delta F/F_0$, where $\Delta F = F_{obs} - F_0$. F_{obs} is the probe fluorescence at a given time (normally peak value during activation), and F_0 is fluorescence at baseline. The signal-to-noise ratio (SNR) is defined as the ratio of the fluorescence signal change [10]ΔF to the shot noise on the baseline fluorescence, $F_0 N^{-1/2}$, where N is the number of photons detected [16]. Among the currently available indicators, calcium-dependent indicators generally have higher SNR than voltage-dependent indicators. Because of this, they are more commonly used in a variety of studies, especially in *in vivo* imaging in which animal movements introduce additional noises thereby decreasing the SNR.

Among GECIs, GCaMPs generally produce a larger fluorescence change than FRET-based indicators do, therefore they have higher SNR. GCaMP2 was developed in 2001, already able to robustly report spike trains. GCaMP3, developed in 2009, enhanced the fluorescence increase 4-6 fold [27], thereby further increased the SNR and the dynamic range. However, for a long time, GCaMPs could not beat the superior SNR of the chemical-based calcium indicators, such as OGB-1 AM, but that situation has been changed by the most recent GCaMP6. Nowadays, the fast version of GCaMP6 has been

---

[10]An equivalent calculation for FRET sensors takes the difference in donor-acceptor ratio divided by the combined shot noise on the baseline fluorescence of both FPs.

used in *in vivo* recording to detect single action potentials in the neuronal somata, as well as synaptic calcium-transient in individual dendritic spines [28].

Photostability Continuously monitoring the activity requires an indicator that remains stable during repeated excitation. However, most indicators suffer from low photostability. Chemical-based voltage indicators are normally photobleached within seconds, while the recently developed GEVIs, including ArcLight [29, 30] and Arch [26], have improved lifetime. Compared to voltage indicators, calcium indicators generally exhibit much better photostability. Both the chemical version and GCaMPs (GCaMP2 and the higher versions) can be repeatedly imaged for hours without dramatic photobleaching [11]. Yet, GCaMPs are "chronically" expressed in the cells, which provides long-time window for imaging. One can repeatedly record the same cells over days and weeks to study the dynamic circuit during development or the process of learning.

Potential perturbation Both chemical- and protein-based indicators could potentially add calcium buffering or perturb the membrane electrical property, thereby affecting the functional integrity of the neurons [18, 31] and even the behavioral phenotypes [27]. At low probe concentration, it is difficult to visualize positive cells because of dim fluorescence; in contrast, highly-concentrated probes give increased baseline brightness and SNR, but can alter calcium homeostasis and compromise the signal. Thus, in both chemical loading and genetic expression, the abundance of the indicator needs to be controlled. Empirical evidence showed that genetically expressed indicator did

---

[11]It also depends on the imaging technique, for example confocal microscopy causes more serious photobleaching compared to two-photon or light sheet microscopy. See details in the next section.

not cause detectable abnormality [27,32], which is probably because, in most cases, the genetically-expressed indicators present in cells with a relatively low concentration [33].

Voltage-sensitive dye is able to detect synaptic input and subthreshold activity, but its low signal-to-noise ratio and vulnerability to photobleaching make it less practical for repeated cellular recording. Most of the fluorescent protein-based voltage probes have been limited by small response magnitudes and slow kinetics. The rhodopsin-based new GEVI, Arch [26], is potentially attractive if its brightness can be increased. Currently, the start-of-the-art calcium indicators, specifically GCaMPs, are the preferred choices for large-scale cellular recording in the study of neural activity.

1.2.2 Fluorescence microscopy techniques for neural activity recording

To monitor the activity of a large population of neurons, the first two requirements on the optical instrument are: 1) large field of view to cover many neurons in the tissue, 2) high speed to follow fast biological processes such as Ca^{2+} or voltage dynamics. A wide-field fluorescence microscope may immediately comes to mind that directly takes full advantage of the advanced camera [12] with a large sensor and high speed. However, it only works well for imaging the surface of a tissue. When it focuses down to the interior, the signal normally deteriorates rapidly, mostly due to the emission light from out-of-focus region of the tissue. Therefore, the first key for volumetric imaging is to remove the out-of-focus light, and two general approaches have been used to do that. One

---

[12]It mainly includes two categories of cameras: charge-coupled device (CCD) and complementary metal-oxide semi- conductor (CMOS) cameras.

is computationally subtracting the extraneous signals, and the other is instrumentally avoiding out-of-focus light by restricting the illumination, the so-called optical sectioning.

The *computational approach*, known as deconvolution, is based on information about the process of image formation and recording to remove the out-of-focus light from each spot on the raw image. A different approach to drop the out-of-focus signal by computational procedure is structured illumination microscopy (SIM) [34, 35]. One of the properties of the out-of-focus signals is that they are insensitive to certain changes of illumination, for example, the three phase-shifted sinusoidal pattern [34]. After pairwise subtraction of raw images obtained at different phases, common signals, mostly out-of-focus light, will be to some extent canceled out, but in-focus information that is modulated by the sinusoidal illumination pattern remains. This method achieves "optical sectioning" by taking multiple images with a conventional wide-field microscope, and has been successfully applied in three dimensions [35]. Alternatively, out-of-focus light can be assigned back to "non-focus" voxels in the three-dimensional space according to the angular information collected by additional microlenses [36]. Although these approaches can help remove/correct out-of-focus light computationally, they still leave behind the associated shot noise with wide-field illumination, as well as limited depth of penetration. For very thick samples with a large amount of out-of-focus light, they cannot produce images with sufficient contrast.

Classic *optical sectioning* aims to deliver excitation light only to the focusing regions, that, in theory, can be a point, a line, a plane, or even an irregular pattern. Accordingly, a volumetric image in the three-dimensional space will be acquired one voxel, one line or one plane, at a time. In practice, the most popular optical sectioning technique

over past decades is point scanning microscopy, including confocal and two-photon microscopy. However, the series point scanning is time-consuming, and many efforts have been made to improve their imaging speed. To date, for fast large-scale imaging, one may consider spinning-disk confocal microscopy and planar illumination-based so-called light sheet microscopy. Additionally, two-photon microscopy, as the most commonly used optical approach for recording neuronal activity, with exceptional advantage of beating scattering [13], and therefore is capable of penetrating deep into the brain, will also be introduced in this section.

Two-photon microscopy

Before explaining the imaging technique, I would first introduce the two-photon effect. When using the standard green fluorescent fluorophore GFP for example, while one-photon effect describes the fluorophore molecule absorbing a single photon with wavelength of $\sim 488\,\text{nm}$ and emit a photon of $515\,\text{nm}$, "two-photon excitation" is the quasi-simultaneous absorption of two near-infrared photons [14] and gives out a $515\,\text{nm}$ photon. The probability for such a two-photon absorption event is low, and therefore requires high photon density, which is usually achieved using a high-energy pulsed laser and spatially focusing the laser beam through a high-numerical aperture (NA) microscope objective. Because that probability is in a quadratic relationship to the excitation

_____

[13]*Scattering*, is an essential optical property of most biological tissues, especially brain tissues [37]. Due to the heterogeneity of refractive index of substances inside the tissue, light will not simply take the direct path but be diffracted, reflected and refracted by the tissue. This applies to both excitation and emission light in fluorescence imaging. Scattering causes the light redistribution to undesired regions, thereby resulting in out-of-focus illumination as well as lost of in-focus emission light (emission light from the in-focus regions appears to have been emitted from the last point of scattering but not from the actual location). This phenomenon gets worse as one images deeper into the tissue, substantially challenges the imaging technique.

[14]The common two-photon light sources are Ti:sapphire lasers with 720-1050 nm tunable output.

intensity, successful excitation only takes place locally at the focal point, but not any non-focal regions. This is called "intrinsic optical sectioning". Despite the light that is scattered inside the tissue, since all the emitted light is coming from the exact focus locus, one can collect as much as possible that is coming out of the tissue and assign all of them to the respective scanning point (origin). It doesn't require a pinhole to eliminate the scattered light, and therefore has much higher photon budget compared with confocal microscopy. Along with the insusceptibility to scattering, longer excitation wavelength also allows better depth penetration. The attainable *in vivo* imaging depth has been reached to $\sim 800 - 1000\,\mu$m below mouse pia, the typical layer 5 neocortex [10, 38]. The insusceptibility to scattering also enhances the spatial resolution and signal contrast of the image. In addition, "intrinsic optical sectioning" confines effective illumination only to the vicinity of the focal plane, thereby largely reducing photobleaching/photoxicity of out-of-focus regions of the sample.

Due to the point laser-scanning nature of two-photon microscopy, collecting a volumetric image requires serially scanning the excitation point in the three-dimensional space, which is typically achieved by a pair of galvanometric mirrors for lateral scanning and a piezoelectric actuator for continuous axial movement [15] [40, 41]. While the speed of the scanning is somewhat limited by the attainable oscillation frequency of mechanics, the bottleneck of the imaging speed is the minimal dwell time required for each pixel. During the scanning, the laser has to dwell on each voxel for a period of at least 10^{-6} s [16] to collect sufficient photons thereby achieving reasonable signal-to-noise ratio

---

[15] Novel approaches for fast z-scanning include remote mechanical z-scanning, temporal focusing, and variable focus lenses, as reviewed by Lutcke et al. (2011) in "Two-photon imaging and analysis of neural network dynamics" [39].

[16] For detail mathematical reasoning, please refer to the supplementary information "Fundamental speed limits of optical microscopy" in "Fast three-Dimensional fluorescence imaging of activity in neural

[17]. According to this minimal dwell time per pixel, and within a maximum of 2-3 s time window in calcium imaging, the conventional point scanning two-photon microscopy can scan $2 - 3 \times 10^6$ pixels. In a typical experiment, these pixels constitute a volume of $256 \, \text{pixels} \times 256 \, \text{pixels} \times 40 \, \text{frames}$, containing several hundred cells.

One way to overcome that speed/spatial limit is parallel illumination, where instead of focusing the laser into a single voxel, it splits the light into multiple "beamlets" (an array of beams) to illuminate multiple spots and image them with a camera at one time [44]. With a similar multi-focal strategy, combined with targeted path [18] approaches, several advanced two-photon microscopy techniques have been invented to increase imaging speed, in which a diffractive spatial light modulator (SLM) [45] or nonmechanical acousto-optic deflectors (AODs) [46] is used.

The multi-focal imaging strategy is to some extent going back to the "wide-field" fashion. The inevitable emission cross talk among multiple focal points would compromise the merit for overcoming scattering - the initial attraction of two-photon microscopy for deep brain imaging. However, it is always a balance among the three key criteria mentioned at the beginning of this section — imaging volume, speed and scattering. Different from two-photon microscopy, spinning-disk confocal microscopy and the recently emerging light sheet technique balance the three criteria yet lean towards higher speed and larger volume.

populations by objective-coupled planar illumination microscopy" by Holekamp et al. (2008) [42]. Similar discussions can be found in chapter "Fluorophores for confocal microscopy" by Tsien et al. in "Handbook of biological confocal microscopy" by Pawley (2010) [43].

[17]See "signal-to-noise ratio" in page 12.

[18]With pre-defined lines or discrete regions of interest, one can move the the laser focus only to the selected pixels. Such targeted scanning avoids wasting time on background regions and maximizes signal integration time on the selected pixels (useful structures in images). With an acousto-optic deflector (AOD), the laser focus can be moved within microseconds between any two positions in a field of view.

Spinning-disk confocal microscopy

Similar to two-photon microscopy, conventional confocal microscopy is also a technique based on point laser scanning. Except for the difference in wavelength, both deliver illumination light by the imaging objective that focuses the laser light into a point. However, without the two-photon effect, the excitation not only occurs at the desired in-focus point, but also extends to the non-focusing area that conforms to the point spread function of illumination light – a double cone excitation shape. In order to prevent out-of-focus emission light from non-focus planes, a pinhole is placed in the optically conjugated focal plane before the detector, and then the only signal collected is from the in-focus spot in each point scanning.

With the similar "multiplex" idea as mentioned for two-photon microscopy, in order to enhance scanning speed, different strategies have been used to illuminate multiple pixels simultaneously while collecting emission light from them at the same time. In practice, the most popular technique is spinning-disk confocal microscopy. It uses a disc with arrays of pinhole apertures that illuminate hundreds of spots simultaneously. During rapid rotation of the disc, the emitted fluorescence light from these spots is then focused onto either the same or different pinholes before forming images on a camera [47]. The arrangement and size of the pinholes on the disc allow scanning of the entire field of view during rotation. In addition, the same spots can even be illuminated several times within a frame time, thereby accumulating dwell time with reduced excitation energy. In fact, spinning-disk confocal normally uses an arc-discharge lamp for wide-field illumination, and the low excitation energy reduces photo-toxicity and photo-bleaching compared to the conventional confocal, making it the preferred system for live imaging.

However, the lower power illumination per pixel mentioned above on the other hand restricts the penetration depth. In addition, one major disadvantage of the spinning-disk confocal is its inefficient use of light. If pinholes occupy 1% of the disk area, 99% of the light is wasted. In order to increase the amount of light into each pinhole, a second disk containing an array of microlenses can be placed on top of the pinholes [48]. In such a design, a collimated laser beam is focused by those microlenses into the corresponding pinholes, which greatly increases the illumination efficiency.

In spinning-disk confocal, the pinhole aperture size, type and spacing affect the imaging speed; these parameters also determine the brightness of the out-of-focus excitation, thereby influencing the image quality. One would carefully choose these parameters to balance the image speed and quality according to specific needs. However, the configuration is normally fixed during manufacturing and cannot be adjusted by users.

Light sheet microscopy

In light sheet microscopy, all the pixels on the focal plane of the objective are illuminated and imaged at one time, so this technique possesses high speed and a large field of view, equivalent to that of wide-field microscopy. However, it limits the sheet illumination to the vicinity of the focal plane, thereby minimizing out-of-focus light. The idea of planar illumination was first described by Siedentopf and Zsigmondy in 1903 [49], but it had not been used to image the interior of a biological tissue until ninety years later when it was implemented as a fluorescence light sheet microscopy [50].

How to create planar illumination? Planar illumination is not as widely understood as the single point illumination, which is normally produced by a regular objective lens in confocal or two-photon microscopy. In fact, in the latter techniques, it is the same objective lens that functions for both delivering point illumination as well as collecting emission light for imaging. In light sheet microscopy, a light sheet needs to be introduced from the side of the tissue to the focal plane of the imaging objective lens, so it requires a separate lens [19]. A light sheet can be generated by focusing the expanded laser beam in only one direction by a convex cylindrical lens or a uniaxial gradient-index lens [54, 55]. Alternatively, it can also be formed by a combination of a spherical lens and a concave cylindrical lens that spreads the light only in one direction. The latter combination design allows the use of a conventional microscope objective lens as the spherical lens, therefore provides the flexibility to choose between different commercially available objective lenses, and the convenience to change lenses through standard adapters. However, the low cost cylindrical/spherical lenses can be used to make miniaturized illumination assembly, the advantage of which will be discussed later.

Light sheet thickness Most light sheets are generated from Gaussian beams, the typical laser output. Because Gaussian beams undergo widening at increasing distances from the beam waist, the thickness of the sheet along the light propagation axis is uneven. The thinnest beam waist with thickness w_0 is positioned at the center of the field of view. The regions extended to the two sides of the beam waist where thickness

---

[19]Unconventional objectives incorporate the two parts in a single lens has been developed [51, 52]. The designs make the illumination and even the detection on an oblique plane with a shallow angle to the focal plane of the objective lens, and therefore provide a very limited filed of view at the intersection of the two planes. Wolleschensky (2008) proposed a novel lens with an add-on cap to the existing microscope lens to achieve planar illumination [53], which has not been realized yet.

goes up to $\sqrt{2} \times w_0$ are defined as Rayleigh range, which is normally used as a reference

to determine the size of an acceptable field of view. The thickness of the sheet defines

the axial resolution of a microscope, and the Rayleigh range affects the size of the field

of view. Both the thickness w_0 and the Rayleigh range are determined by the objective

numerical aperture (NA), and they counteract each other [20] Therefore, the larger the

field of view, the worse (thicker) the axial resolution (light sheet thickness). In order to

obtain a Rayleigh range of $100 - 500 \mu$m, a low NA ~ 0.1 lens is required, and the light

sheet thickness will be approximately $4 - 10 \mu$m [42].

One way to generate light sheet with relatively even thickness is using a Bessel beam

[56] instead of a Gaussian beam for illumination. This has been successfully implemented

with a high NA lens to obtain a small-area ultra-thin sheet with 3D isotropic resolution

down to $\sim 0.3 \mu$m [57]. However, such a resolution improvement comes at a cost because

the Bessel beams introduce "side lobes" of extraneous illumination outside the focal

plane, thereby compromising the image quality and subjecting the sample to much more

photobleaching and photodamage. Two practical approaches to relieve the consequences

of the side lobes are structured illumination and two-photon excitation [57].

Microscope design and sample preparation   As mentioned above, light sheet mi-

croscopy uses two separate lenses, one for delivering excitation light sheet, and the other

for collecting emission light. These two are orthogonally arranged in space. At the

cross of the illumination and detection lens is the specimen. Sticking to this geometry

---

[20]For the planar gaussian beam, under the condition with an optimal NA for minimizing light sheet thickness throughout the filed of view, there will be $w\{\ell\} = \frac{2\lambda\ell}{\pi n}$, where λ is the light excitation wavelength, n is the refractive index of the immersion medium. For details, please refer to the supplementary information "Upper limits on thickness of planar illumination" in "Fast Three-Dimensional Fluorescence Imaging of Activity in Neural Populations by Objective-Coupled Planar Illumination Microscopy" by Holekamp et al. (2007) [42].

arrangement, one can flexibly design a microscope with a preferred way to mount particular samples. For example, light sheet can be delivered horizontally from the side of the sample, and the imaging objective is vertically mounted above the specimen. This example is a typical upright microscope, and many groups adopt it because of the convenience to build it in the context of a traditional wide-field epifluorescence microscope by adding extra components for light sheet illumination. There is another similar design, normally seen in a completely homemade version. In that design, the whole upright microscopy is laid down horizontally, and therefore everything can be mounted on the surface of an optical table. In both designs, a small specimen is normally placed in an imaging chamber with side "windows" allowing access of illumination/imaging lenses. However, for large samples like a head-fixed mouse with a cranial window on the top, neither design previously mentioned will work. In order to handle this most typical sample preparation in the research of mammalian brains, Holy group invented a 45-degree vertically tilt design that allows both illumination and imaging from above [42]. The large tilt angle of light at the fluid/tissue interface normally introduces aberration [21] that to some extent can be alleviated by tuning the angle of the light sheet [54] as well as the adaptive imaging approach [60].

Scanning modality In high-speed neural imaging, 3D scanning is normally achieved by moving the rigid optics instead of the biological sample [22]. During the scanning, the

---

[21]It happens when the reflective indices of the immersion medium and sample are not precisely matched. In a typical experiment with brain tissues, the tissue reflective index is normally $1.36 - 1.41$ [58, 59], while the medium keeping the brain alive is normally aCSF with a refractive index of 1.34 [59].

[22]For *in vivo* imaging, organism needs to be kept static to avoid undesired stimulation. Even for *ex vivo* preparation, high-frequency movement may induce tissue deformation due to inertial forth. In the study of developmental process in zebrafish or drosophila embryos, some investigators chose to move the specimen directly, probably because these specimens are not sensitive to movement.

light sheet and the imaging objective need to move in synchrony, which can be attained by synchronizing signals in the two separate actuators controlling the movement of the two parts, or physically coupling the two parts together [42] and moving them together with a single actuator. The latter design requires a special coupler to hold illumination optics together with the imaging objective, and this original invention is particularly named as objective-coupled planar illumination microscopy (OCPI).

Current constrains In light sheet microscopy, the large area parallel illumination allows one to take full advantage of the advanced high-speed megapixel camera (charge-coupled device (CCD) or complementary metal-oxide semi- conductor (CMOS) cameras) for fast volumetric imaging. Recently, the speed and image size has grown rapidly with the birth of high quantum efficiency, low-noise fast sCMOS camera. The state-of-the-art sCMOS with 2560×2160 pixels and 100Hz frame rate allows one gigapixel recording every 2 seconds, a calcium imaging time window. One recent application using such a fast camera was able to perform light sheet calcium imaging of 100,000 neurons of the entire larval zebrafish brain every 1.4 seconds [11]. With the anticipation of new generation higher speed cameras, it is crucial employ facile spatial scanning of a large area of the specimen. This is already starting to become a problem for large neural tissues like mouse brains, for which long travel of light delivery/collection optics is restricted due to the limited open space around the tissue. In addition, the travel speed and precision of the mechanics are also challenged in long-distance scanning. Recently the "scanless" electrically tunable lens has been adopted to achieve flexible volumetric imaging without moving the specimen or the objective, yet the light delivery optics still need to be moved during scanning. Another inherent limitation is the penetration depth. The two-photon

technique can improve the penetration, but the current light source cannot form a light sheet with high-density photons sufficient for two-photon excitation of the entire focal plane. While two-photon line scanning microscopy is achievable and yields images up to twice the depth of one-photon light sheet microscopy [61], it largely compromises the scanning speed. Either the microendoscopy approach that adds a microprism to relay the deep tissue imaging, or an *in vivo* tissue clearing technique that directly alleviates scattering could be the potential direction to improve the imaging penetration of light sheet microscopy.

1.2.3   Managing big data for large-scale imaging

Repetitive large-scale imaging generates large data sets. This is especially true for imaging awake behaving animals, in which wealth of stimuli can be presented to the animal while monitoring the activity of neurons in the brain. This type of experiment may last for hours, resulting in terabytes of data. Both online digital acquisition as well as offline processing and analysis of these data require considerable effort in the initial development of the platform. Without going deep into computer science and mathematic algorithms, here is a brief introduction of those basic aspects involved in practice.

Image acquisition software   During a real time recording, big data poses challenges on continuous data transfer and storage. In order to attain high temporal resolution, high-performance imaging acquisition software must coordinate all the hardware and continuously write the data to hard drives with minimal overhead time. It is easier to employ the commercialized software coming along with the camera and incorporate it

into the framework, yet when one increases the imaging speed to the highest as claimed by the manufacture, poor performance my lead to "drop frames". In this situation, customized optimization of the software pipeline may be required.

Image registration For hour-long recording, biological tissues may undergo morphological changes like shifting, warping, swelling, etc.. In *in vivo* recording, there are motions caused by respiration or movements of restrained animals. In order to track the same neurons throughout the recording, imaging registration is needed to correct those mismatches of raw images. Algorithms that allow two-dimensional or three dimensional, rigid or non-rigid corrections have been developed and utilized by different scientists. Which algorithms to choose depends on the nature of the data. Generally, a three-dimensional non-rigid correction is needed for warping tissues, such as *ex vivo* preparation immersed in the medium. When the data set is so large that a single image volume reaches reaches one gigabyte, the optimization becomes a challenge for both the efficiency of the algorithm and the performance of the computer.

Image segmentation In order to extract the information of individual cells in the imaging volume, one needs to first determine which pixels are regions of interest (ROI), such as pixels representing cell bodies or neuronal processes. While manual image segmentation is possible for small size images, large images necessitate automatic algorithms for ROI recognition. There are two basic ideas to design the algorithm. The first one is based on anatomical criteria, which relies on the contrast of ROIs to the background. However, this approach becomes less practical as the new functional indicator like GCaMPs normally doesn't provide sufficient contrast at baseline. Nowadays

the segmentation of ROI heavily relies on the functional criteria [62], as pixels that belong to the same cells change intensity together, so temporal information will provide a useful basis for imaging segmentation. Different algorithms based on this idea have been developed and are still being improved upon [63]. It is worth pointing out that a good signal-to-noise ratio of individual neurons is required for robust ROI detection, as weakly responsive cells are normally difficult to recognize by algorithms. Additionally, for a heavily labeled, dense neuronal population, adjacent neurons that largely share similar response patterns normally require extra care to differentiate, for example by adding prior knowledge about the contour of ROIs, either by algorithm or manually. The latter strategy is called semi-automatic approach, which represents the main stream of the current status of the field.

1.3 Scope of the thesis

In the previous sections, I have reviewed approaches for recording activity from large number of neurons. Particularly, Light sheet fluorescence microscopy technique, with a relatively short history in neural imaging, is raising with potent momentum for fast large-scale neuronal recording. Focusing on this technique, specifically the objective-coupled planar illumination microscopy (OCPI) that was originally invented here by Holy group, my dissertation will further elaborate two directions of study.

A major body of this dissertation is an application of this technique in the research of neural individuality. This part of study was performed in the context of mouse pheromone-sensing neurons, which consist hundreds of distinct neuronal types. In order to investigate whether individual animals possess distinctive types of pheromone-

sensing neurons, I took advantage of OCPI imaging to exhaustively record activity from mice with different sexes and experiences to study potential sexual dimorphism and experience-dependent plasticity.

The second goal of this dissertation is to develop a new variant of OCPI microscopy to extend its application into *in vivo* imaging of mouse brain activity. The new technique, through a particularly designed horizontal scanning, combined with the advanced high-speed camera, also further enhances the imaging speed and scanning volume.

1.4 An application: neural individuality

What factors make individuals unique? Variability stems in part from genes and epigenetics, and recent advances have permitted the study of such differences on a genome-wide scale [64]. However, much of what distinguishes individual persons or animals lies within the nervous system [65]. At a macroscopic level, inter-individual variability of the brain, for example in terms of cortical thickness/surface area [66] and grey/white matter structure [67], are correlated with performance in basic and higher cognitive functions [68,69]. The emerging connectome [3] as well as single neuron innervation pattern analysis [70] also suggest diverse neural wiring across individual organisms. Therefore, it is intriguing to study the individual differences in the nervous system as well as how the differences arise.

However, it is difficult to investigate individuality of neural structure and function. In a neuronal circuit, there are normally over 100,000 neurons of diverse types, intricate wirings, and synaptic/electrical connections. In order to make a comprehensive comparison between individuals, one has to sample a representative neuronal population from

each subject at the single-neuron level. As a result, there are extreme challenges on the resolution, scale as well as the efficiency of the research approaches. Large-scale cellular imaging that simultaneously records activity from a very large neuronal population provides the opportunity to tackle this task. By exhaustive calcium imaging of a whole organism [11–13] or a local circuit [71, 72], one can examine individual differences in the functions of neurons.

1.4.1 Mouse pheromone-sensing neurons

We focused on the mouse vomeronasal epithelium, a component of the olfactory system devoted to social cues, often called *pheromones*. Pheromones mediate a variety of innate social behaviors, including sexual behavior [73–82], male aggression [74–76, 83–86], interspecies defensive behaviors [87], maternal aggression [76–78, 80, 88] and lactating behavior [77]. These behaviors are specific to animals of particular sex, species, ages, experiences, etc.; it is very likely that neural circuitry for pheromone signaling contains information of animal identities. Pheromone-sensing neurons that directly detect pheromone chemicals and initiate the downstream signaling may be the fundamental source of individuality.

Mouse pheromone-sensing neurons, also called vomeronasal sensory neurons (VSNs), are packed in the vomeronasal epithelium(Fig. 1.1). Each sensory neuron sends an apical dendrite to the surface of the epithelium, where a receptor protein expressed at the dendritic tip can detect chemical cues from the nasal cavity. There are approximately 300 different vomeronsal receptor genes [91], and each sensory neuron mainly expresses a
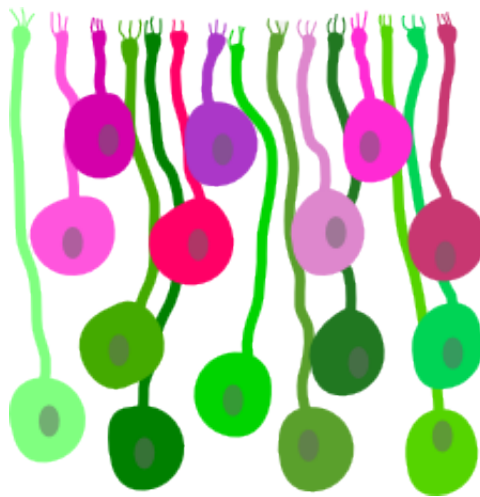
Figure 1.1. **Schematic of the structure of pheromone-sensing neurons.** This represents a coronal section of the vomeronasal neuroepithelium. Each sensory neurons sends a dendrite to the surface of the epithelium to detect chemical cues. Apical neurons colored in magenta hues express receptor genes in the V1R family, while basal neurons in green hues express receptors in the V2R family. There is a small subset of basal neurons expressing formyl peptide receptor genes [89, 90] instead of V2R receptors. Courtesy of Timothy E. Holy.

single receptor type [23]. Due to the extensive receptor-type diversity and large number of neurons (over 100,000) in the vomeronasal epithelium, it is not trivial to compare these neurons between animals. Since the cloning of VSN receptors [89, 90, 93–96], molecular approaches including *in situ* hybridization and microarray, as well as physiological recording with electrodes [97], have been used to study different types of VSNs. However, these studies have been inconclusive [98], perhaps because the rarity of expression of each receptor gene ($\sim$300 genes, each expressed by just 0.1–1% of the $\sim$100,000 VSNs in each epithelium) [91] requires exhaustive sampling by methods sensitive to individual neurons. In this dissertation, I took advantage of the large-scale functional imaging approach to examine whether these VSN types vary by individual, by sex, and by experience.

1.4.2 Sexual dimorphism

Neuronal individuality is generated by stochastic gene expression, biological factors ("nature"), and experience ("nurture") [99, 100]. In wild-type mice, one prominent example of "nature"-induced individual variability is sexual dimorphism. Previous work has identified both sexually-dimorphic behaviors [92] and a small number of dimorphic nuclei or neuronal populations [101–109]. However, at present little is known about the physiological properties and circuit function of these neurons.

It is worth noting that in the mouse most dimorphic nuclei are downstream of mouse pheromone sensory neurons(Fig. 1.2) [92, 110, 111]. While the dimorphisms are well-established in "central" nuclei, it is unclear whether the dimorphism arises from the

---

[23]Exceptions exist in basal layer neurons expressing V2R receptor genes. These neurons express two V2Rs, with a V2R2 subfamily gene as the most common co-receptor [92].
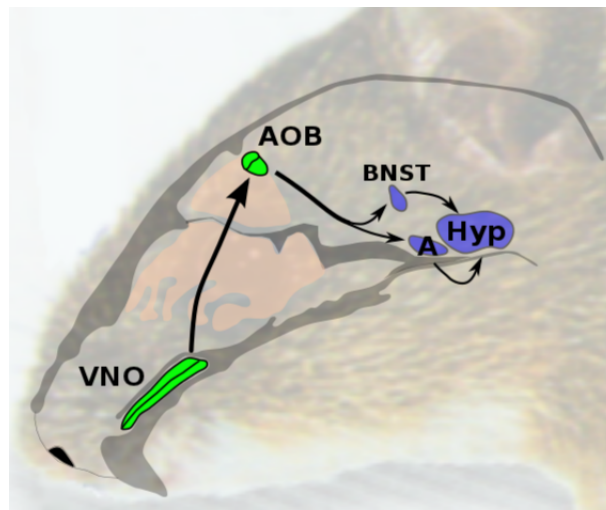
Figure 1.2. **Schematic of the accessory olfactory system.** Pheromone-sensing neurons situating in the vomeronasal organ (VNO) project to the accessory olfactory bulb (AOB), where the mitral cells send information to the deep brain nuclei (in purple), that are the previously identified sexually dimorphic brain regions: medial amygdala (A), ventromedial hypothalamus (Hyp), and bed nucleus stria terminalis (BNST). Redrawn and modified based on courtesy of Timothy E. Holy.

upstream sensory neurons. In several species, the male and female vomeronasal organs (VNOs), which house the pheromone-sensing neurons, are of different sizes [110,112,113]. However, none of the vomeronasal receptor genes have yet been found to be expressed differentially in male and female animals [94, 95, 114]. The closest known example is a difference, for cells expressing a particular V2R gene, of the mean soma depth within the VNO epithelium between the sexes [95]. However, because all VSNs receive sensory exposure through their dendritic knobs at the surface of the VNO, there is no known functional consequence of a shift in the location of the soma; moreover, this receptor gene is thought to be a pseudogene [98]. In addition, natural investigation of scents produces different amounts of *c-fos* activation in VSNs of males and females [81,115,116]; however, because the amount of voluntary investigation time also differs by sex [117], it is unclear whether differences in *c-fos* activation reflect an underlying sex difference at the level of sensory neuron types and function.

1.4.3 Experience-dependent plasticity

Individual differences may result from differential experiences. It's difficult to study the the contribution of experience in determining individual neural differences in humans due to the limited experimental approaches. Mice, which also display numerous plasticity in behaviors, offer the opportunity to pursue such questions at the level of neuronal circuitry. An extensive literature on cellular plasticity [118–123] provides a backdrop for individuality based on "nurture," but how plasticity is organized on the scale of cell types, circuits, and systems remains largely mysterious.

In the case of mouse pheromone-sensing neurons, it has been shown that experience can change the VSN gene expression [114, 124]. These studies used pooled VSNs in the epithelium, therefore it is unclear that whether the reported changes corresponded to different numbers of cells or changes of expression level within cells. In addition, Hagendorf et al. discovered an activity-dependent expression of an ether-á-go-go-related gene (ERG)—a potassium channel—in the basal layer VNO [125]. They showed that mice with reduced sensory exposure had reduced ERG expression, while mice exposed to an odor-rich environment expressed higher levels of ERG. To what extent the plasticity would lead to the changes in individual VSN functions and even the overall VSN type compositions remains an open question. Therefore, it would be interesting to compare cell types from animals with different olfactory experiences.

1.5 Methodological exploration: light sheet microscopy for *in vivo* imaging of mouse brain

Light sheet fluorescence microscopy has emerged as a powerful tool for fast volumetric imaging in biological sciences. Through focusing a thin light sheet to the objective focal plane, light sheet microscopy acquires a whole frame image at one time, thereby achieving efficient frame-based optical sectioning. With the merit of high speed, large field of view, high signal-to-noise ratio, and low photobleaching and phototoxicity, light sheet microscopy is an ideal tool for live imaging over a long time [126]. In recent years, the light sheet technique has been successfully applied to image small size organisms, such as the zebrafish [11,127], fruit fly [61], C. elegans [128], as well as *ex vivo* preparation of mouse tissue [42, 71, 72]. Most of these applications aimed for imaging developmental

processes rather than neurophysiology. As for larger preparations, especially the head-fixed awake behaving mouse, the appropriate configuration is still lacking.

1.5.1 Challenges of using light sheet microscopy in mouse imaging

Applying light sheet technique to *in vivo* mouse imaging presents several challenges. In light sheet microscopy, illumination and detection are attained through two separate lenses arranged orthogonally in space, and the specimen is positioned at the intersection of the two lenses. Typical custom [61,127,129,130] and the commercially available light sheet microscopes are all designed in a way that both illumination and detection lenses are mounted horizontally. Accordingly, a small specimen is placed in a liquid medium-filled imaging chamber with side "windows" for accessing the two lenses. However, this design cannot work for imaging an awake mouse. First, it is impossible to immerse an awake mouse in a small liquid-filled chamber. In addition, in an *in vivo* mouse experiment, brain imaging is normally conducted through a cranial window on the top of the mouse head, therefore necessitating an upright instead of a horizontal setup. Even with a classical upright imaging system, it is difficult to deliver the light sheet into a mouse brain. There was an effort to introduce the light sheet into the live mouse brain by implanting a miniature microprism to attain side illumination of target brain regions [55]. However, that invasive approach with surgical excision of nearby brain tissues has not managed to record neural activity from live animals yet. Therefore, a non-invasive upright light sheet microscope will be more suitable for imaging mouse brain activity *in vivo*.

1.5.2 OCPI microscopy

With the aim to custom build a non-invasive light sheet microscope suitable for *in vivo* imaging of the mouse brain, we previously developed objective-coupled planar illumination (OCPI) microscopy [42]. In OCPI, a light sheet is generated by a cylindrical lens placed in a custom-machined optics tube. This tube is orthogonally arranged to an objective lens, and the two parts are held together by an illuminator/objective coupler. The entire coupler is placed above the specimen with a tilt angle so that both the illumination arm and imaging arm are 45 degrees to the specimen surface. In this way, we only need a window on the top of the specimen to attain both light sheet illumination as well as imaging. By moving up and down the entire illuminator/objective coupler along the axis of the objective lens (45 degrees vertically tilted), OCPI can achieve volumetric scanning of the specimen. OCPI images up to $\sim 10,000$ neurons in a volume of $710\,\mu\mathrm{m} \times 125\,\mu\mathrm{m} \times 282\,\mu\mathrm{m}$ tissue by scanning a distance of $200\,\mu\mathrm{m}$.

1.5.3 OCPI microscopy and mouse brain imaging

This first generation of OCPI microscopy used the high performance EMCCD camera at the time when it was built, and attained calcium imaging of $\sim 10,000$ neurons every 2 seconds. It has been successfully applied to *ex vivo* imaging of the mouse vomeronasal organ [42,71,131] and accessory olfactory bulb [72,132], as well as the brains of drosophila and laval zebrafish (unpublished data). All of these applications and an initial attempt to apply OCPI microscopy to imaging the mouse cortex *in vivo* (unpublished data, collaboration with Burkhalter Lab) also motivated the development of a second generation of OCPI microscopy with following improvements and new features:

Eliminate restrictions on scanning distance In OCPI microscopy, the size of the imaging volume is restricted by the scanning modality. Similar to most of the axial scanning, the maximum scanning distance is limited to the working distance of the objective lens. Because large biological samples, such as the mouse cortex, have extensive surface areas, if OCPI microscopy can scan them horizontally (Fig. 1.3), then the imaging volume will be greatly increased. With this consideration, a second generation of OCPI named horizontal-scanning OCPI (hsOCPI) microscopy was conceived.

Miniaturize illumination optics With the aim to perform *in vivo* imaging through the cranial window of a mouse, especially to scan horizontally along the opening, a compact optical assembly is required. Because the standard imaging objective lens is normally bulky, it is desirable to minimize the size of the illumination arm on the coupler as much as possible.

Another benefit of using more miniaturized illumination optics is that one can further rotate the entire coupler to decrease the tilt angle of the objective lens in order to make it closer to the vertical line. A smaller tilt angle will alleviate the aberration resulting from light refraction at the medium and tissue interface.

One challenge for custom illumination optics is dealing with multi-color imaging. As more fluorescent probes become available, it is beneficial to implement multiple laser lines into the system. Accordingly, chromatic lenses will be chosen to build the system.
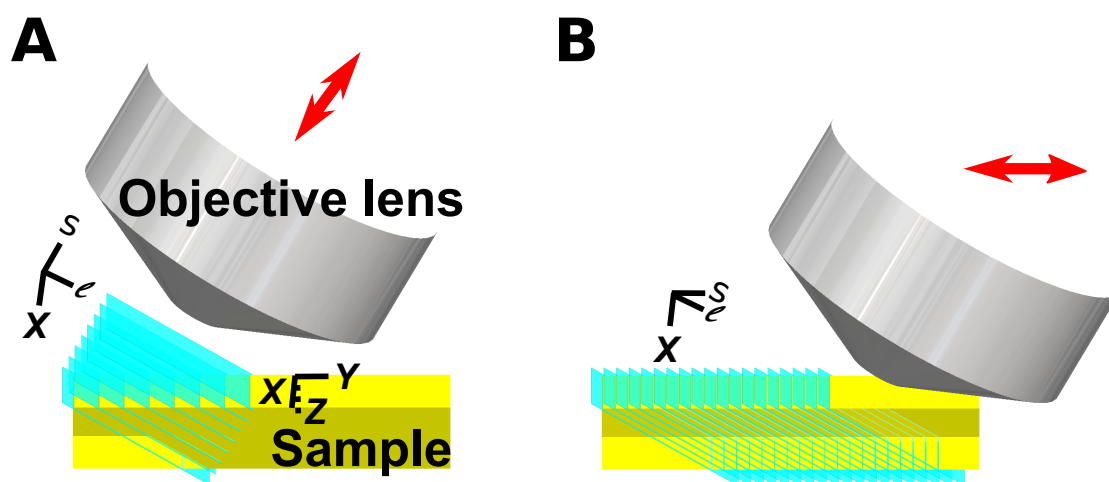
Figure 1.3. **A**, axial scanning in OCPI with limited traveling range. **B**, horizontal scanning in hsOCPI without restriction on scanning distance. s: scanning axis, ℓ: light sheet propagation direction, $X - Y - Z$: coordinates of the sample.

1.6 Summary

The scale and complexity of neural circuits drives neuroscientists to look for techniques for recording a large numbers of neurons with cellular and even subcelluar resolution. Volumetric imaging that harnesses fluorescence functional indicators and fast optical microscopy emerges as effective approach for that purpose. Among the existing optical techniques, light sheet-based OCPI microscopy exhibits potentials for further increasing the scanning volume while imaging at high speed. In the next chapters, I will first demonstrate an application of OCPI microscopy in large-scale neural recording, with the aim to unravel individual differences by exhaustively sampling pheromone-sensing neurons from individual mice. After that, I will describe a methodological study to improve the current OCPI microscopy in several aspects in order to use it in live imaging of mouse brain.

Chapter 2

Methods

2.1 Animals

GCaMP2-expressing vomeronasal organs (VNOs) were obtained from the F1 generation of tetO-GCaMP2 and OMP-IRES-tTA cross (on a C57BL/6 background) [133]. GCaMP3 VNOs were obtained from a cross between Ai38 [23] and OMP-Cre [134]. Male and female mice were singly housed from weaning on postnatal day 21, unless otherwise specified. At 12–16 weeks, male and female littermates were recorded on the same experimental day for strict parallel control. For male mice with unilateral naris occlusion, right external nares were sutured and irreversibly closed at the beginning of the exposure period, which ranged from postnatal week 3 to week 7. All experimental protocols were in compliance with NIH guidelines and were approved by the Washington University Animal Care and Use Committee.

2.2 Reagents and stimuli

The VNO tissue was dissected and maintained in carboxygenated Ringer's solution (115 mM NaCl, 5 mM KCl, 2 mM $CaCl_2$, 2 mM $MgCl_2$, 25 mM $NaHCO_3$, 10 mM HEPES, and 10 mM freshly added D-(+)-glucose) throughout the experiment. The Ringer's solution was carboxygenated by bubbling with 95% O_2/5% CO_2 in a 37 °C water bath for at least 30 min. VNO stimuli, the sulfated steroids (Steraloids Inc., RI, USA) were dissolved in methanol, 1 : 1 methanol / H_2O, or H_2O to 20 mM as stock concentration (kept at 4 °C), and were diluted to a final concentration 10 μM with freshly prepared carboxygenated Ringer's solution. 12 sulfated steroids were used in this study: A3500, 5β-androstan-3α-ol-11, 17-dione sulfate (ketoetiocholanolone sulfate); A6940, 4-androsten-17α-ol-3-one sulfate (epitestosterone sulfate); A7010, 4-androsten-17β-ol-3-one sulfate (testosterone sulfate); A7864, 5-androsten-3β,17β-diol disulfate; E0893, 1,3,5(10)-estratrien-3,17α-diol 3-sulfate (17α-estradiol sulfate); E1050, 1,3,5(10)-estratrien-3,17β-diol disulfate (17-estradiol disulfate); E4105, 4-estren-17β-ol-3-one sulfate (nandrolone sulfate); P3817, 5α-pregnan-3α-ol-20-one sulfate (allopregnanolone sulfate); P3865, 5α-pregnan-3β-ol-20-one sulfate (epiallopregnanolone sulfate); P8200, 5β-pregnan-3β-ol-20-one sulfate (epipregnanolone sulfate); Q1570, 4-pregnen-11β, 21-diol-3,20-dione 21-sulfate (corticosterone 21-sulfate); Q3910, 4-pregnen-11β, 17,21-triol-3,20-dione 21-sulfate (hydrocortisone 21-sulfate). The two negative control stimuli were Ringer's solution with 0.05% methanol as a vehicle control. For behavioral tests, A6940 and A7010 were further purified with silica gel thin layer chromatography (TLC) (Sigma-Aldrich Co., MO, USA), dissolved in ddH_2O to stock concentration 20 mM and kept at -80 °C before use. Urine from male and female mice (2- to 5-month-old) of C57BL/6

background were collected over periods of 2 weeks with liquid nitrogen [97] (CeeKay Supply) and pooled by sex. Solid-phase extracts were prepared with Strata-X 33u polymeric reversed phase column [97] (Phenomenex Inc., CA, USA).

2.3 Calcium imaging of whole-mount VNO by OCPI microscopy

Mice were euthanized with CO_2 and decapitated, and the VNO was quickly removed into ice-cold carboxygenated Ringer's solution. Under a stereomicroscope, the two VNO tissues were removed from the bony capsule, and each intact neuroepithelium was separated from the blood vessel [135]. The flatted VNO epithelium was then adhered to a nitrocellulose membrane (0.45μ m, Millipore Co., MA, USA), with the dendritic layer facing up. This whole-mount VNO preparation could be kept in ice-cold carboxygenated Ringer's solution for up to 3 hrs before physiological imaging as described [131].

Imaging was performed on a custom objective-coupled planar illumination (OCPI) microscope [42] with 488 nm light sheet (thickness: 5μm) illumination. To reduce phototoxicity, laser power was minimized to a level corresponding to ~10,000 photons per cell in each stack to achieve a shot noise-limited sensitivity to $\Delta F/F$ ~1%. Typically, this resulted in < 0.05 mW laser power when imaging GCaMP2 VNO tissue. The VNO preparation was placed in a custom imaging chamber with continuous superfusion of carboxygenated Ringer's solution (temperature: 35 °C; flow rate: 2.2 ml/min) alternating with stimuli. The stimuli and Ringer's flush were delivered through a 16-channel superfusion system (Automate Scientific Inc., CA, USA) pressurized with helium-balanced 40% O_2 and 3% CO_2. The superfusion system was computer controlled by custom software to synchronize with the imaging acquisition system (*Imag-*

ine, http://holylab.wustl.edu/software.htm). Before recording, the VNO was superfused with Ringer's for at least 30 min to acclimate. We found that stimuli resident in the superfusion system's PTFE/silicone tubing for several tens of minutes induced a global increase in fluorescence intensity of the VNO tissue, presumably due to loss of gases and the accompanying pH changes; to reduce this artifact, we expelled a small amount of each solution right before recording. During recording, each stimulus was applied to the tissue for 25 s, following by Ringer's flush for 50 s. The order of 12 stimuli together with 2 Ringer's controls were randomized within a cycle ("trial"). All stimuli were repeated in 4 cycles, together amounting to ~ 75 min of recording on each VNO imaging volume. The dimension of one tissue volume was $710\,\mu\mathrm{m}\times 125\,\mu\mathrm{m}\times 282\,\mu\mathrm{m}$, and OCPI scanned the volume every 2 s, with a 3 s pause to save the data.

2.4   Image registration and segmentation

VNO tissue normally exhibited small but detectable shifting and deformity (swelling, shrinking, warping, etc.) during long hours of recording. Such tissue movement was corrected by custom three-dimensional nonrigid registration software written in MATLAB, C++, and Julia [136]. Manual image segmentation was performed in a custom GUI in MATLAB to identify individual cells. Briefly, cells exhibiting induced and/or spontaneous activity were highlighted in images showing the change in fluorescence ($\Delta F/F$). Each highlighted region in the VNO cell body layer, but not the dendritic knob layer, was circled as a region of interest (ROI) representing one cell, avoiding double-counting in adjacent optical sections. Adjacent cells normally were clearly differentiated from

42

each other by their distinctive responses to different stimuli. For a typical VNO sensory neuron, the ROI size was $4\,\mu$m in diameter.

2.5 Cellular responses

Fluorescence intensity of a particular cell in a particular stack was measured as mean intensity of all pixels within its ROI. Cellular $\Delta F/F$ responses were calculated as the time-weighted fluorescence change upon stimulation [71], using the average of the 20 s pre-stimulus period as the background. The component of the response due to Ringer's artifact was subtracted on each trial by performing robust regression of all neurons' responses to the response caused by one of the two Ringer's control tubes. The second Ringer's control (shown as "Ringer's" in all figures) was treated identically to the other stimuli, and thus served as an independent negative control. To distinguish spontaneous activity, we tested reproducibility over all 4 trials by the one-tail Student's t-test against the second Ringer's control. Only cells responding to at least one stimulus with 1) p-value < 0.05, and 2) $\Delta F/F > 0.03$ were counted as responsive cells and kept for further analysis.

2.6 Clustering of physiological cell types

Physiological cell types were identified by clustering all responsive cells pooled from GCaMP2 imaging volumes collected in this study. Each cell was a data point in the 13-dimensional space with the value of responses to 12 stimuli and a Ringer's control. All the data points were clustered by a variant of the mean shift clustering algorithm [137], a method with sensitivity high enough to reliably detect clusters with size of no less than

10 data points. Statistical significance of clusters was assessed by performing clustering in 10,000 bootstrapped datasets, and mean shift peaks that fell into the same cluster with frequency $>= 0.05$ were merged. The above strategy robustly detected clusters with fine in-cluster homogeneity and clear between-cluster separation. After clustering, the pooled cells were split back into their individual imaging volumes. Clusters showed substantial consistency across datasets, with the main source of variability being the absolute intensity of responses.

Cells recorded from GCaMP3 VNOs were classified by reference to the much larger GCaMP2 dataset, assigning each to the GCaMP2 cell with the smallest Euclidean distance in the space of normalized responses. This approach was not effective for any new cell types, but it identified GCaMP3 cells belonging to the known types, like type-8 in Fig. 3.9B. GCaMP3 cells were also analyzed without prior classification (Fig. 3.9).

2.7 Variability analysis

For any particular cell type and set of experiments, the variability of each cell type was defined as

$$\text{Variability}(n) = 2\sigma(\sqrt{n}), \tag{2.1}$$

where σ is the standard deviation, and n is the observed number of cells of a particular type in a particular experiment (imaging volume); the standard deviation was calculated across experiments. This $\sqrt{n}$ scaling transformation is "variance stabilizing" for a Poisson sampling model, and for such a model Equation. 2.1 has a value very near 1 independent of the mean value of n [138]. This $\sqrt{n}$ scaling transformation was used, where appropriate, throughout our analyses of variability.

For each cell type, random sampling was simulated by Poisson process with λ as the mean observed cell count, with a number of samples matching the number of experimental points. To obtain the distribution of the variability, each simulation was repeated by 1,000 times and the 95% quantile used to estimate the uncertainty of the variability (Fig. 3.2f). The normalized variability (Fig. 3.11g) was defined as $(Var_{obs} - 1)/(Var_{ran97.5\%} - 1)$, in which Var_{obs} is the observed variability (from Equation. 2.1), and $Var_{ran97.5\%}$ is the two-tailed 95% quantile upper bound variability from Poisson random sampling. In this way, the normalized variability of any random sampling has a 97.5% chance to be at or below 1.

Inter/intra- animal differences were analyzed using non-overlapping pairs of imaging volumes from the same mice. For each animal, the pair of volumes (data sets) contained one from the anterior VNO and the other from the posterior VNO. The observed intra-animal difference was calculated by sum of absolute differences in $\sqrt{n}$ for each type across all the true pairs. In the permutation test, to obtain the distribution of inter-animal differences, VNO data sets from the pairwise data sets were shuffled. Shuffling was conducted across pairs but within anterior and posterior data sets, respectively. This controlled for hypothetical differences between anterior and posterior VNO (no obvious location-dependent differences were noted). Only permutations lacking any true pairs were accepted, resulting in 43 permutations using 5 true pairs. In Fig. 3.2i, each data point represents the sum of inter-animal pairwise differences for a particular permutation. The rank of the observed intra-animal difference in the 43 permuted values was reported as the p value.

2.8   Cell depth analysis

The VNO surface of each imaging volume was identified using an automated algorithm [71]. For each ROI, the distance of ROI centroid to the tissue surface was calculated, and further corrected for the imaging tilt ($45\,°$).

2.9   Long-term chemical exposure

Custom double-layer stacking cages, modified from conventional mouse cages (*Max 75*, dimensions: $18.4\,$cm W $\times 29.2\,$cm D$\times 12.7\,$cm H), were used to provide persistent exposure to natural chemical cues from other animals. Briefly, a conventional mouse cage with the bottom replaced by a stainless wire mesh (diameter: $1.6\,$mm; grid size: $1\,$cm$\times 1\,$cm) was stacked on another cage with the normal wire bar lid filled with feed and water gel pack. The two layers were locked together by a pair of screws on the mesh and bar lid, and were easily disassembled for refilling food/water and twice-weekly cage changes. The wire mesh and bar lid forming the inter-layer divider provided sufficient open area to allow urine, feces and other discharge from the upper cage fall into the lower cage, as verified by direct inspection. However, this inter-layer divider with small grid size and $\sim 2\,$cm spacing largely restricted physical contact between animals housed in the two layers. We housed the test animal in the lower layer with another animal of the same or opposite sex in the upper layer. The exposure started from weaning on postnatal day 21 and lasted 9–13 weeks unless otherwise specified. A few experiments in which dirty bedding from male/female mice was supplied manually were also conducted; there were no obvious differences between this procedure and housing in stacking cages. Mice from both paradigms are reported in Fig. 3.11.

46

Long-term application of female urine or sulfated steroids to mice were conducted with nestlets (standard size $2\,\mathrm{cm} \times 2\,\mathrm{cm}$, 1/3 of normal thickness). For each animal housed in the normal cage, a piece of nestlet was first soaked in $1\,\mathrm{ml}$ of raw female urine or sulfated steroid solution ($200\,\mu\mathrm{M}$ in $\mathrm{ddH_2O}$), and then placed into a 35-mm petri dish lid inside the cage. Animals normally vigorously chewed the nestlets, which delivered the chemicals into their VNOs, as verified by fluorescent dye tracing after a 2-hour presentation (data not shown). A fresh nestlet with stimulus was presented to each animal on a daily basis for 2–3 months.

2.10 Behavioral assay

Sniffing episodes were recorded as described [139, 140]. Individually housed C57BL/6 males and females (3- to 4-months old), and female-exposed males in the stacking-cages were kept on a 12h/12h light/dark cycle. Animals were acclimatized to the testing environment with a $15\,\mathrm{min/day}$ episode in the testing chamber for 3 consecutive days before the first trial. Trials were conducted after lights-out under red illumination. In order to promote initial contact to the cotton swab when mice freely explored the enclosed testing chamber, a neutral volatile cue, vanilla diluted 1:1000 in water, was freshly prepared as a vehicle solution. TLC purified A6940 and A7010 stock solutions were diluted with vehicle solution to a final concentration $100\,\mu\mathrm{M}$. A day's test consisted of $15\,\mathrm{min}$ of acclimatization followed by three 210-s trials, using a $\sim 20\,\mathrm{min}$ gap between trials. The three trials were (1) presentation of a cotton swab with a sulfated steroid ($20\,\mu\mathrm{l}$ solution), (2) a swab with vehicle solution, and (3) the other sulfated steroid. The order of the two sulfated steroids was randomized. Swabs, mounted in a custom

beam-break sensor [140], were introduced through a hole in the lid of the chamber at the beginning of the recording. An animal approaching the cotton swab broke the infrared beam and triggered a voltage drop of the TTL signal, which was captured at 1 kHz with a custom software [140]. Bouts of investigation lasting less than 10 ms—previously found to be false optical triggers, for example, by detector movement or changes in lighting [140]—were discarded in data analysis. Bouts of chewing, tugging, and climbing the detector, when present, tended to occur later in the trial and were not typical within the first 20 s after initial contact.

2.11   Statistics

Student's t-tests or multiple independent comparisons were used for specified experiments. Multiple independent comparisons were performed by individual Student's t-tests followed by multiple comparison correction to control for type I errors. A conservative method, Šidák correction was used. For n independent comparisons, the *corrected threshold* α_* for statistical significance was calculated as $\alpha_* = 1 - (1 - \alpha)^{1/n}$, where α is the naïve (isolated) threshold for significance. Here, $\alpha = 0.05$; for $n = 17$, this results in $\alpha_* = 0.003$.

Chapter 3

Individuality, dimorphism and plasticity in mouse pheromone-sensing neurons

3.1 Results and conclusions

3.1.1 Imaging 10, 000 neurons simultaneously from whole-mount VNO by OCPI

We imaged the whole-mount vomeronasal organ (VNO) at single cell resolution using a light sheet-based imaging technique, Objective-Coupled Planar Illumination (OCPI) microscopy [42]. OCPI microscopy works by illuminating the objective's focal plane with a thin sheet of light; the objective together with the light sheet moves up and down at a titled angle to repeatedly scan the tissue along the objective's z-axis (Fig. 3.1A). Using OCPI microscopy, we scanned a VNO volume $710\,\mu\text{m} \times 125\,\mu\text{m} \times 282\,\mu\text{m}$, accounting for approximately one seventh of the total volume of an intact VNO tissue (Fig. 3.1B). In the

cell body layer, the cell density of sensory neurons in a 4-month-old VNO was previously [141] measured to be $\sim 1.01 \times 10^6 \,/\text{mm}^3$ (averaged across sexes) [142]. We estimated the total number of vomeronasal sensory neurons (VSNs) contained in a single OCPI imaging volume as $1.01 \times 10^6 \,/\text{mm}^3 \times 710\,\mu\text{m} \times 125\,\mu\text{m} \times 282\,\mu\text{m} \times 0.9 = 18,200$ (a factor of 0.9 came from the exclusion of edges of imaging volumes during image registration). Because 1) there is a 43% increase in sensory cell number between 1 and 4 months of age, [142], and 2) males have a larger VNO volume and number of sensory neurons than females [112], we estimated that our single imaging volumes on average provided over $10,000$ VSNs for analysis.

3.1.2 Functional classification of cell types

We performed calcium imaging of VNOs while interrogating neuronal responses to 12 sulfated steroids (supplementary video 1, Fig. 3.2a, Fig. 3.5), spanning the androgens, estrogens, pregnanolones, and glucocorticoids, a class of social cues originally isolated from mouse urine [97]. Using OCPI microscopy [42, 71, 131], we collected image stacks (volumes) with frame size $710\,\mu\text{m} \times 710\,\mu\text{m}$, scanning $282\,\mu\text{m}$ along the s axis (Fig. 3.1). Of an approximate 10,000 neurons whose activity was monitored in each volume, we typically observed 700–1000 neurons responsive to at least one of the stimuli (Fig. 3.2b). The numbers of responsive neurons in each volume varied by stimulus and individual (Fig. 3.2c), ranging from an average minimum of 19 neurons (for the androgen ketoetiocholanolone sulfate, A3500) to a maximum of 552 neurons (for the estrogen 17β-estradiol
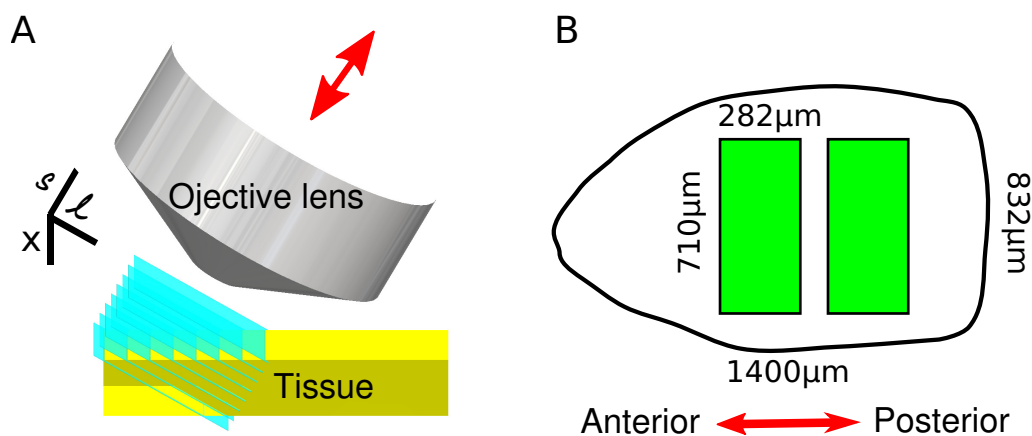
Figure 3.1. **A, schematic of OCPI volumetric scanning.** The objective's focal plane is illuminated by a thin sheet of light generated by cylindrical lens (not shown here). Illumination optics are physically coupled to the objective lens such that moving them up and down achieves three-dimensional scanning of the tissue. ℓ: lightsheet propagation direction, s: scan axis. **B, geometry of the imaging volume within the whole-mount VNO preparation.** In a subset of experiments, two OCPI imaging volumes were collected from a single VNO preparation. Those volumes cover the full tissue depth ($125\,\mu$m), and two intact regions ($710\,\mu$m$\times 282\,\mu$m rectangles in green) of the tissue when viewed from the top. In a typical intact VNO tissue of $1,400\,\mu$m long and $832\,\mu$m wide (measurement from a 3-month-old female mouse), each imaging volume covers approximately one-seventh of the whole tissue volume.

disulfate, E1050). These cell numbers correspond to ∼0.2% to 5.5% of the VSNs in the imaging volume.

Consistent with previous reports [71, 97, 132], VSNs activated by single compounds were functionally heterogeneous and could be classified into different types on the basis of stimulus responsiveness [71, 132] (Fig. 3.3). We reasoned that a much larger dataset might offer greater statistical power to detect rare types. By combining 26 VNO imaging volumes—comprising over 250,000 vomeronasal neurons—we identified 20,853 reproducibly steroid-responsive cells, nearly 10% of the total population and sufficient to expect many instances of each distinct receptor type expressed by these neurons. Based on the similarities of cell physiological responses, we clustered all steroid-responsive VSNs into 17 different types reproducible across multiple preparations (Fig. 3.2d & e, type-18 and-19 cells were detected in only a small subset of preparations). Among these 17 types, 9 types matched previously reported physiological types of VSNs studied by multi-electrode array and/or calcium imaging [71, 132], and many are also reflected in the responses of downstream neurons such as accessory olfactory bulb mitral cells [132]. Here we also discovered 8 new VSN physiological types. Most of the newly identified types were narrowly tuned to single sulfated steroids: type 3 to allopregnanolone sulfate (P3817), type 8 to epitestosterone sulfate (Fig. 3.3), type 10 to testosterone sulfate (Fig. 3.3), type 11 to ketoetiocholanolone sulfate, and type 17 to 17α-estradiol sulfate (E0893). These narrowly tuned cell types, typically with a cell count as low as 10 per imaging volume, each accounted for ∼0.1% of the neuronal population, 10-fold lower than that of the previously reported cell types. Such rare cell types could be reproducibly
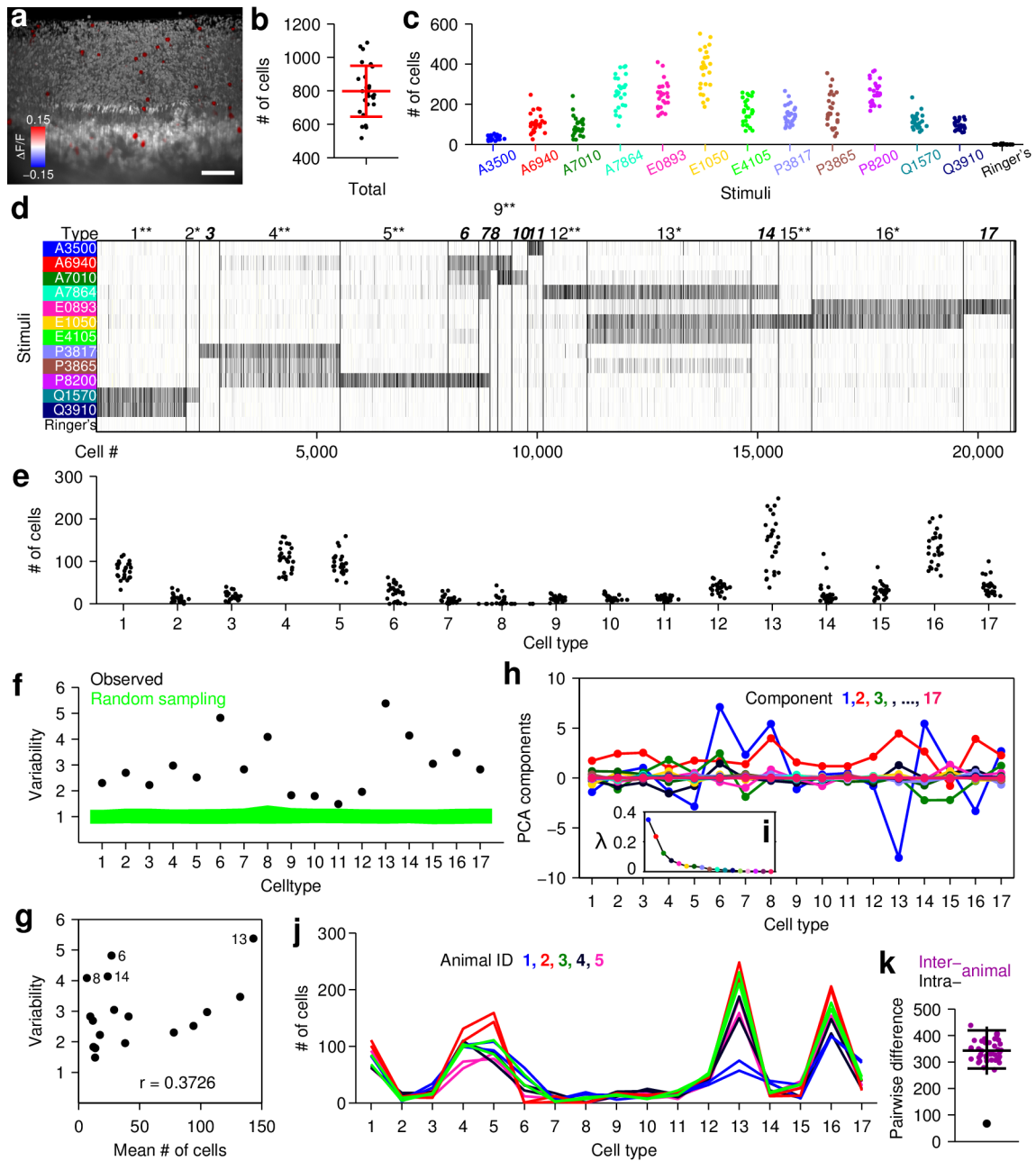
identified due to the exhaustive sampling and large numbers of neurons assembled in 26 imaging volumes.

3.1.3 Cell-type specific individual variability

We first asked whether the variability in each cell type from one imaging volume to the next was consistent with expectations from random sampling. Random sampling predicts an essentially Poisson distribution for the counts of each cell type. We compared the observed variability to that of a Poisson distribution, and found that the

---

Figure 3.2. *(preceding page)* **Large-scale recording of vomeronasal sensory responses revealed non-stochastic variability between individual mice. a**, three-dimensional rendering from an imaging volume of the whole-mount VNO. Gray scale is the raw fluorescence intensity of GCaMP2, and red/blue color scale represents the GCaMP2 fluorescence intensity change ($\Delta F/F$) caused by stimuli, here exemplified by the androgen ketoetiocholanolone sulfate (A3500). Cells responded to A3500 are visualized by the red cell bodies inside the tissue and the red dendritic knobs on the tissue surface (see comparison in Fig. 3.5). Scale bar, $50\,\mu$m. **b**&**c**, cell counts in each VNOimaging volume, in terms of total number of steroid-responsive cells (b) and number of cells responding to each stimulus (c). **d**, cluster organization of cells (from 26 imaging volumes) revealed at least 17 reproducibly-identified physiological types of VSN. Types marked by ⋆ correspond to previously-reported VSN physiological types [71,132]; ⋆⋆ represents types corresponding to observed mitral cell responses in the accessory olfactory bulb [132]; bold indicates newly-discovered types. Each column represents a single cell. For each stimulus, gray intensity represents the average induced fluorescence change $\Delta F/F$ across 4 trials. **e**, cell counts of each VSN physiological type in each imaging volume. **f**, cell count variability (see Methods) of each type in all imaging volumes. Green represents the 95% confidence interval if cell numbers are drawn from a Poisson distribution. **g**, variability was not correlated with cell abundance, r: Pearson's correlation coefficient ($p = 0.1408$). **h**&**i**, PCA analysis of cell counts in all types. Principal components are color coded, and scaled by the corresponding λ (i). **j**, Pairs of imaging volumes recorded from the same animals. Each color represents one animal, and the two lines with the same color are the two non-overlapping imaging volumes from the same animal. **k**, difference of intra-animal pairs (•) was smaller than that of any combination of inter-animal pairs (•) from shuffling across the pairs in h. Error bars represent standard deviation in b and 95% confidence interval in k.
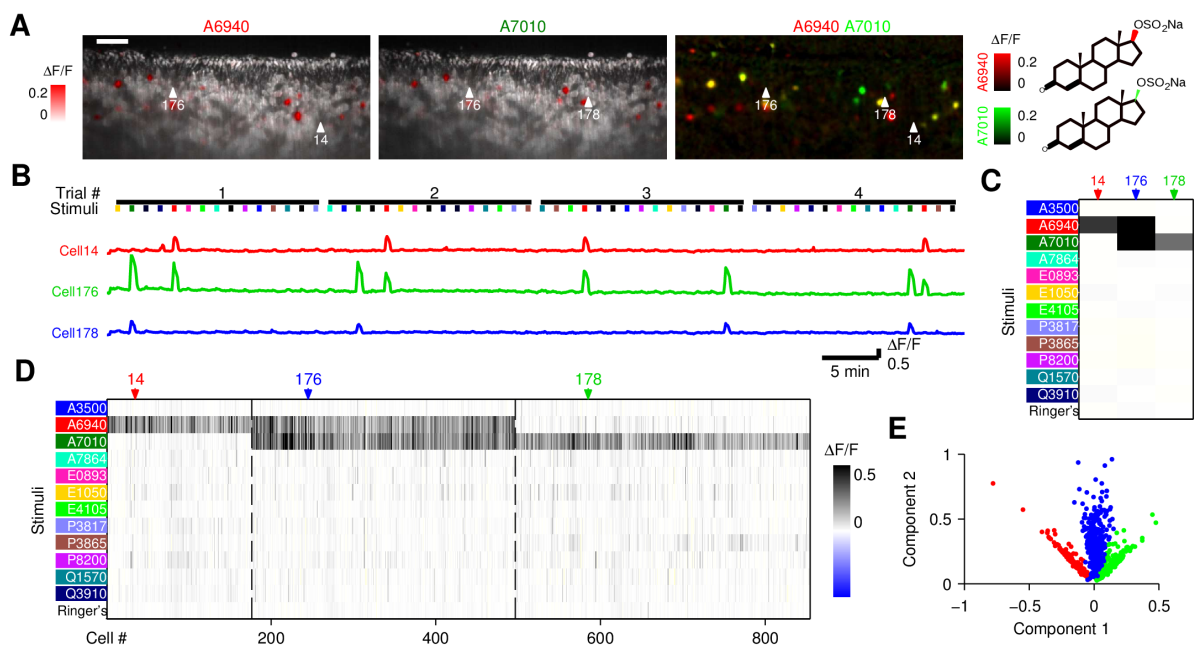
Figure 3.3. **Classifying specific VSN functional types using multiple stimulus responses: an example of two steroid enantiomers. A**, a two-dimensional slice showing responses to two stereoisomers, epitestosterone sulfate (A6940, left) and testosterone sulfate (A7010, middle). Red color scale represents the GCaMP2 fluorescence intensity increase ($\Delta F/F$). Right, merged image with responses to the two stimuli encoded in different color channels. Cell 14 responded to A6940, cell 178 responded to A7010, and cell 176 responded to both. Scale bar, $50\,\mu$m. **B**, $\Delta F/F$ as a function of time for the example cells in A. Delivery of different sulfated steroids and Ringer's control is represented by colored bars, with red for A6940 and green for A7010. These cells were specifically activated by A6940 and/or A7010 in all 4 trials. A small fluorescence increase triggered by stimulus delivery, independent of the particular contents of the stimulus, was present in essentially every cell in the recording (uncorrected trace shown; see Methods). **C**, column representation of the example cells in A and B. For each stimulus, gray intensity is the average of $\Delta F/F$ across 4 trials. **D**, the subset of all neurons showing selectivity for either (or both) of these androgens. **E**, linear discriminant analysis (LDA) for all the cells in D reveals three largely-separated groupings of cells. Each dot represents a single cell (color indicates cluster identity in D); the original 13-dimensional response vectors in D are projected to the first two LDA dimensions.

observed variability exceeded expectations by as much as 5-fold (Fig. 3.2f) with striking differences among the different types. For all 17 cell types, the excess variability was statistically significant (above the 95% confidence interval of random sampling). The degree of excess variability did not obviously correlate with factors such as abundance (Fig. 3.2g): the four most variable were types 6, 8 and 14 (among the rarest types) and 13 (the most common type). Neither did the variability obviously correlate with tuning width, as the more variable types included those sensitive to a single ligand as well as types responding to multiple ligands (Fig. 3.2d).

To determine whether variability in one type might be correlated with variability in another, we performed a Principal Component Analysis (PCA) of the scaled cell counts (see Methods). We found that 58.11% of the variance was explained by the first two components (Fig. 3.2h&i). The second-largest component was approximately flat, and therefore approximately represented the variability in the total number of responsive cells from one preparation to the next. However, The largest component showed a strong positive correlation among type 6, 8 and 14, and anticorrelation with type 13 (and more mildly with types 5 and 16). This "axis" of variation was therefore extremely selective for particular cell types.

To determine whether the observed variability reflected features specific to individual animals, in 5 preparations we imaged two non-overlapping volumes (Fig. 3.2j) and compared the intra-individual differences in cell-type counts against the inter-individual differences. We found that, on average, the intra-individual difference was dramatically lower than the inter-individual difference (Fig. 3.2k). In aggregate, no arrangement of cross-animal pairwise comparison among these 10 recordings had lower pairwise discrep-

ancy than the pairing based on individual identity ($p = 0.022$, permutation test, see Methods).

We conclude that cell-type variability is significantly greater than expected by chance, is much larger for certain cell types than others, and is a signature of the individual animal.

3.1.4 Mechanisms of individuality: sexual dimorphism

The animals used in Fig. 3.2 had identical autosomal genotypes, but included both males and females. To determine whether cell type abundance was influenced by sex, we analyzed cell counts separately for 6 male and 5 female datasets. Both males and females possessed neurons responding to each ligand (Fig. 3.4A–D). Neither the total number (Fig. 3.7a) nor number of neurons responding to each ligand (Fig. 3.4E) varied significantly between males and females, although males had a non-significant tendency towards more cells responding to epitestosterone sulfate (A6940, $p = 0.1033$), testosterone sulfate (A7010, $p = 0.2318$), and epipregnanolone sulfate (P8200, $p = 0.0197$, not significant in the test with Šidák correction for multiple independent comparisons, see Methods). This indicates that males and females can detect all of these sulfated steroids, and that even the numbers of cells responsive to each ligand do not show dramatic dimorphism. Likewise, at the level of cell types, we found that the large majority of VSN types existed in both sexes (Fig. 3.7a, Fig. 3.6): for 15 out of 17 types, we found that the cell counts were comparable between males and females, indicating that the majority of steroid-responsive VSN types were equally expressed in vomeronasal organs from mice of either sex.
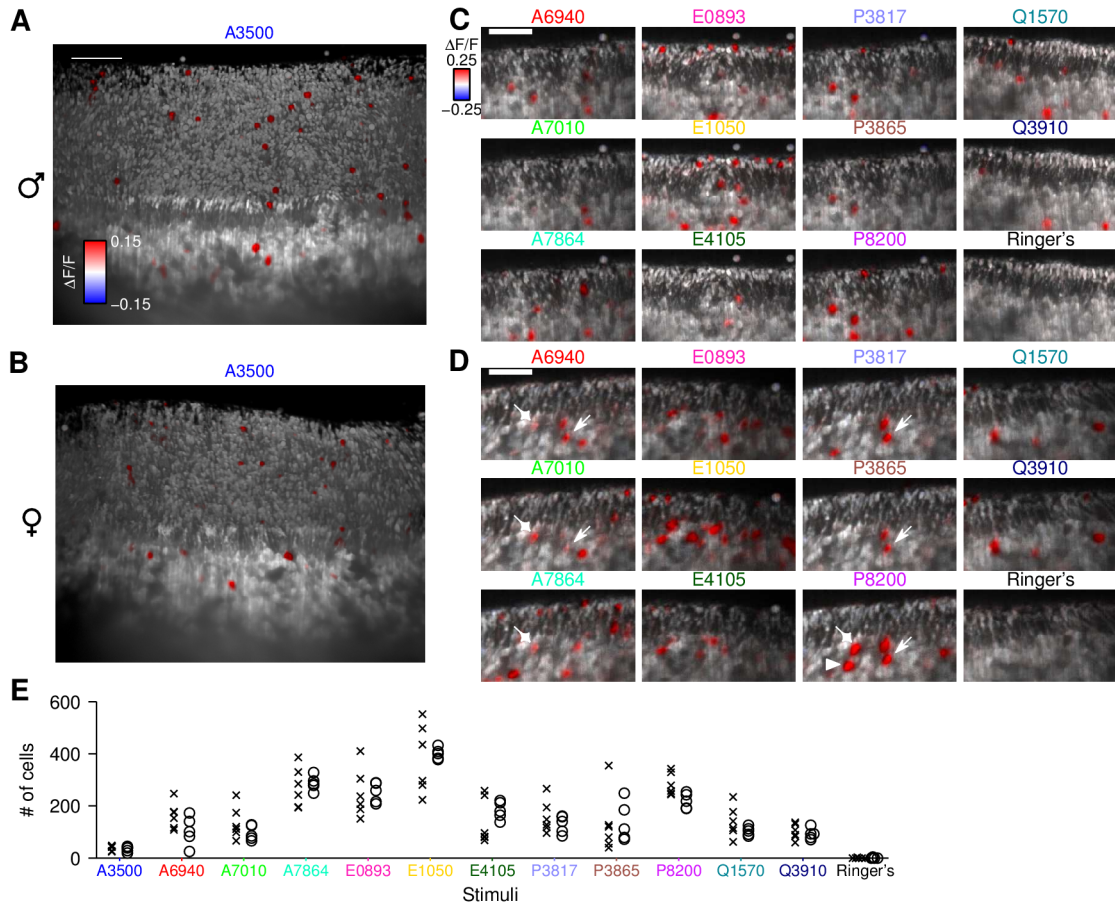
57

Figure 3.4. **Large-scale recording of sensory responses to sulfated steroids in male and female mouse vomeronasal organs.** Three-dimensional rendering of whole-mount VNOs from male (**A**) and female (**B**) mice. Gray scale is the raw fluorescence intensity of GCaMP2, and red/blue color scale represents the GCaMP2 fluorescence intensity change ($\Delta F/F$) caused by the androgen ketoetiocholanolone sulfate (A3500). Both male and female VNOs responded to A3500 as visualized by the red cell bodies inside the tissue and the red dendritic knobs on the tissue surface (see comparison in Fig. 3.5). **C** & **D**, two-dimensional slices from male (C) and female (D) VNO imaging volumes show cellular responses to the other 11 sulfated steroids. Both male and female possessed VSNs responding to the tested steroids, but not Ringer's control. VSNs responsive to single steroids (illustrated by epipregnanolone sulfate (P8200)) were heterogeneous: arrowhead indicates a cell responding exclusively to P8200; diamonds indicate a cell responding to P8200 and three androgens (A6940, A7010 and A7864); and arrows indicate a cell responding to all pregnanolones (P8200, P3865 and P3817) and two androgens. **E**, number of cells responding to each stimulus in each male ($\times$) and female ($\circ$) VNO imaging volume. Each marked point represents one entire imaging volume. There were no significant differences between male and female VNO imaging volumes (Students' t-test with Ŝidák correction for multiple comparison, familywise significance level $\alpha = 0.05$). Scale bar, 50 μm.
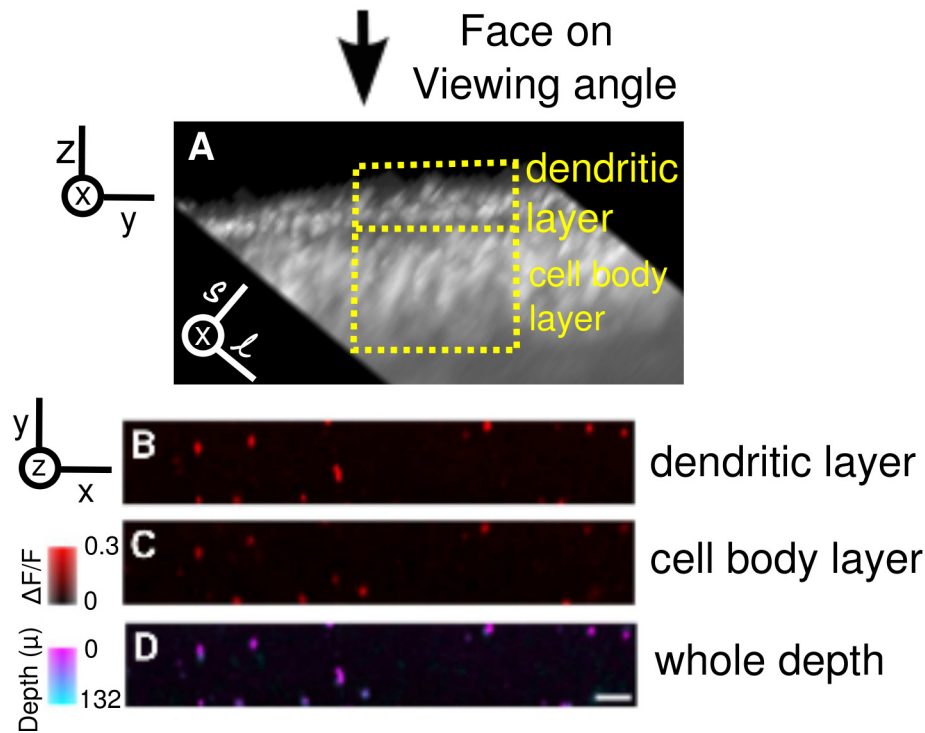
Figure 3.5. **Calcium signals at the dendritic knobs and the cell bodies were consistent when whole-mount VNO was stimulated by sulfated steroids. A**, a side view of a VNO imaging volume with surface facing up. In this view, the dendritic knob and cell body of each VSN were aligned vertically. x-ℓ-s represent the coordinate axis related to image acquisition, with ℓ representing the lightsheet propagation direction and s along the scanning axes (refer to Fig. 3.1). x-y-z are coordinate axes for tissue, in which z is along the tissue depth. Rectangles encompass the regions of dendritic layer and cell body layer analyzed in B-D. Haze below the cell body layer is a consequence of scattering. **B &C**, maximum intensity projection of cell responses to A3500 at the dendritic layer and cell body layer defined in A. Red color scale represents the GCaMP2 fluorescence intensity increase ($\Delta F/F$). **D**, maximum intensity projection of cell responses of the whole VNO depth. Colors code the depth from which each maximum intensity originated, with magenta for the superficial layers (the knobs) and blue for the deep layers (the cell body layer). This representation is independent on any manual segmentation, yet note the consistency of magenta signals with that from manually assigned dendritic layer in B, and the consistency of blue signals with that from cell body layer in C. The 1:1 correspondence between magenta and blue signals (equivalent to red signals in B and C) indicated that most cells showed consistent calcium signals at both layers. While the calcium signals at the dendritic knobs were occasionally more intense, the relatively larger size and more regular shape of cell bodies made the image registration and cell segmentation more reliable. In this study, all the cell responses were measured at the somata. Scale bar, 50 μm.
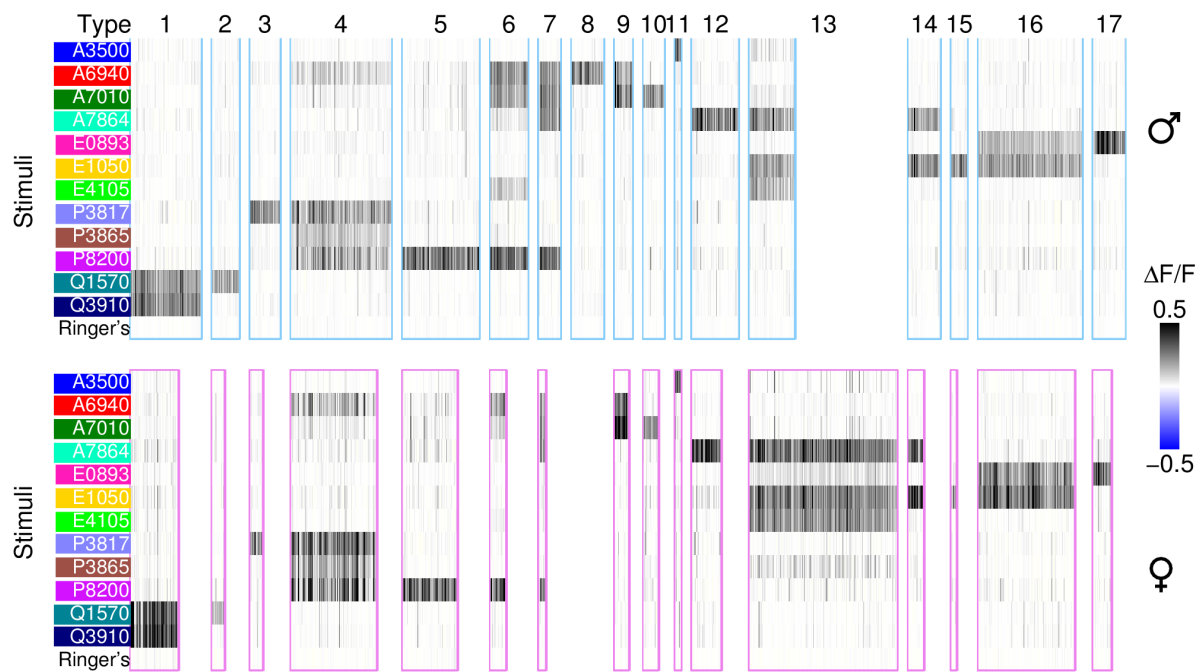
Figure 3.6. **Physiological types of VSNs in single male (upper) and female (lower) imaging volume.** Each thin column of the heatmap represents a single cell; gray intensity is the average induced fluorescence change $\Delta F/F$ across 4 trials. For the 17 main physiological types, all but type 8 were present in both and female mice. Type-8 VSNs were only detected in the male VNO.

However, this analysis also revealed a dramatic example of sexual dimorphism. VSN type 8, responding selectively to epitestosterone sulfate (supplementary video 2), was found almost exclusively in male mice (Fig. 3.7b–e, supplementary video 3 & 4). In all 6 male VNO imaging volumes, an average of 23 (23.2 ± 4.8, mean±s.e.m.) type-8 cells were found in each male imaging volume, yielding a total of 139 type-8 cells across all 6 imaging volumes (Fig. 3.7b & d). In contrast, only one clear example of a type-8 cell was found in 5 imaging volumes from females (Fig. 3.8). Across preparations, this male/female difference, at least one-hundred fold, was highly significant even when corrected for multiple independent comparisons ($p = 0.0014$). In addition to type 8, we found that type-6 neurons, responding strongly to epipregnanolone sulfate and more weakly to certain androgen sulfates, also differed significantly ($p = 0.0016$) between males and females, by a ratio of approximately two-fold (male 49.0 ± 3.8, and female 20.2 ± 5.4, mean±s.e.m.)(Fig. 3.7b).

To test whether the apparent absence of type-8 neurons from females might be an artifact of clustering, we performed a second analysis in which neurons most similar to type 8 were examined regardless of their clustering classification. This analysis did not reveal any additional type-8 candidates among the female imaging volumes (Fig. 3.8). We also wondered whether females might have type-8 neurons that were less sensitive than those in males. We therefore performed a subset of experiments using mice expressing the more sensitive GCaMP3 [27] in VSNs, and interrogated the neuronal responses to a range of concentrations, up to $100\mu M$, of sulfated steroids (Fig. 3.9). This approach detected 1–2 fold more total epitestosterone sulfated-responsive cells (GCaMP3 vs. GCaMP2: 200.0 vs. 162.8 for males, and 268.0 vs. 104.4 for females); in males, type-8 neurons were
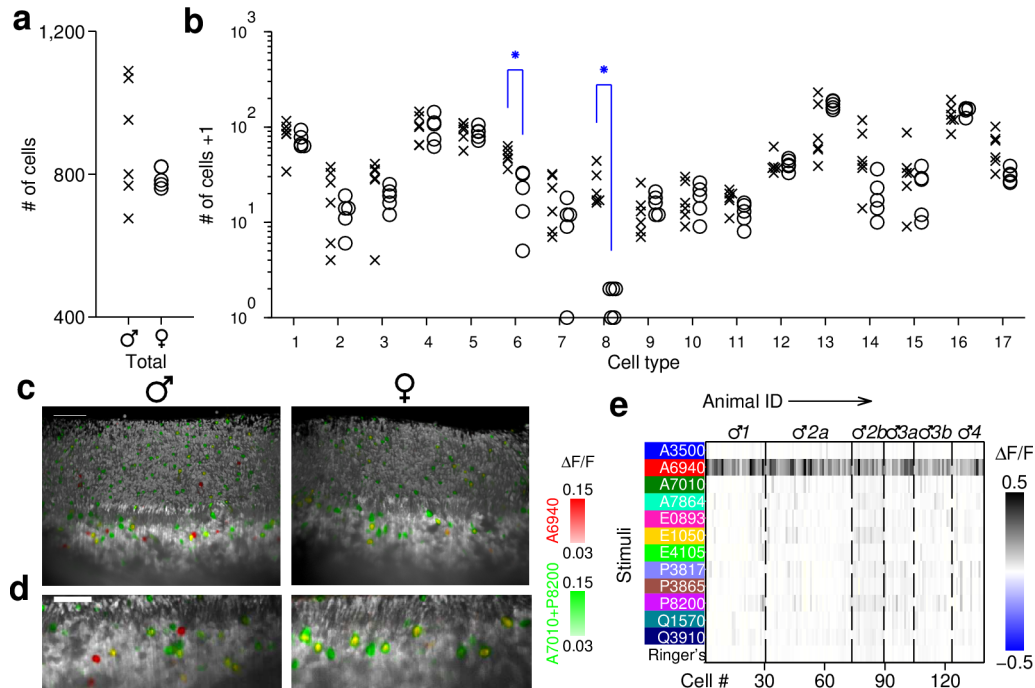
Figure 3.7. **Physiological neuronal types in VNOs from male and female mice.**
a&**b**, cell counts in each male ($\times$) and female ($\circ$) VNO imaging volume, in terms of
total number of steroid-responsive cells (a) and number of cells of each VSN physio-
logical type (b). Type 6 and type 8 were more abundant in male than in female mice
($*$, $p = 0.0016$ and $p = 0.0014$, respectively, Students' t-test, significance tested with
Ŝidák correction for multiple comparisons). Note logarithmic scale. Three-dimensional
images (**c**) and two-dimensional slices (**d**) of male and female VNOs. Red indicates the
fluorescence change caused by epitestosterone sulfate (A6940) ($\Delta F/F_{A6940}$), and green
colorizes $\max(\Delta F/F_{A7010}, \Delta F/F_{P8200})$. Type-8 cells, exclusively responsive to A6940,
are therefore red; note these were present only in the male VNO but not in the fe-
male VNO. Responses induced by P8200 (green) were particularly intense and spread
to neighboring pixels, producing a green halo around the yellow cells. Scale bar, $50\,\mu$m.
e, type-8 VSNs were found in all 6 male VNO imaging volumes (from 4 individual male
mice). Dashed lines separate cells from different imaging volumes. Each imaging volume
is labeled with the animal's identity; multiple imaging volumes collected from the same
animal are differentiated by letters.
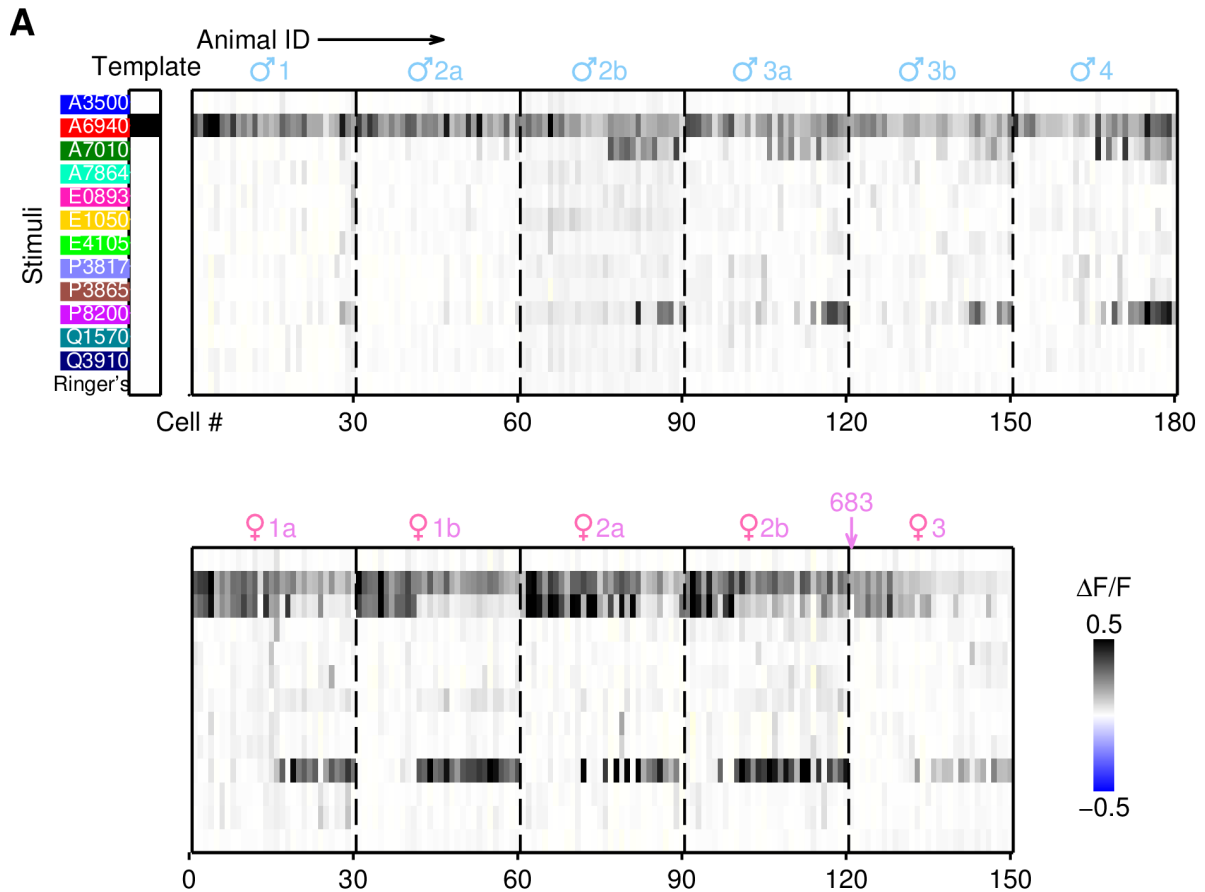
Figure 3.8. **A clustering-free analysis shows that epitestosterone sulfate (A6940)-selective VSNs were specific to male mice. A**, upper Left: a template "artificial cell" responding exclusively to A6940; this template was used to "fish out" the 30 cells with most similar response pattern (smallest Euclidean distance between normalized responses) from each imaging volume. Within each imaging volume (separated by dashed lines), cells were arranged in decreasing order of similarity to the template. Each column represents a single cell; gray intensity is the average $\Delta F/F$ across 4 trials. Each imaging volume is labeled with the animal's identity; multiple imaging volumes collected from the same animal are differentiated by letters. Top, all 6 experiments from male mice (N = 4 animals) contain cells that responded selectively to A6940. Bottom, in females only a single neuron, indicated by the arrow, showed a similar response profile from all the 5 female VNO volumes (N = 3 animals). Note that Fig. 3.7a shows 3 female type-8 cells, but 2 of them were suggested to be false positives upon inspection ($\Delta F/F$ "spillover" from adjacent cells with strong responses). **B**, the $\Delta F/F$ traces of the top three cells from each imaging volume. Color bars represent different stimuli, red for epitestosterone sulfate (A6940). Cells "fished" from male imaging volumes responded to A6940 exclusively, reproducibly in all 4 trials. Spontaneous activity was detected as small peaks that were not typically coincident with stimulus onset.

B

Trial # 1 2 3 4

♂1: Stimuli, Cell499, Cell500, Cell224

♂2a: Stimuli, Cell371, Cell851, Cell14

♂2b: Stimuli, Cell366, Cell467, Cell582

♂3a: Stimuli, Cell860, Cell742, Cell738

♂3b: Stimuli, Cell256, Cell728, Cell553

♂4: Stimuli, Cell782, Cell771, Cell781

♀1a: Stimuli, Cell820, Cell232, Cell749

♀1b: Stimuli, Cell413, Cell259, Cell668

♀2a: Stimuli, Cell724, Cell557, Cell720

♀2b: Stimuli, Cell523, Cell780, Cell18

♀3: Stimuli, Cell683, Cell442, Cell463

$\Delta F/F$ 0.5

5 min

64

present at levels comparable to the GCaMP2 experiments (21.0 ± 4.0 vs. 23.7 ± 4.8, mean$\pm$s.e.m)(Fig. 3.9A&B), while in females no clear examples of type-8 neurons were found (Fig. 3.9E&F).

The hundred-fold sex difference of type-8 neurons represents the largest sexual dimorphism reported for the mammalian nervous system, and to our knowledge the first difference observed at the level of neurophysiology [102–104, 109]. In addition to this difference in mean cell counts between males and females, we noted that males were substantially more variable than females: in females, the variability of 11/17 types was not distinguishable from random sampling, but this was true for only 3/17 in males (Fig. 3.10); the rest were more variable than one would expect by chance.

3.1.5   Mechanism of sexual dimorphism: experience

To explain sexual dimorphism in animals and humans, three mechanisms are typically invoked: a difference of genes (X and Y chromosomes), a difference of hormones (androgens and estrogens), and a difference of experience (e.g., expectations and conditions of rearing) [104, 143, 144]. For vomeronasal sensory neurons, the first two biological explanations might initially appear to be most plausible [112, 116, 145–147]. However, the corresponding biological manipulation would change the animal's hormones and metabolites thereof [78, 148, 149]. Because vomeronasal neurons detect steroid metabolites [97], such manipulations would also substantially change the animal's sensory experience of its own scent. Thus, we decided to first test whether a mouse's long-term olfactory experience affects the composition of sensory neuronal types in males and females.
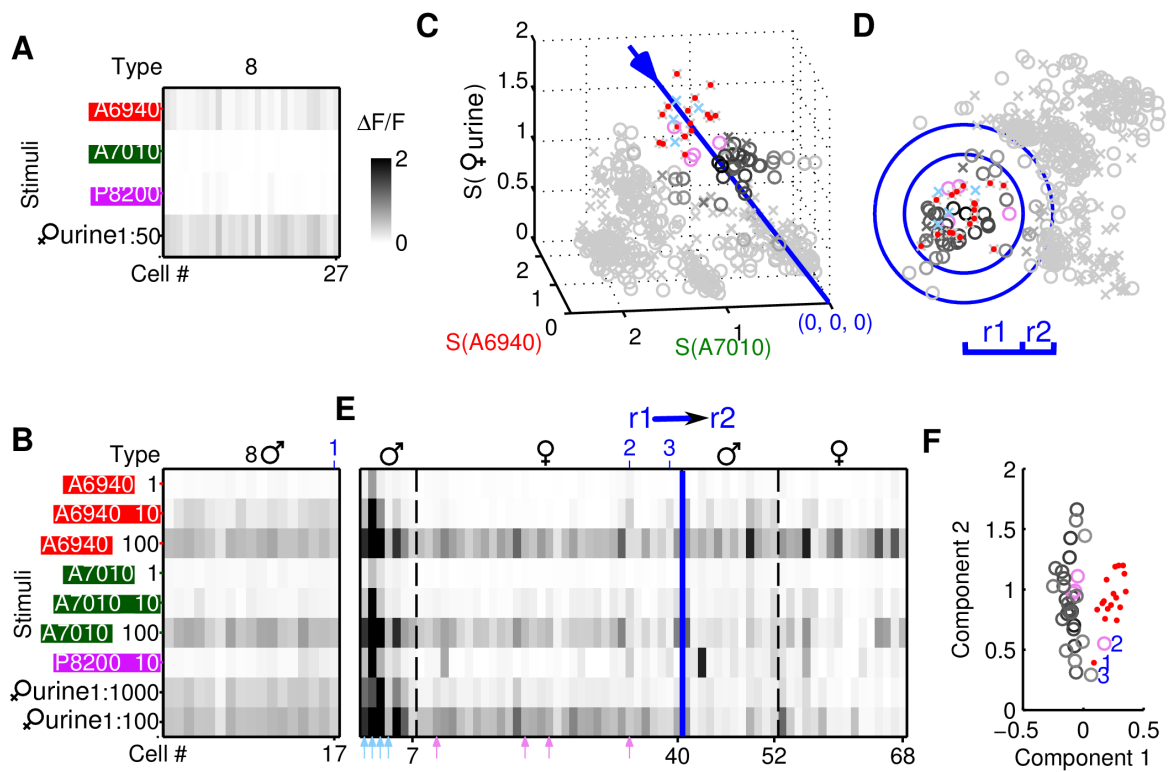
In total, we examined six different categories of individuals: isolation-housed males and females (as shown in Fig. 3.7), females exposed to either a male or a female, and males exposed to either a male or a female. To provide long-term exposure to chemical cues from other animals without allowing sexual behavior or intense social contact, we designed two-layer stacking cages to house mice (Fig. 3.11a) that permit chemical cues from the upper animal to fall down to the animal in the lower cage. After 9–13 weeks (matching the duration of isolation-housing in the previous experiments), we removed the

---

Figure 3.9. *(preceding page)* **VSN responsiveness to concentration series of sulfated steroids and female urine tested by GCaMP3 VNOs.** Type-8 VSNs recorded from a male GCaMP2 VNO (**A**) and GCaMP3 VNO (**B**). The shown GCaMP2 VSNs came from clustering result in Fig. 3.2d. The shown GCaMP3 VSNs were classified as type 8 according to their responsiveness to $10\,\mu M$ A6940, A7010 and P8200. The colorized stimulus bars including the unit (for $10\,\mu M$) in B highlights the same stimuli as used in A. **C**, for all A6940-responsive cells from GCaMP3 male ($\times$) and female ($\circ$) VNOs, sensitivity (S, sum of normalized responses across concentrations for each chemical) for A6940, A7010 and female urine were plotted in three-dimensional space. Type-8 cells were marked by •. The nearby cells that were not computationally (see Methods) identified as type-8 were colorized for each sex (male ×, female ○). Putative type-8 cells with lower sensitivity, if present, would be located close to the blue line that goes through the center of type-8 cluster and the origin. The distance of each cell (unless otherwise colorized) to the blue axis is coded by the darkness of the marker. **D**, two-dimensional projection of all cells along the blue axis in C. The concentric blue circles defined by the type-8 center (center of all •) encompass potential type 8-like cells. The full responsiveness of all potential type 8-like cells in the blue circles were shown in **E**, sorted by ascending distance to the type-8 center. Note this approach detected a cohort of cells (mostly within r1 distance) as the top candidates of type 8-like cells in females. Note that these neurons showed similar sensitivity to male type-8 neurons to A7010, but were of approximately ten-fold lower sensitivity to A6940 and female mouse urine, indicating that they likely represented a different cell type. **F**, linear discriminant analysis (LDA) of type-8 cells (•) and female neurons within r1 in pannel E. The two LDA components were obtained after an unbiased k-means clustering ($k = 3$) of cells. Note the almost perfect separation between male type-8 neurons and the nearest candidates in females. The three numbered cells in the overlap region are also indicated in B&E; cells 2 and 3, from females, were not type-8 cells as they responded to P8200 (panel E), a difference that was not well-captured by these two LDA components.

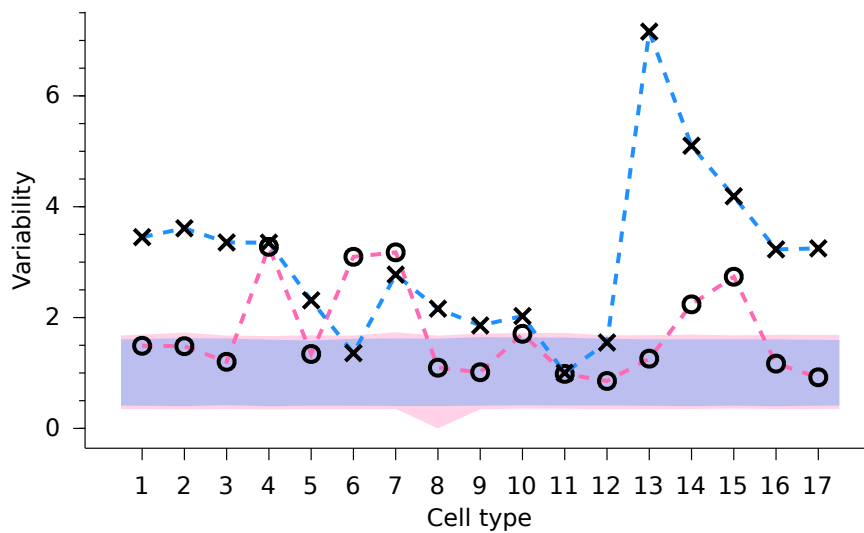Figure 3.10. **Variability of isolation-housed male (×) and female (○) mice.** For each sex, cell count variability of each type, and 95% confidence interval for Poisson random sampling, are shown as in Fig. 3.2f. The confidence intervals are shown in pink and blue for the female and male groups, respectively. Within-sex variabilities were not distinguishable from random sampling in 3 (male) and 11 (female) cell types.

vomeronasal organ from the lower animal and imaged responses to these same sulfated steroids.

For vomeronasal organs from female mice, exposure to male chemical cues caused the total number of steroid-responsive neurons to decrease slightly (Fig. 3.12A; $p = 0.0357$). While it appeared that some cell types responding to sulfated androgens and estrogens (type 9, 12, and 13) were somewhat rarer (Fig. 3.12B &C), no individual case was significant when corrected for multiple comparisons ($p = 0.0470, 0.0320, 0.0133$). Crucially, for these females exposed to the males, we still did not detect evident type-8 VSNs: only a single clear type-8 cell was found in all 5 image volumes. Consequently, females with long-term exposure to male cues were virtually indistinguishable from isolation-housed females. Likewise, we found that females exposed to the chemical cues of other females were similarly unchanged (Fig. 3.12).

For vomeronasal organs from male mice, exposure to female chemical cues did not change the total number of steroid-responsive VSNs (Fig. 3.11b). Such exposure also did not change the number responsive to each individual steroid (Fig. 3.13). Such males were therefore able to detect the same cues as isolation-housed animals.

However, in males exposed to females, the sexually-dimorphic type 8 (selective to epitestosterone sulfate A6940) was virtually absent (Fig. 3.11c–e, Fig. 3.14, and supplementary video 5). In 4 imaging volumes, we did not observe any type-8 VSN, a marked contrast with isolation-housed males (139 such neurons in 6 imaging volumes, $p = 0.0017$). This difference was not due to generic social experience, as males exposed to the secretions of other males had type-8 neurons present in numbers not significantly
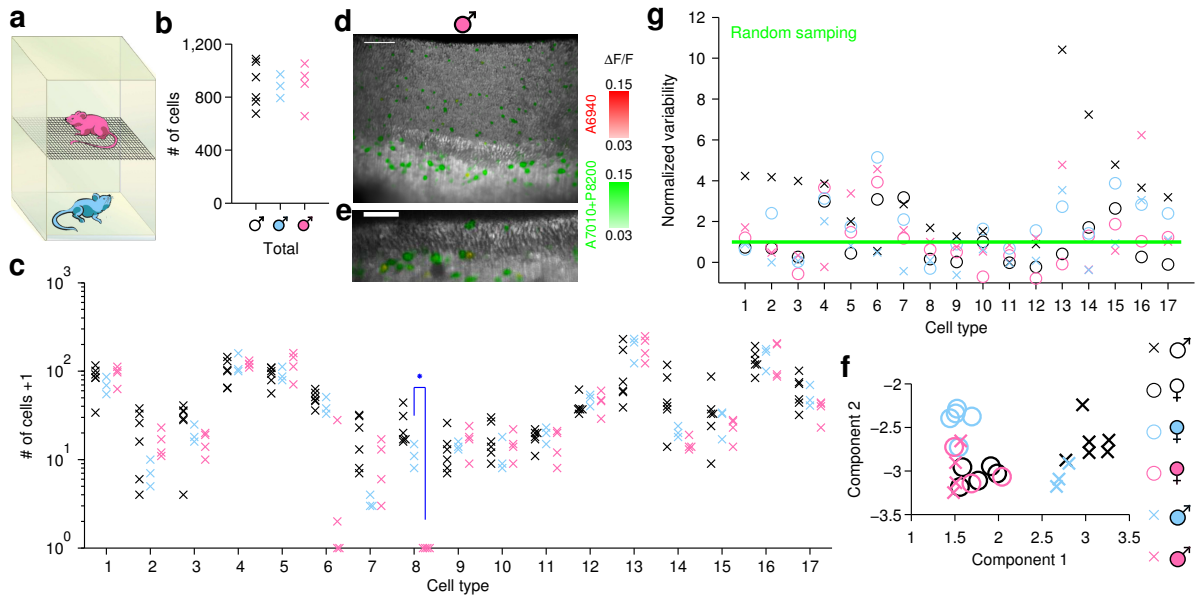
Figure 3.11. **Exposure to female scents triggers the disappearance of a male-specific VSN type. a**, stacked cages provide chronic exposure to chemical social cues without permitting aggressive encounters or mating. **b** &**c**, number of cells in each male VNO imaging volume: (×) isolation-housed male, (×) male housed below another male mouse, and (×) male housed below a female mouse. b, total number of cells responding to sulfated steroids; c, number of cells in each specific VSN physiological type. Type-8 cells showed a dramatic decrease in abundance in males exposed to females (*, $p = 0.0017$, Students' t-test, significance tested with Ŝidák correction for multiple comparison). **d** &**e**, three-dimensional rendering and two-dimensional slice of a VNO imaging volume from a male mouse exposed to a female. Coloration is identical to Fig. 3.7c &d. The absence of red cells indicates the absence of type-8 VSNs in males exposed to female, in contrast with isolation-housed males in Fig. 3.7c &d, and male-exposed males in Fig. 3.14. Scale bar, $50\,\mu$m. **f**, whole-animal view of VNO cell-type composition from different groups of mice. A linear-discriminant projection onto the two components with largest eigenvalues are shown. Isolation-housed males (×) and females (∘) were well separated; males exposed to female cues (×) would be grouped with females (note overlap with circles). **g**, normalized variability for each group of mice with the same sex and experience. For the 6 groups of animals, the numbers of cell types with variability consistent with random sampling (below the green line) were 3 (×), 11 (∘), 5 (∘), 8 (∘), 12 (×) and 9 (×) out of 17 types.
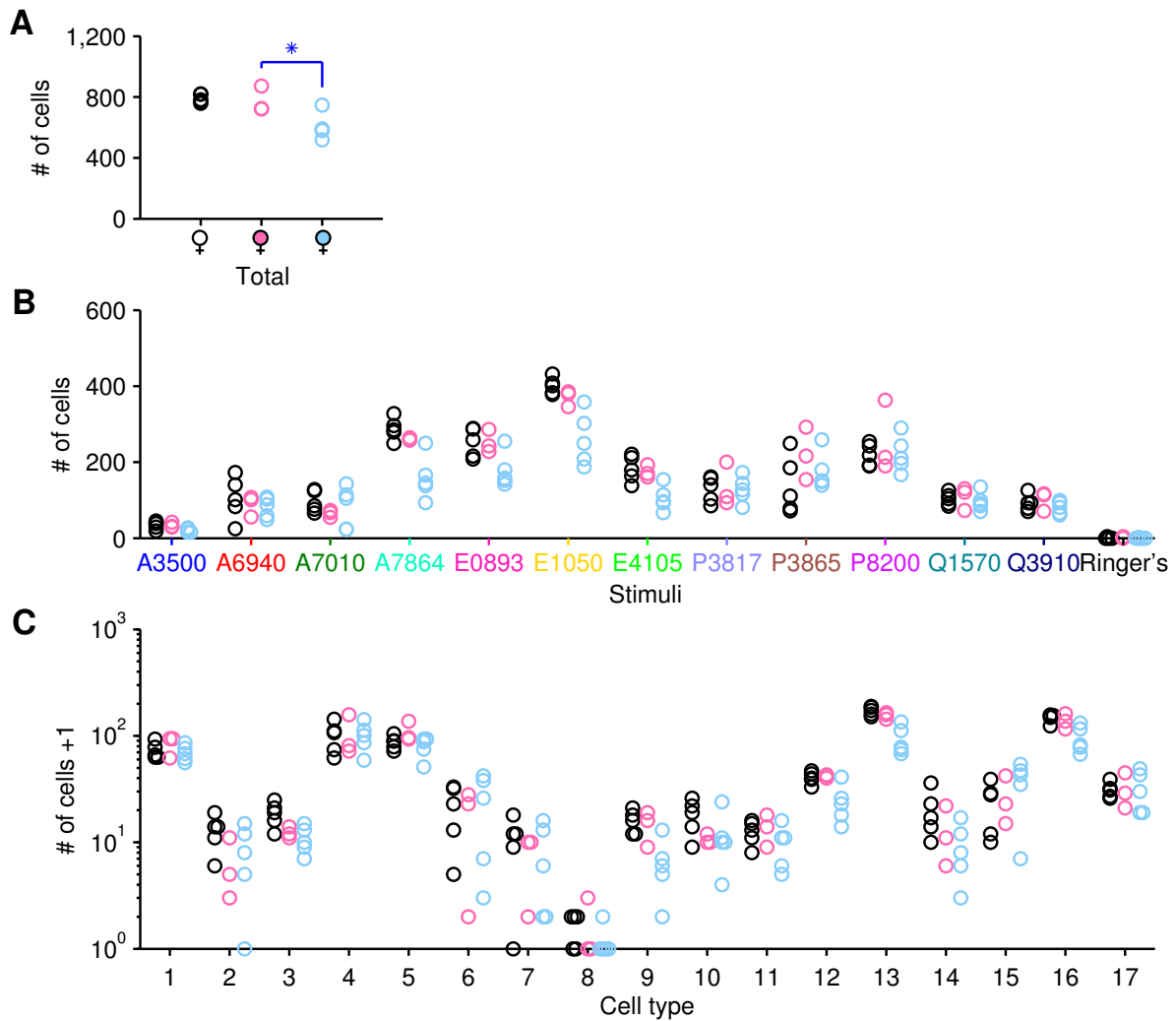
Figure 3.12. **Social exposure does not dramatically change the steroid response profiles of VSNs in female mice.** Isolation-housed female (○), female exposed to another female (○), and female exposed to a male (○). **A**, total number of steroid-responsive cells; **B**, number of cells responding to each stimulus; **C**, number of cells in each specific VSN physiological type. The total number of steroid-responsive cells decreased after male exposure (∗, $p < 0.05$, Students' t-test), but neither the number of cells responsive to any of the individual steroids nor the number of individual physiological types independently reached significance (familywise significance level $\alpha = 0.05$, Students' t-test with Ŝidák correction for multiple comparisons).
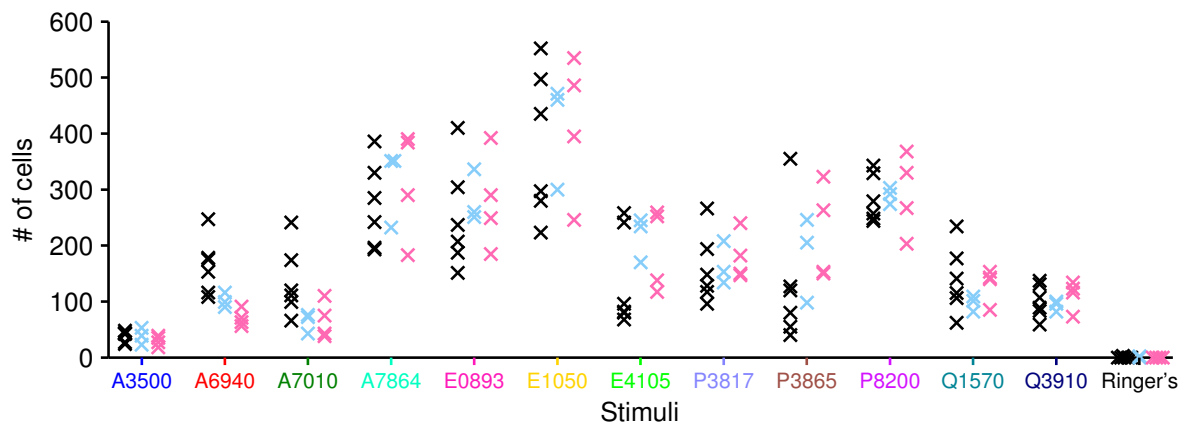
Figure 3.13. **Effects of sensory experience on males were seen only via decomposition by VSN type, not on a per-ligand basis.** Total number of steroid-responsive cells in male mice with sensory experience. No significant difference was found when isolation-housed males ($\times$) were compared to male-exposed males ($\times$), nor to female-exposed males ($\times$) (familywise significant level $\alpha = 0.05$, Students' t-test with Ŝidák correction for multiple comparison). Differences shown in Fig. 3.11c emerge only when responses are broken down by VSN physiological type.

different from isolation-housed animals ($p = 0.1020$, Fig. 3.11c, and supplementary video 6).

To provide an unbiased view of the distribution of VSN types at the level of whole animals, we performed a linear discriminant analysis of the features that best distinguished among animals with different sexes and history of sensory experience. Consistent with the result for types 8 and 6, we found that exposure to female cues "converted" male VNOs into a pattern of responsiveness indistinguishable from that of females (Fig. 3.11f), suggesting that experience, not sex, determines the composition of VSN types. We also examined the individual variability within these six groups, and found that animals with the same sex and experience exhibited variability consistent with random sampling in approximately half of the type/experience conditions (48/102, Fig. 3.11g), remarkably different from the result of 0/17 cases when combining animals from different groups (Fig. 3.2f). Thus, much (but not all) of the individual variability we observed stems from the different explicit sensory experiences we provided to these animals.

3.1.6 Experience-dependent plasticity: use it *and* lose it

Exposure specifically to female cues led to the near-absence of the particular VSN type — type-8 neurons — from the vomeronasal organ. To determine whether the disappearance of type-8 neurons from males was due to direct exposure of VSNs or an altered hormonal milieu triggered by the scent of females [150, 151], we occluded one naris in each male throughout the exposure period, thereby giving both sides the same exposure to circulating hormones but differing sensory experience. Dye-tracing demonstrated the effectiveness of unilateral naris occlusion in limiting exposure of the VNO to chemical
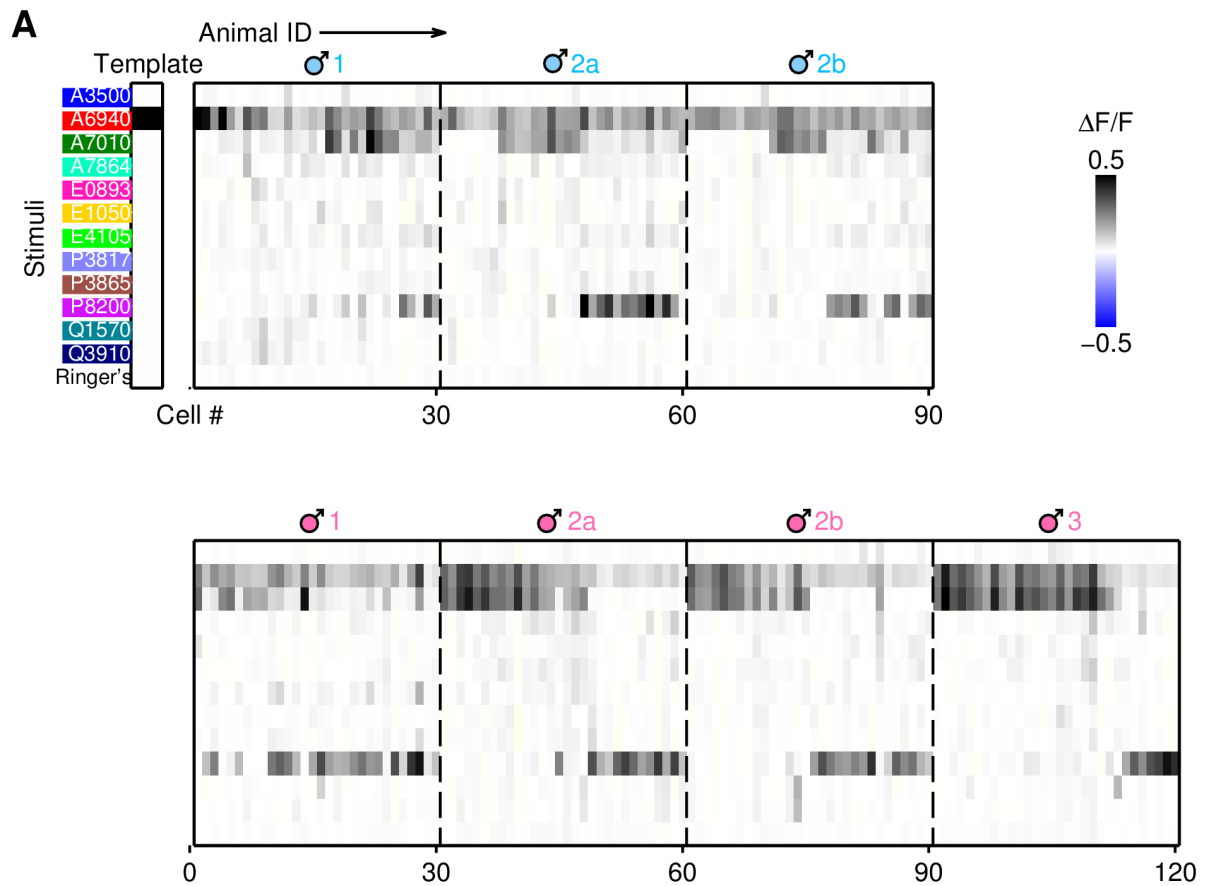
Figure 3.14. **A clustering-free analysis shows that male mice exposed to female lost epitestosterone sulfate (A6940)-selective VSNs. A**, upper Left: a template artificial cell, as described Fig. 3.8. In contrast with isolation-housed males (Fig. 3.8) and male-exposed males (upper, 2 animals, 3 imaging volumes), males that had been exposed to females (lower, 3 animals, 4 imaging volumes) did not show A6940-selective VSNs (type-8 VSNs). **B**, the $\Delta F/F$ fluorescence traces of the top three cells from each imaging volume. Color bars represent different stimuli, red for epitestosterone sulfate (A6940). Top cells from imaging volumes of male-exposed males exclusively responded to A6940 (similar to males in Fig. 3.8), but top cells from female-exposed males responded to more than just A6940 (as with females in Fig. 3.8).
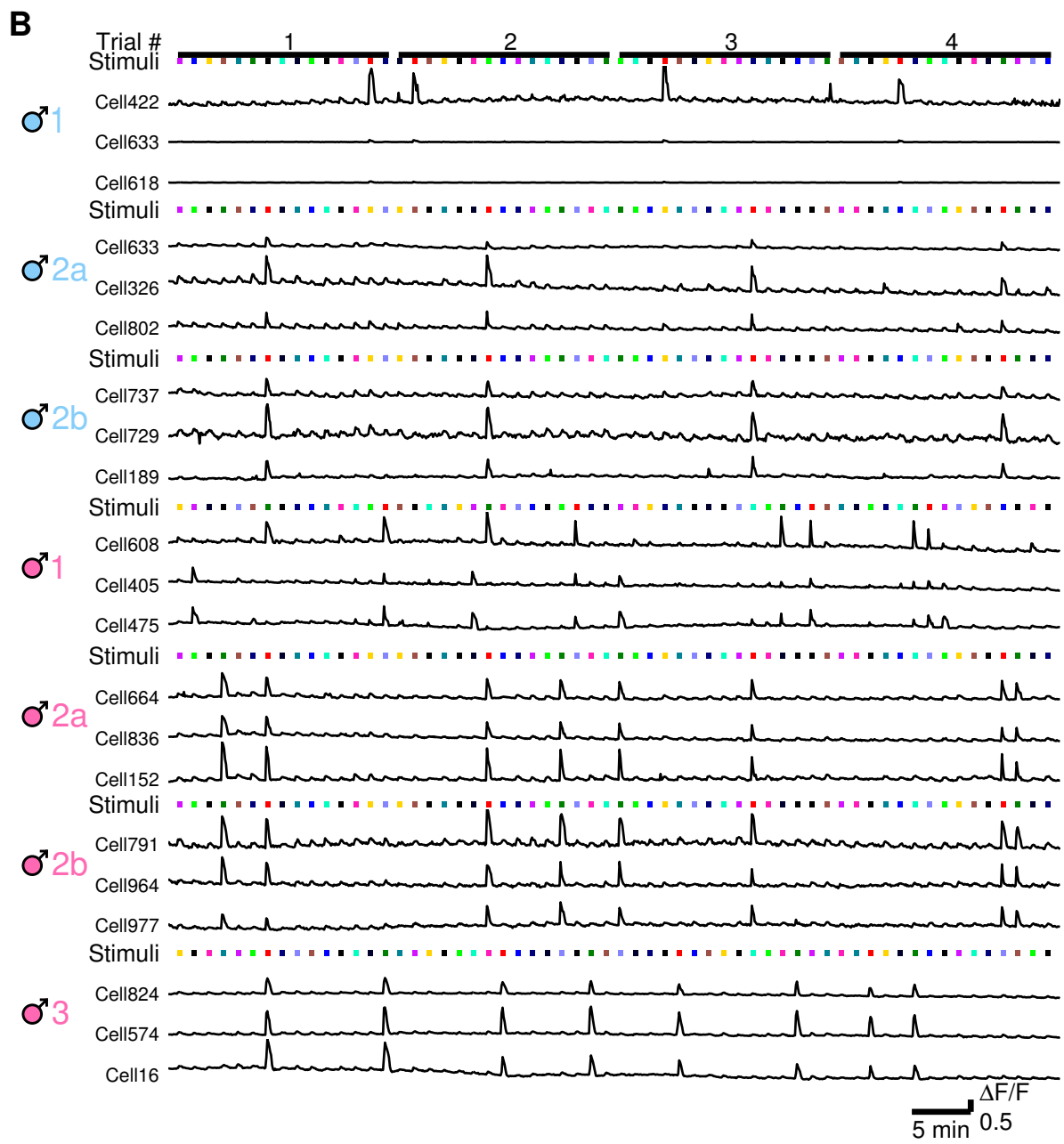
cues (Fig. 3.15a). When the two sides were isolated and tested physiologically, VNOs from the open side had no type-8 neurons. In contrast, VNOs from the closed side possessed type-8 neurons as observed in unexposed males (Fig. 3.15b). This indicates that sensory experience, rather than circulating hormones, is the determining factor in this form of plasticity.

In addition to type-8 neurons, we also found that the more modestly-dimorphic type-6 neurons, primarily responsive to P8200 and A6940, tended to be suppressed in males exposed to females ($p = 0.0156$, Fig. 3.11c). To learn more about why these two types, and not others, showed evident experience-dependent plasticity, we tested how the different neuronal classes responded to female mouse urine, a dominant source of chemosensory cues during the exposure period. Urine perceptibly activated just 3 of the 17 types, which were type 8, type 6, and (most weakly) type 11 (Fig. 3.15c & d). This result provides a natural explanation for selective plasticity: neuronal types responding most strongly to the stimulus were those that exhibited the greatest reduction in number. Type-8 neurons, the type exhibiting strongest plasticity, were also absent in isolation-housed males presented with nestlets soaked with female urine or epitestosterone sulfate solution (Fig. 3.15f), further demonstrating that activation of these particular neurons led to the observed plasticity. Moreover, this use-dependent loss is not restricted to these particular cell types, but instead represents a general mechanism regulating VSNs, as the total female urine-responsive cells (including non-steroid-responsive cells) showed a three-fold reduction after female cue exposure(Fig. 3.15e)(see supplementary discussion).

Finally, we identified the developmental factors controlling this plasticity. To determine whether this plasticity was confined to the early post-weaning period, instead
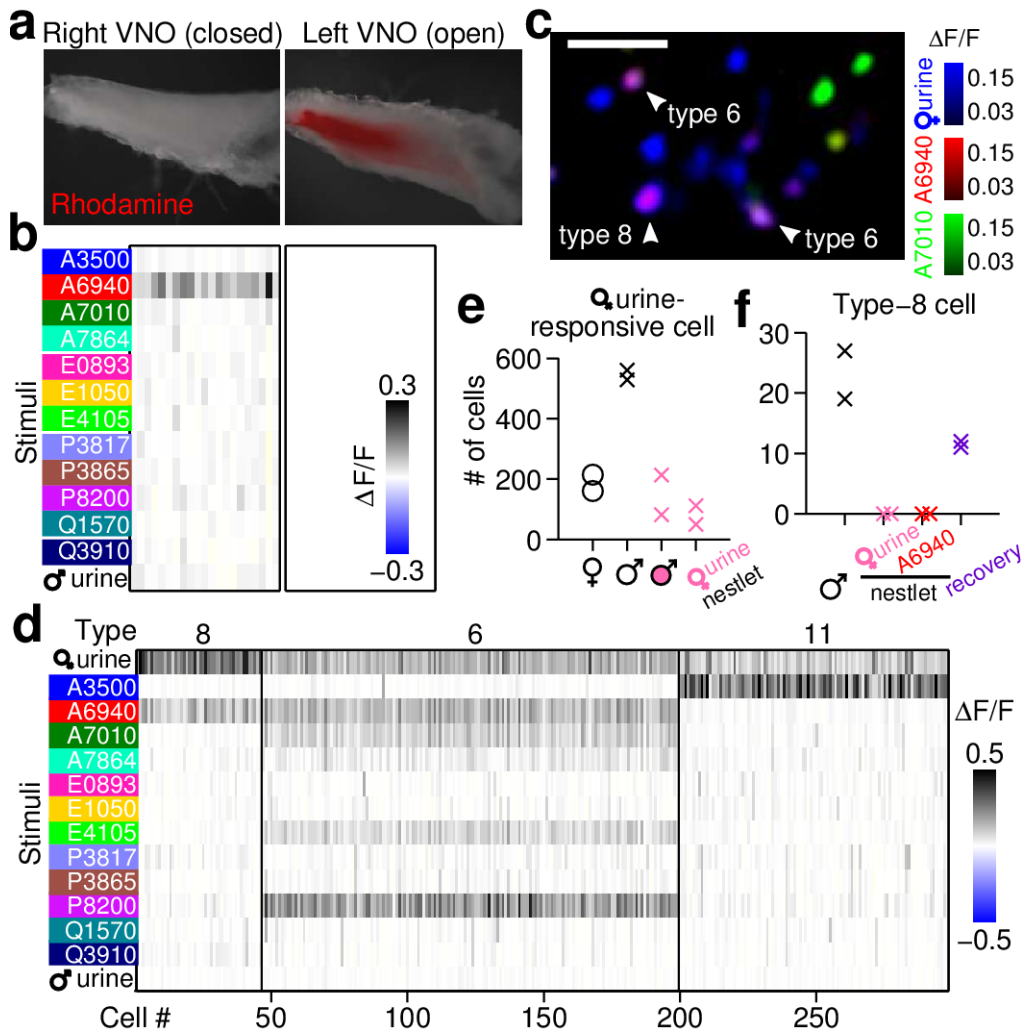
Figure 3.15. **Plasticity is a consequence of sensory activation. a**, two VNO tissues dissected from the same male mouse. The right naris was closed during the entire exposure period to the female. Chemical access was limited to the open side, as shown by Rhodamine 6G uptake. **b**, type-8 neurons were detected on the closed side, but not the open side ($N = 2$ male mice). **c**, overlap of type-8 and 6 neurons with responses to female mouse urine (1:50 dilution). A two-dimensional slice is shown; arrowheads represent examples of type-8 and type-6 cells that responded to female urine. Scale bar, $50\,\mu$m. **d**, female urine activated type-8, 6 and 11 VSNs, with decreasing strength. All urine-responsive neurons that also responded to at least one sulfated steroid are shown. **e**, the total number of cells responding to female urine (1:50 dilution) in isolation-housed females ($\circ$) and males ($\times$), female-exposed males ($\times$), and males exposed to nestlets with raw female urine ($\times$). **f**, the number of type-8 neurons in isolation-housed males ($\times$), males exposed to nestlets with raw female urine ($\times$) or epitestosterone sulfate solution (A6940, $200\,\mu$M) ($\times$), and males recovered from female exposure (after being exposed to females for 2 months, singly housed for another 3 months) ($\times$). Each marker represents an individual mouse.

of beginning exposure around the weaning age (P21), we began with isolation-housed mature males (7-week-old) and commenced a two-month exposure to females; this experience led to the disappearance of type 8 neurons (Fig. 3.16). We also found that a two-week exposure did not suffice (Fig. 3.16). Finally, female-exposed males that were then re-isolated from females for an additional two months exhibited a partial return of type-8 neurons (Fig. 3.15f). These results demonstrate that this plasticity requires long-term exposure, is not restricted to an early-life critical period, and is at least partially reversible.

3.1.7 Dimorphism and plasticity of behavior

Because type-8 neurons were exclusively activated by epitestosterone sulfate (A6940), we next tested whether males and females responded differently to epitestosterone sulfate at the behavioral level. We presented epitestosterone sulfate on a cotton swab, and used an optical beam-break detector [140] to measure the timing and duration of investigation periods of freely-behaving animals (Fig. 3.18a & b). From initial contact, male mice investigated epitestosterone sulfate ∼25% longer than females (Fig. 3.17A). In terms of the difference from baseline investigation time of a vehicle control (Fig. 3.17B & C), males preferred epitestosterone sulfate (positive effective investigation time, e.g. $1.02 \pm 0.53\,\mathrm{s}$, mean±s.e.m. over $15\,\mathrm{s}$), but females avoided it (negative effective investigation time, e.g. $-1.22 \pm 0.38\,\mathrm{s}$, females vs. males $p = 0.0016$) (Fig. 3.18c). This difference between the two sexes was not observed in the $trpc2^{-/-}$ mice (Fig. 3.17E) for which VSNs are stimulus-nonresponsive [75, 76, 152], indicating that the behavioral differences required functional VSNs. Consistent with the changes in receptor types, female-exposed males
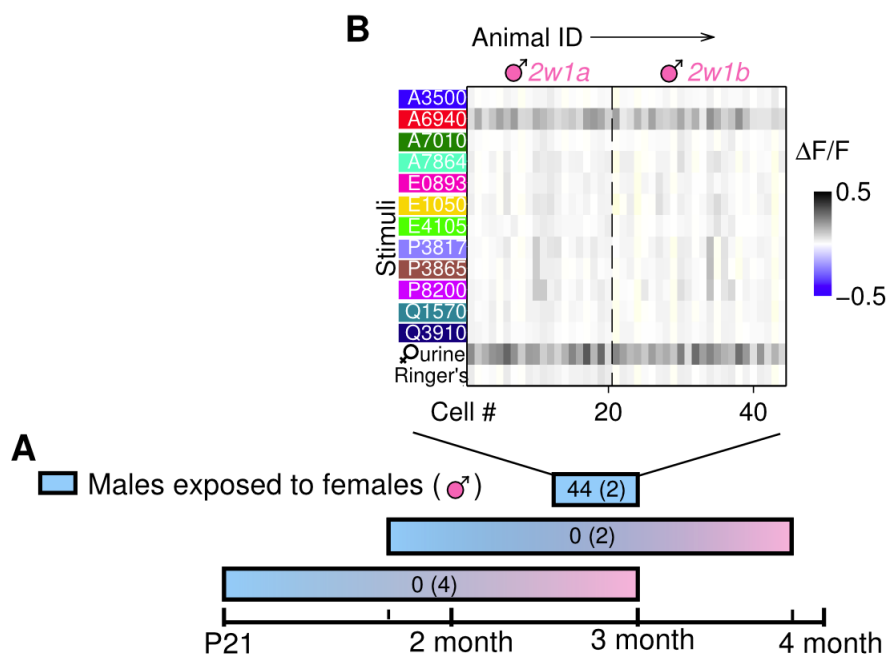
Figure 3.16. **The time window for experience-dependent plasticity of type-8 VSNs.** Male mice were exposed to females at different developmental stages for varying exposure durations. Long-term exposure (~ 2 months), starting from either postnatal day 21 or week 7, caused type-8 VSNs to disappear (4 imaging volumes from 3 male mice, and 2 VNO imaging volumes from one male, respectively); short-term exposure (2 weeks) during adulthood did not affect type-8 VSNs (2 VNO imaging volumes from one male).

did not behave like males but rather, like females, exhibited a relative avoidance (effective investigation time $-1.56 \pm 0.58\,$s, female-exposed males vs. males $p = 0.0026$, female-exposed males vs. females $p = 0.6176$) (Fig. 3.18c, Fig. 3.17D). The investigation time for testosterone sulfate (A7010), an enantiomer of A6940 (Fig. 3.3), was not statistically significant between males and females over any time interval (e.g. females vs. males $p = 0.5991$ over 15 s) (Fig. 3.18c, Fig. 3.17C), consistent with the lack of dimorphism or plasticity in A7010-responsive neurons. The differences in behavioral responses to epitestosterone sulfate were consistent with the distinctive dimorphism and plasticity observed in type-8 neurons.

3.2 Discussion

3.2.1 A clean system for studying the effect of environment on sexual dimorphism

It is widely recognized that the environment has far-reaching influence on self-concept and gendered behavior of humans, yet empirically testing the effects of nature vs. nurture in humans is a formidable challenge because of the number of variables to control. Such control is easier to achieve in rodent models, yet the effect of environment on sexual dimorphism is poorly studied in rodents [143, 144]. The mouse accessory olfactory pathway exhibits dimorphism at multiple circuit levels [110], which from hormonal manipulations like gonadectomy combined with implantation of sex steroids [112, 116, 145, 153–155] has been thought to be a consequence of circulating gonadal hormones [112, 146, 156]. A sexually dimorphic AOS circuit organized by preprogrammed genetic and hormonal factors is seductive, as this very system is documented in the control of innate social behavior,
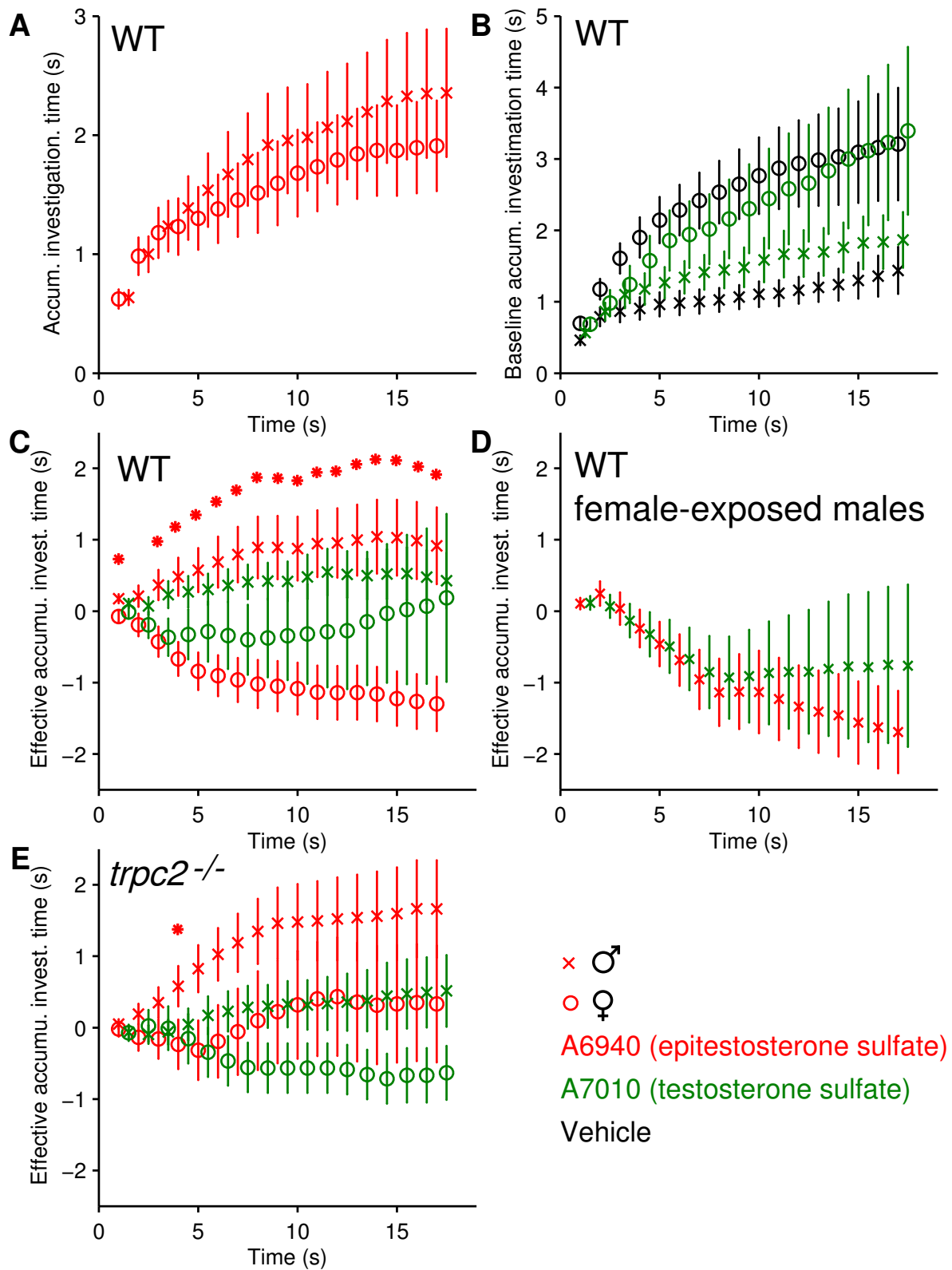
including sexual behavior [73–82], male aggression [74–76, 83–86], interspecies defensive behaviors [87], maternal aggression [76–78, 80, 88] and lactating behavior [77]. However, one potential confound is that studies employing hormonal manipulation could substantially change the metabolites in the animal's urine, saliva, tears, etc. [78, 148, 149, 157], thereby altering the olfactory environment for the animal. Therefore, the relative roles of internal hormones and/or sensory experience in generating AOS circuit dimorphism has not been addressed.

This study found that isolation-housed male and female mice developed functionally different sensory cells, but the differences were diminished if they were housed in the same chemical environment. To directly differentiate hormonal and sensory effects, we exploited the bilaterality of the VNO, with both sides experiencing the same levels of circulating hormones but with just one side receiving sensory exposure. This study provided the first direct evidence that differences in the environment could shape a sexually

---

Figure 3.17. (preceding page) **Investigation time of isolation-housed males($\times$), females($\circ$), and female-exposed males ($\times$) to sulfated steroids at different time intervals since the initial contact.** All trials were aligned to the onset of the initial contact to the cotton swab (time $0\,sec$). **A &B**, raw investigation time to epitestosterone sulfate (A6940), testosterone sulfate (A7010) and vehicle (1:1000 vanilla). The raw investigation time revealed that males and females exhibited differential preference towards epitestosterone sulfate, as controlled by testosterone sulfate and baseline investigation to vehicle for each sex. **C &D**, effective investigation time, calculated by subtracting baseline investigation time measured with vehicle solution. Males ($\times$, N = 10, 3 trials) spent more time sniffing A6940 than females ($\circ$, N = 10, 3 trials) (*, $p < 0.01$, Students' t-test), but there was no significant difference for A7010 ($p > 0.05$ for any interval). **D**, effective investigation time of female-exposed males were not significantly different from that of females in C. **E**, $trpc2^{-/-}$ mice did not show significant sexual difference to neither A6940 (except at a single time interval, over $4\,sec$ after initial contact) nor A7010.
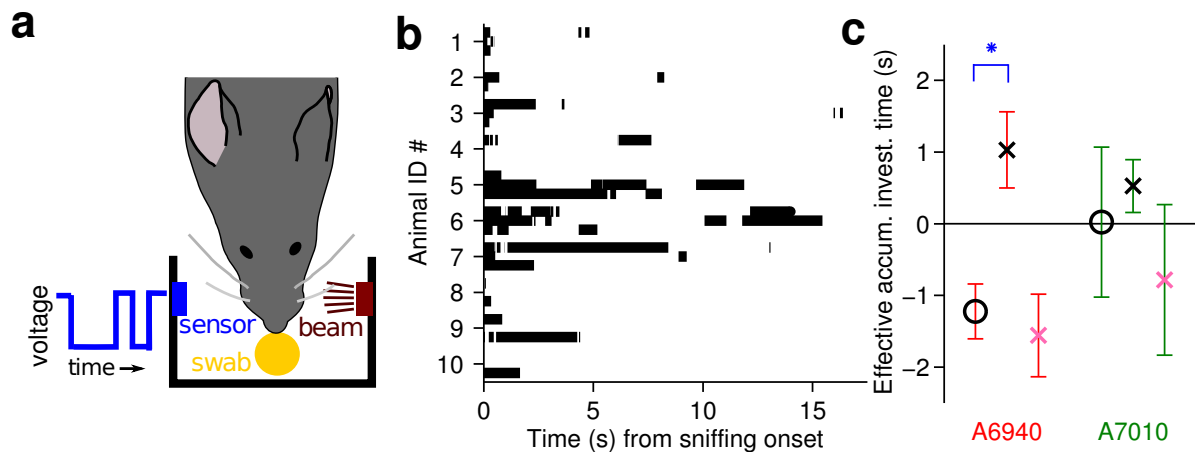
Figure 3.18. **Olfactory investigation of epitestosterone was sexually dimorphic and determined by experience**. **a**, schematic of apparatus used to record episodes of olfactory exploration in freely-behaving animals. The infrared beam was broken (see the blue voltage trace) when the mouse contacted the cotton swab. **b**, investigatory episodes of 10 male mice to epitestosterone sulfate. Each animal participated in 3 trials, each of which was aligned ($t = 0$) to the time of first contact. Black blocks represent continuous periods of investigation. Blank trails were "failure trails" in which the animals never investigated the cotton swab. **c**, investigation time relative to control (see methods, Fig. 3.17) was higher for males ($\times$, N = 10) investigating A6940 than females ($\circ$, N = 10) ($*$, $p = 0.0016$, Students' t-test), but did not differ for A7010 ($p = 0.6176$). In contrast, female-exposed males ($\times$, N = 12) were indistinguishable from females ($p = 0.5991$).

dimorphic neural structure. The remarkable role of environment in forming sexually dimorphic circuitry may have far-reaching consequences, with interesting implications even for the discussion of human activities such as school performance and the workplace [158].

3.2.2   Mechanism of experience-dependent plasticity of VSNs

We observed that responsive male-specific type-8 and type-6 neurons disappeared, or diminished in number, after chronic exposure to females, and further demonstrated that female urine, the major source of female secreted chemicals, activated these neurons. In contrast, cell types unaffected by female exposure were not activated by female urine, with the exception of type-11 neurons which exhibited much lower responsive strength compared to type 8 and type 6 (Fig. 3.15d). We also directly stimulated type-8 neurons by presenting nestlets soaked with female urine, or soaked with epitestosterone sulfate (A6940) solution, on a daily basis for 3 months. In both experiments, type-8 neurons completely disappeared (Fig. 3.15f).

"Adaptation" has been proposed to explain the lack of *c-fos* activation in the BALB/c male VNO after ESP-1 exposure [81] as well as down-regulation of pup pheromone-induced *c-fos* activation [86]; however, the decrease in *c-fos* signals may alternatively reflect reduced investigation of familiar chemicals [117] instead of a change in sensory capacity. The existing physiological evidence—a more direct measure than *c-fos* of neuronal function—is quite limited in terms of the number of responsive neurons: one multielectrode array study of 320 single-units observed ESP1 responses in 3 neurons from females and 2 neurons from males [77], while a second data set observed 3/166 responsive

neurons in females and 0/66 responsive neurons in males [97]. These results indicate the presence of at least some ESP1 responses in males, and are therefore consistent with the possibility that the decrease in fos-positive cells was a consequence of reduced investigation rather than innate VSN functional differences.

One possible mechanism for changes in cellular function is altered gene expression, particularly of the vomeronasal receptors themselves. To date, no vomeronasal receptor genes have been mapped to the Y chromosome [159]. Studies of the influence of experience on gene expression in VSNs (vomeronasal receptors and otherwise) [114, 124] showed maximal changes of approximately 2-fold, insufficient to account for the size of phenomenon we observed in type-8 neurons. It is not known whether the reported changes corresponded to different numbers of cells or changes of expression level within cells. Likewise, none of the vomeronasal receptor genes have yet been found to be expressed differentially in male and female animals [94,95,114]. The closest known example is a difference, for cells expressing a particular V2R gene, of the mean soma depth within the VNO epithelium between the sexes [95]. However, because all VSNs receive sensory exposure through their dendritic knobs at the surface of the VNO, there is no known functional consequence of a shift in the location of the soma; moreover, this receptor gene is thought to be a pseudogene [98].

Hagendorf et al. discovered an activity-dependent expression of an ether-á-go-go-related gene (ERG)—a potassium channel—in the basal layer VNO [125]. They showed that mice with reduced sensory exposure had reduced ERG expression, while mice exposed to an odor-rich environment expressed higher levels of ERG. For several reasons, this form of plasticity seems unrelated to that observed here. First, ERG is expressed by

the basal V2R neurons, whereas type-8 VSNs reside mostly in the apical zone of VNO (Fig. 3.19). Second, ERG is widely-expressed and does not appear to be restricted to particular functional types. Finally, the specific form of plasticity in the current study is opposite in sign: odor-exposure triggered a loss of type-8 neurons, but ERG expression increased in response to stimulus exposure with a suspected role in repolarizing the membrane to support sustained firing [125].

We tested the time window for expression of this plasticity, and found it required approximately 2 months—a period long enough for sensory neuron turnover in VNO epithelium [142] (Fig. 3.16). The plasticity of type-8 VSNs existed at both developmental stages and in adulthood. Moreover, we found this plasticity was bidirectional, as re-isolating male mice from females led to the reappearing of type-8 neurons (Fig. 3.15f). These results are consistent with possibility that the observed plasticity of type-8 cell responsiveness may involve type-8 cell death and regeneration. Odor-mediated changes in neuronal survival in the main olfactory epithelium have been documented previously [122, 123]. However, these studies examined sensory neurons in the aggregate, and did not attribute the effect to specific sensory neuron types or patterns of responsiveness. As with Hagendorf [125], the direction of the effect—with stimulation prolonging survival of sensory neurons—appears to be inconsistent with the more selective form of plasticity identified in this study.

3.2.3 Sulfated steroids & behavior

Sulfated steroids, as active ligands for VSNs, were purified from female mouse urine; at present they constitute by far the most active class of known ligands for VSNs
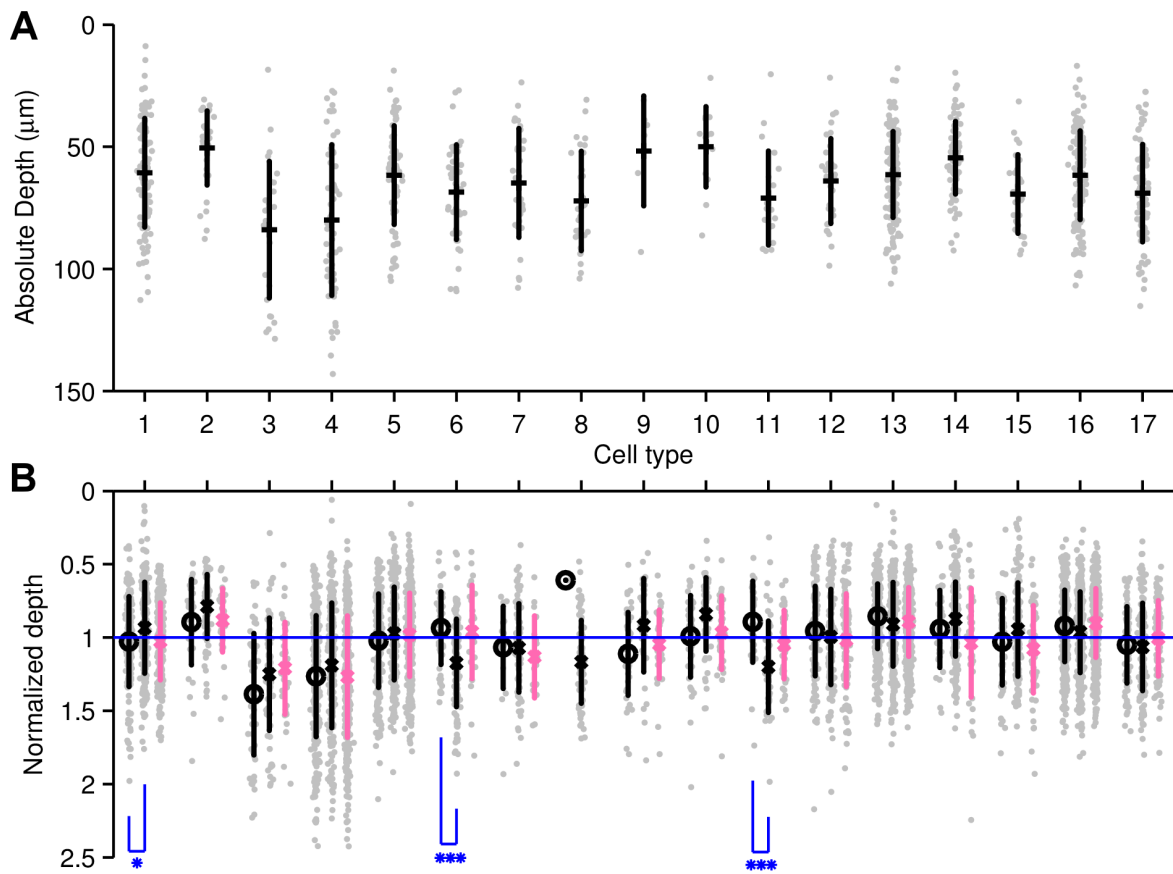
Figure 3.19. **A**, the depth of cells from a single imaging volume of a male VNO tissue. Each gray dot represents a single cell. Depth was calculated as the distance of cell body centroid to the tissue surface. A majority of the types situated in the apical zone of the epithelium, except that pregnanolones-responsive type 3 & 4 were more basally distributed [71]. Male specific type 8 were close to the apical zone, yet more basal than other apical types. **B**, depth distribution of cells from singly-housed females ($\circ$) and males ($\times$), and female-exposed males ($\times$); each group was a pool of cells from 3 individual VNO imaging volumes. To correct for the variation of tissue thickness, all depths were normalized by the average depth of all responsive cells within each tissue. Besides male-specific type-8 cells (with only a single cell found in one of the female VNOs), the other two female-urine responsive types, type-6 and type-11, exhibited significant depth differences between males and females ($\ast\ast\ast$, $p = 6.0 \times 10^{-7}$ and $p = 4.7 \times 10^{-5}$, respectively. Students' t-test), with male cells more basal. Type-1 cells showed a much milder difference ($\ast$, $p = 0.0030$). After female exposure, the depth of remaining male cells of type-1, 6 and 11 were not distinguishable from that of females. Error bars, standard deviation.

[71, 97]. The overlap of epitestosterone sulfate with urine responses in type-8 neurons (Fig. 3.15c &d) might reflect the presence of epitestosterone sulfate in female urine; alternatively, the fact that many VSN types respond to multiple ligands (Fig. 3.2d, Fig. 3.4D) makes it plausible that another, perhaps closely-related, ligand in C57/6 female mouse urine activates type-8 neurons.

While the chemistry and neuroscience of sulfated steroids for the VNO has been the subject of several studies and reviews [71, 97, 160–164], the behavioral role of sulfated steroids has received less attention. It was shown that their concentrations in urine changed according to the physiological status of animals, increasing several-fold in stressed animals [97]. Besides information regarding sex and stress level, the strain identity, social and reproductive status are also potentially encoded by sulfated steroids. However, prior to this study, no direct behavioral impact of vomeronasal detection of sulfated steroids had been demonstrated; this constitutes a further form of novelty for this study. We focused on investigation time, which has been shown to be a sensitive and quantitative indicator of vomeronasal function [165], perhaps because of the slow pumping of stimuli into the VNO [166].

3.2.4 Using imaging technique to study neural individuality at single cell resolution

Individual differences in neuronal circuitry underlie individuality in behavior, but studying these differences at a cellular level in neural assemblies remains a major challenge: circuits contain tens or hundreds of different cell types—and many thousand individual neurons—distributed throughout cubic millimeters (or more) of tissue. Large-

scale recording by light sheet/OCPI microscopy [42] provides one of the few viable strategies for studying systematic functional differences between individuals. Here, by recording from approximately 10,000 neurons per preparation, OCPI microscopy enabled detection of striking individual differences confined to a previously-unrecognized ∼0.2% of the total neuronal population.

3.2.5 A new form of neural plasticity: "use it *and* lose it"

In the nervous system, many known mechanisms of plasticity contribute to the maintenance and strengthening of oft-excited connections; this positive contribution of activity to circuit development and stabilization is often summarized as "use it or lose it." In contrast, the plasticity we discovered in the vomeronasal organ can be better summarized as "use it *and* lose it," because the most strongly-activated neuronal types were most dramatically reduced. We suspect that the strength of this phenomenon is partly due to the controlled sensory environment of the laboratory, and that under natural circumstances with diverse stimuli, all neuronal types may be under a certain amount of sensory-induced competitive pressure. This plasticity might therefore be a reflection of cell-survival or receptor-choice mechanisms that ensure balance in the expression of neuronal types and the ability of organisms to detect a wide variety of scents. This proposed role is consistent with the decreased animal-to-animal variability of females compared to males (Fig. 3.10) and the fact that females produce a substantially-larger number and intensity of vomeronasal cues than males [75, 97, 133, 167]. However, this may not fully explain why isolation-housed males are more variable than males with

access to other males (Fig. 3.11g). It seems likely that additional experience-dependent phenomena contribute to the individual differences among these animals.

3.2.6 A plasticity-caused sexual dimorphism

The vomeronasal system is widely believed to drive "innate" responses to social odors. Many of these behaviors are strongly dimorphic—aggression or mating—and consequently males and females are expected to differ in their underlying neuronal circuitry [111, 168]. Here, we showed that isolation-housed males have at least one type of sensory neuron that is nearly absent in females. It would seem reasonable to expect this difference to have a biological origin, determined by the genes or hormones specific to each sex. Instead, we find that this extreme example of apparent dimorphism is entirely due to sensory experience: exposing males to female cues converts their vomeronasal organs to a female-like pattern. Our finding that neuronal dimorphism is a consequence of plasticity, in a sensory system long held to subserve the innate differences between males and females, brings new mechanistic appreciation of the extraordinary importance of experience and individuality in the development of neuronal circuits and behavior.

3.3 Summary and future directions

Here using large-scale recording by light sheet-based OCPI microscopy we detected striking variability in neuronal functions among mice with difference sexes and experiences. In the context of pheromone sensing neurons, by which mice recognize mates and conspecifics [133, 167, 169], strain difference could be another natural contributor to individual variabilities in a population. According to the experience-dependent plastic-

ity discovered in the current study, the strain-specific social cues per se could result in distinctive functional sensory neurons in each strain thereby causing inter-strain differences. Therefore, testing the individual differences with mice of different strains is one natural extension for the study of individual differences.

Experience-dependent plasticity of pheromone-sensing neurons is one of the key discoveries in this study. At present the cellular mechanism of this plasticity is unclear. The observed "use it and lose it" phenomenon is not reminiscent of the previously reported plasticity (see section 3.2.2), indicating that a novel mechanism for neuronal plasticity exists in those sensory neurons. In order to explain the cellular mechanism, the most straightforward approach is tracking the cell fate during the expression of the plasticity, by which several key questions can be answered:

- whether neurons that no longer respond to stimuli still exist in the vomeronasal epithelium? A pre-labeling of the target cells before chemical exposure will reveal the cell fate.

- If the cells still exist, do they become silenced or switch to a different receptor type? The switch of type can be validated functionally by new stimuli and molecularly by *in situ* hybridization or more efficiently by single-cell sequencing.

- if the cells disappear, we may wonder why normal cell turnover in the epithelium do not replenish this very type. This case will suggest that neuronal activity can biased the receptor choice during neuronal regeneration.

All the above experiments necessitate chronic labeling of specific functional cell types in live animals, which can be achieved by transgenic labeled mouse line. We can either

focus on the type-8 neurons identified in this study, and therefore find the receptor gene(s) to generate the mouse line, or we can consider choose other receptor-ligand pair if the type expresses the same plasticity.

To find the receptor gene for the type-8 VSNs, besides the traditional *in situ* hybridization approaches [160], a new strategy that combines photoactivatable fluorescence labeling and single-cell transcriptomes [170] is another option with much higher efficiency. Currently we do not know any existing receptor-ligand pair that can facilitate the mechanistic study of this plasticity. However, we do know that BALB/c female urine contains corticosterone 21-sulfate [97] that activates type-1 and 2 VSNs (Fig. 3.2d). In a pilot experiment, we exposed mice to BALB/c female cues and observed a decrease in the number of type-1 VSNs and a concomitant increase of type 2 (data not shown), which suggests a potential mechanism of receptor type switching. We still need to further check whether type 1 conforms to the the same plasticity as type 8, yet type 1/2 are potential candidate types for the future mechanistic study.

Chapter 4

In vivo imaging of mouse brain activity with light-sheet microscopy

4.1 Results and conclusions

4.1.1 Horizontal scanning OCPI microscopy (hsOCPI)

In order to refer axes without ambiguity, we first defined five axes as follows: $X - Y - Z$ denote regular coordinates of a sample with Z on the depth axis (vertically when the sample is placed on a horizontal platform); ℓ points in the light sheet propagation direction; and s represents the scanning axis that can vary in different designs (Fig. 1.3). In the first generation OCPI, the scanning axis s is along the axial axis of the objective lens with a 45 tilt angle to the vertical axis. Here, we invented a new scanning modality with s on the horizontal axis overlapping with Y along the surface of the tissue. The new horizontal scanning completely relieves the restriction on the 3D scanning volume of the first generation OCPI. It allows unlimited scanning of tissues with a large surface area. We name it horizontal scanning OCPI (hsOCPI).

In hsOCPI, scanning was achieved by moving the the entire illumination/objective assembly back-and-forth on the horizontal axis through a vertically mounted translating stage(Fig. 4.1). This high performance stage has 19mm travel range with nanometer precision, enabling large-scale scanning with sufficient resolution for most biological studies. The illumination/objective assembly was mounted onto a custom-machined triangular frame that was directly loaded onto the translating stage. In order to direct collect light from the axis of objective lens to the horizontal axis, we added a mirror between the back aperture of the objective lens and the emission filter. Therefore, a broadband reflective mirror with a size of $2\,inch$ in diameter was mounted with a tilt angle at the top of the triangle frame(Fig. 4.1A). During the scanning, the whole triangle frame assembly is driven by the translation stage and moves back-and-forth along the surface of the tissue. The infinity-focused light coming from the scanning assembly is then focused by a large diameter camera lens and forms images on the sCMOS camera(Fig. 4.1B).

In theory, this design allows completely unrestricted 3D scanning of tissues with a large surface area. The scanning capacity merely depends on the range of the stage. Due to the unconventional vertical mounting of the translating stage, overloading may compromise its mechanical performance. In this design, we minimized the weight of the whole triangle assembly to $\sim 320\,g$ to ensure smooth travels with at least $0.1\,\mu m$ precision at a speed up to $2\,mm/second$.

Without restriction on the mechanical scanning volume, for functional imaging, the imaging capacity completely depends on the camera speed. With an up-to-date fast sCMOS camera (pco.edge 4.2) that allows $100\,Hz$ imaging with a whole frame size of

2160 pixels×2560 pixels, we managed to increase the calcium imaging volume by 15 fold compared to the first generation OCPI.

By imaging subdiffraction fluorescent beads (with a diameter of $0.2\,\mu$m), we measured the light sheet thickness throughout the field of view ($700\,\mu m \times 832\,\mu m$). At the beam waist, light sheet thickness is $\sim 5\,\mu$m (Fig. 4.2A), which was positioned at the center of the field of view. At the two edges of the field of view, the thickness increased to $\sim 10\,\mu$m (Fig. 4.2B). Thus, while the xy resolution is $0.325\,\mu$m, the z resolution is between $5-10\mu m$ in the whole two-dimensional field of view. The maximum scanning volume of hsOCPI is a three-dimensional stripe with the size of $350\,\mu$m×$832\,\mu$m×19 mm.

Because a Gaussian beam is used as the light source, the light intensity along the beam waist exhibits Gaussian distribution. The light intensity dropped by 30% on the two side edge in the filed of view. We correct this intensity drop in any three-dimensional rendered image. In analysis of neuronal activity, this intensity drop to some extent affects the signal-to-noise ratio, but not the neuronal responses since we calculate the fluorescence change $\Delta F/F$ as the response strength.

Besides the highlighted feature on the scanning design for large field of view and high speed, we also implemented five other new features compared with the first generation OCPI:

- Compared to all the other previously reported light sheet microscopy designs, the configuration of hsOCPI is more suitable for *in vivo* imaging of mice. The illumination optics was assembled within a 12 mm long, 8mm outer diameter compact cylinder carrier, which left spacious room around the objective lens to position large samples like a head-fixed mouse.
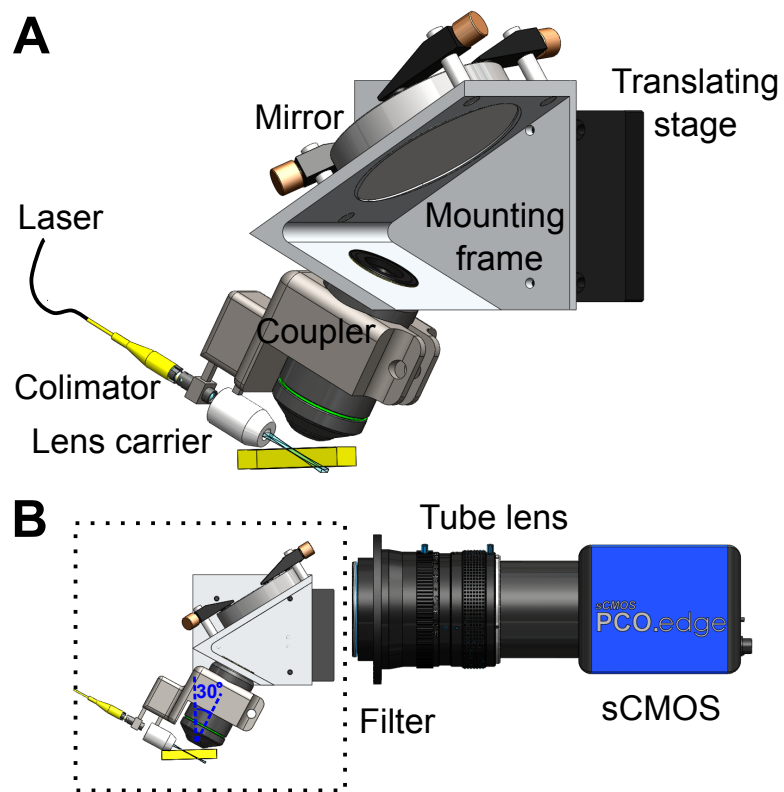
Figure 4.1. **Schematic of hsOCPI setup. A**, side view of the assembly of illumination and detection optics in three-dimensional perspective. **B**, front view of the whole optical design of hsOCPI.
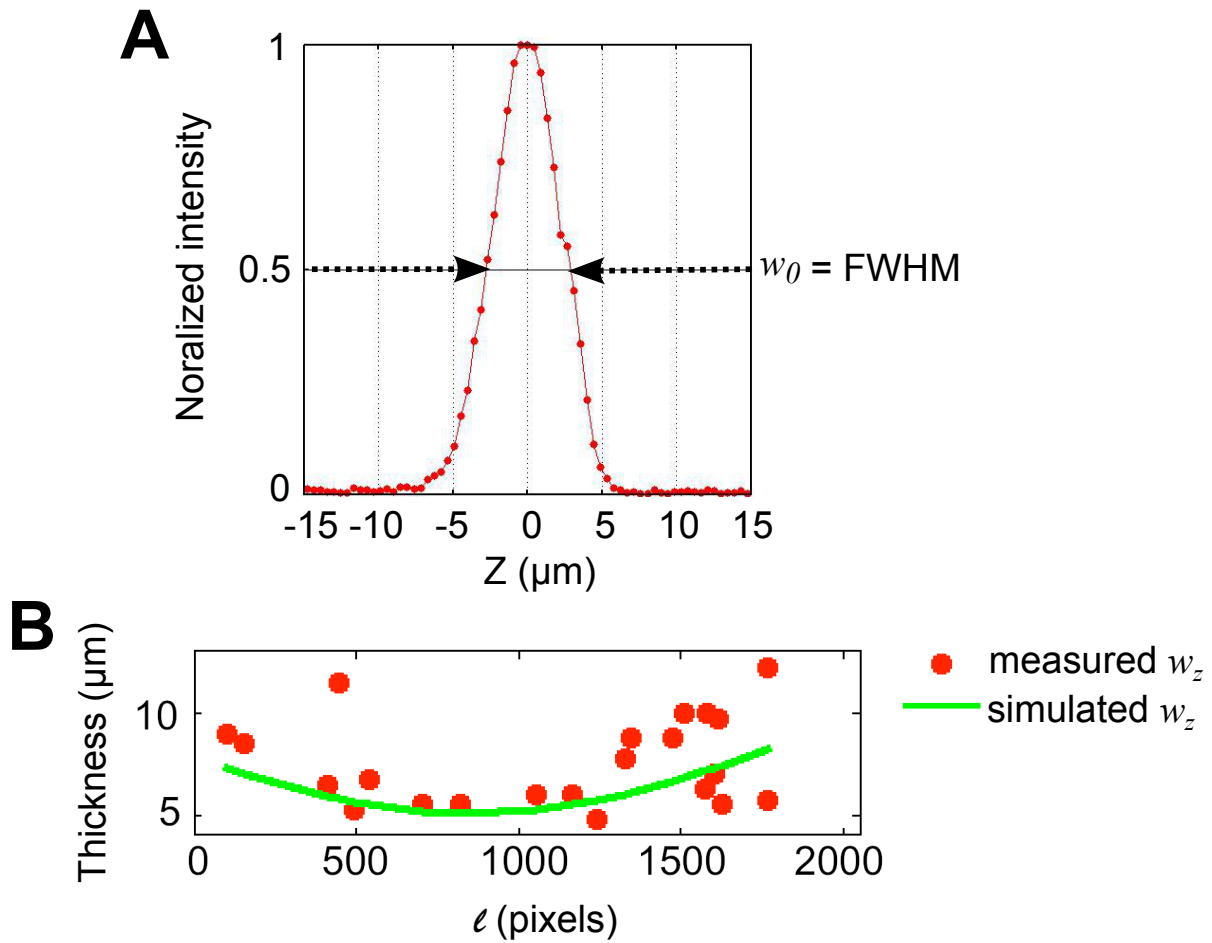
Figure 4.2. **Light sheet thickness. A**, thickness at the beam waist w_0. The intensity profile of a $0.2\,\mu$m fluorescent bead is plotted along the Z axis. FWHM: full-width at half maximum. **B**, the distribution of light sheet thickness along the light propagating axis ℓ in the whole filed of view.

- The miniaturized illumination arm allows unsymmetrical tilt of the illumination/objective coupler. We then changed the tilt angle of the objective lens from 45 degree to 30 degree to the vertical Z axis [60], which helps reduce aberration induced by non-perpendicular incident to the tissue surface.

- We implemented a bi-directional scanning modality, and therefore we can imaging the tissue twice during a back-and-forth scanning. This further enhances the temporal resolution of such a large-scale imaging.

- In order to perform multi-color fluorescence imaging, we used an achromatic spherical lens back to back with a concave cylindrical lens to form the light sheet from collimated laser light from four different laser lines: $465\,\mathrm{nm}$ /$491\,\mathrm{nm}$ /$515\,\mathrm{nm}$ /$561\,\mathrm{nm}$. This allows imaging of almost all of the regularly used fluorescent probes CFP /GFP /YFP /RFPs.

- With the same $\sim 20\times$ magnification, the higher pixel density of sCMOS camera result in better lateral resolution in hsOCPI. The lateral resolution enhanced from $0.71\,\mu$m in OCPI to 0.325μm in hsOCPI, thereby generating better lateral resolved images. This improvement will benefit the imaging of sub-cellular structures, such as dendrites and axons in the neural tissues, despite the fact that axial resolution still leaves behind the light sheet thickness. Additionally, a telephoto zoom lens (AF Nikkor, 180mm, f/2.8D) in the system provides variable magnification.

- In order to handle ~ 700megabyte per second high rate of data transfer and storage over hour-long recording, we upgraded the self-developed data acquisition software

Imagine [42] by implementing a spooling algorithm to write data directly the hard drive.

4.1.2   Large-scale volumetric imaging

Because hsOCPI has 19mm long travel range along the tissue surface, we first used it to image the entire nervous system of a laval zebrafish including the ~ 5mm long spinal cord (Fig. 4.3A). While the large-scale scanning covers the entire fish, the superior spatial resolution also allows discerning single cells as well as the peripheral nerves (Fig. 4.3B).

To perform the mouse cortical imaging, we started with a brain with sparse GFP labeling of interneurons (Fig. 4.4). With hsOCPI, we successfully scanned a $800\mu\,\mathrm{m}\times5.6\,\mathrm{mm}$ rectangular area across the two hemispheres of parietal cortex. Here the limits of the scanning distance came from the curvature of the brain. Regarding the penetration depth, we were able recognize sparsely labeled interneurons at depth of $\sim 200\,\mu$m. Neurons beyond that depth were no longer discernible due to the scattering of brain tissue.

4.2   Future plans

With miniaturized optics and a novel horizontal scanning design, we have achieved an unprecedentedly large-scale scanning of biological tissues with extensive surface area. The initial success of an *ex vivo* cortical imaging of the mouse brain encourages us move to the next step to imaging neural activity from head-fixed mice. Specifically, mice with GCaMP6 labeled cortical neurons will be used to perform calcium imaging with hsOCPI. Aiming for large population imaging, we will use the GCaMP6 viral vector and Emx-1 cre line to obtain a dense labeling of $\sim 80\%$ of cortical neurons [171]. As the
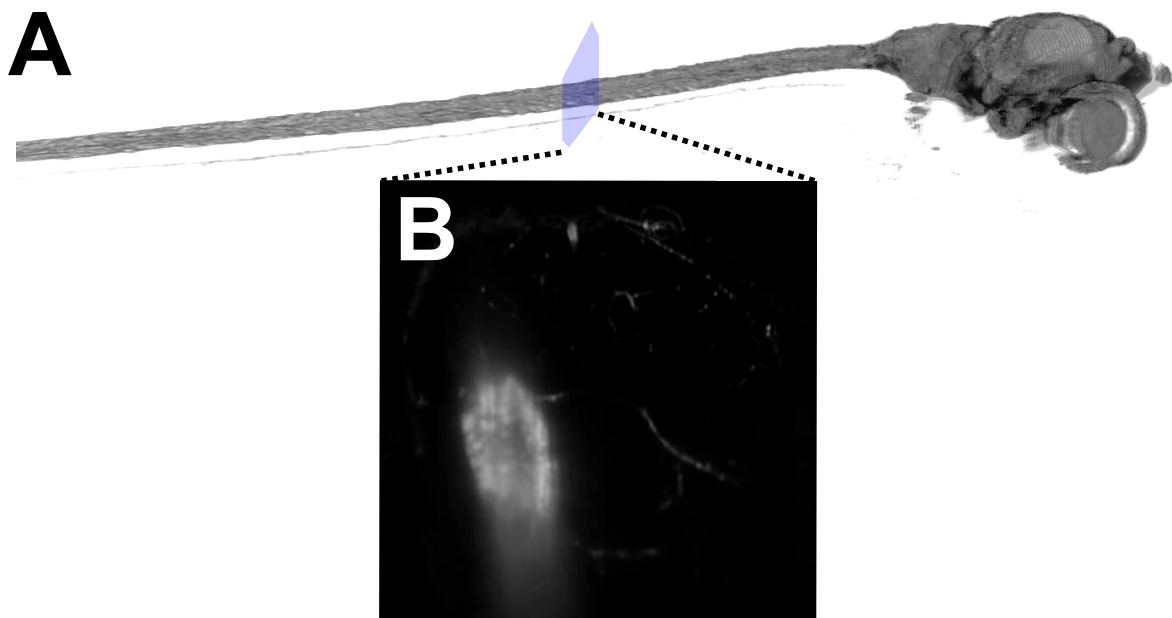
Figure 4.3. **Scanning the entire nervous system in the laval zebrafish.** 6-day-old laval of HuC:GFP transgenic line. **A**, three-dimensional rendering of the whole fish. **B**, an insection image showing the cross section of the spinal cord. Note the cell bodies in the spinal cord as well as the peripheral nerves around it.
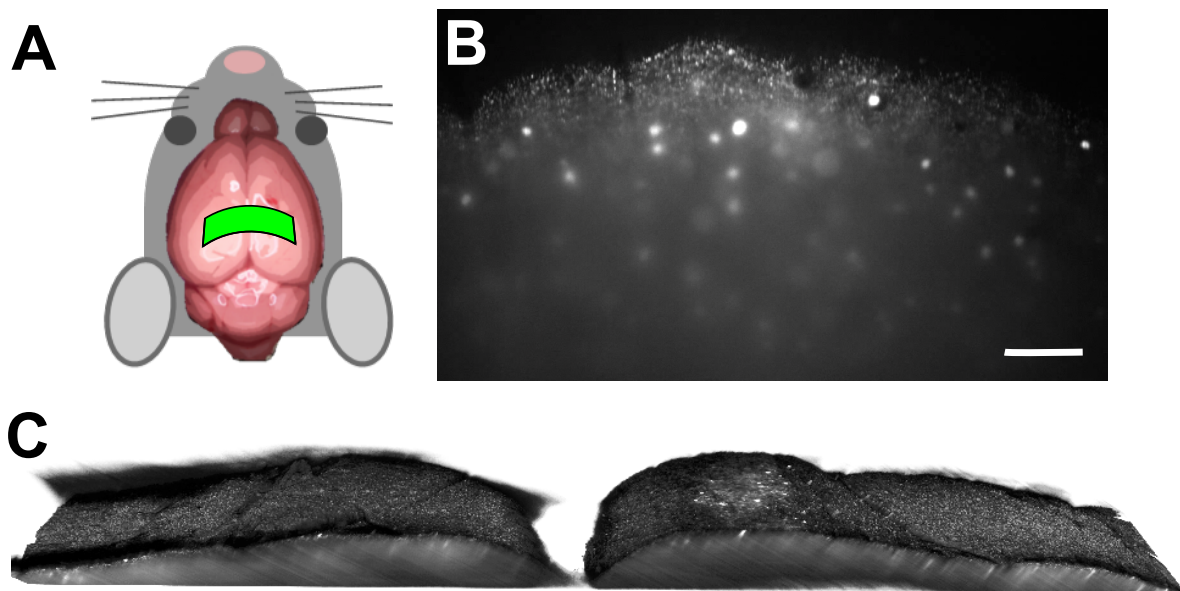
Figure 4.4. **Scanning a $\sim 6\,\text{mm}$ long stripe of mouse cortex. A**, a schematic shows a highlighted regions (in green) across the two hemispheres of cortex in an *ex vivo* whole mouse brain preparation. This long stripe coverages a $800\,\mu\text{m} \times 5.6\,\text{mm}$ surface area in the parietal cortex with GAD65-expressing interneurons labeled by GFP. **B**, an example two-dimensional frame shows sparely labeled interneurons in the layer2/3 cortex. Note the dendrites of these interneurons in layer 1. **C**, a three-dimensional rendering of a stack consists of 5600 frames exemplified in B. It clearly visualizes the brain landscape, including the blood vessels shown as the dark lines on the surface.

first demonstration of this imaging technique, we will start by monitoring spontaneous neuronal activity in the mouse visual cortex in anesthetized animals. It will establish an experimental platform as well as data analysis pipeline for future application in head-fixed behaving mice.

REFERENCES

[1] J G White, E Southgate, J N Thomson, and S Brenner. The structure of the nervous system of the nematode caenorhabditis elegans. *Philos Trans R Soc Lond B Biol Sci*, 314(1165):1–340, Nov 1986.

[2] Lav R Varshney, Beth L Chen, Eric Paniagua, David H Hall, and Dmitri B Chklovskii. Structural properties of the caenorhabditis elegans neuronal network. *PLoS Comput Biol*, 7(2):e1001066, 2011.

[3] Ju Lu, Juan Carlos Tapia, Olivia L White, and Jeff W Lichtman. The interscutularis muscle connectome. *PLoS Biol*, 7(2):e32, Feb 2009.

[4] Moritz Helmstaedter, Kevin L Briggman, Srinivas C Turaga, Viren Jain, H Sebastian Seung, and Winfried Denk. Connectomic reconstruction of the inner plexiform layer in the mouse retina. *Nature*, 500(7461):168–74, Aug 2013.

[5] A L HODGKIN and A F HUXLEY. A quantitative description of membrane current and its application to conduction and excitation in nerve. *J Physiol*, 117(4):500–44, Aug 1952.

[6] L. Galvani. De viribus electricitatis in motu musculari, commentarius. *Bonon. Sci. Art. Inst. Acad.*, 7(364):415, 1791///.

[7] Amiram Grinvald and Rina Hildesheim. Vsdi: a new era in functional imaging of cortical dynamics. *Nat Rev Neurosci*, 5(11):874–85, Nov 2004.

[8] Xiaolong Jiang, Guangfu Wang, Alice J Lee, Ruth L Stornetta, and J Julius Zhu. The organization of two new cortical interneuronal circuits. *Nat Neurosci*, 16(2):210–8, Feb 2013.

[9] Antal Berényi, Zoltán Somogyvári, Anett J Nagy, Lisa Roux, John D Long, Shigeyoshi Fujisawa, Eran Stark, Anthony Leonardo, Timothy D Harris, and György Buzsáki. Large-scale, high-density (up to 512 channels) recording of local circuits in behaving animals. *J Neurophysiol*, 111(5):1132–49, Mar 2014.

[10] Brian A Wilt, Laurie D Burns, Eric Tatt Wei Ho, Kunal K Ghosh, Eran A Mukamel, and Mark J Schnitzer. Advances in light microscopy for neuroscience. *Annu Rev Neurosci*, 32:435–506, 2009.

[11] Misha B Ahrens, Michael B Orger, Drew N Robson, Jennifer M Li, and Philipp J Keller. Whole-brain functional imaging at cellular resolution using light-sheet microscopy. *Nat Methods*, 10(5):413–20, May 2013.

[12] Tina Schrödel, Robert Prevedel, Karin Aumayr, Manuel Zimmer, and Alipasha Vaziri. Brain-wide 3d imaging of neuronal activity in caenorhabditis elegans with sculpted light. *Nat Methods*, 10(10):1013–20, Oct 2013.

[13] Thomas Panier, Sebastián A Romano, Raphaël Olive, Thomas Pietri, Germán Sumbre, Raphaël Candelier, and Georges Debrégeas. Fast functional imaging of multiple brain regions in intact zebrafish larvae using selective plane illumination microscopy. *Front Neural Circuits*, 7:65, 2013.

[14] B M Salzberg, H V Davila, and L B Cohen. Optical recording of impulses in individual neurones of an invertebrate central nervous system. *Nature*, 246(5434):508–9, 1973.

[15] R Y Tsien. New calcium indicators and buffers with high selectivity against magnesium and protons: design, synthesis, and properties of prototype structures. *Biochemistry*, 19(11):2396–404, May 1980.

[16] Ryohei Yasuda, Esther A Nimchinsky, Volker Scheuss, Thomas A Pologruto, Thomas G Oertner, Bernardo L Sabatini, and Karel Svoboda. Imaging calcium concentration dynamics in small neuronal compartments. *Sci STKE*, 2004(219):pl5, Feb 2004.

[17] Takuya Sasaki, Naoya Takahashi, Norio Matsuki, and Yuji Ikegaya. Fast and accurate detection of action potentials from somatic calcium fluctuations. *J Neurophysiol*, 100(3):1668–76, Sep 2008.

[18] S Andrew Hires, Lin Tian, and Loren L Looger. Reporting neural activity with genetically encoded calcium indicators. *Brain Cell Biol*, 36(1-4):69–86, Aug 2008.

[19] Lin Tian, S Andrew Hires, and Loren L Looger. Imaging neuronal activity with genetically encoded calcium indicators. *Cold Spring Harb Protoc*, 2012(6):647–56, Jun 2012.

[20] Christoph Stosiek, Olga Garaschuk, Knut Holthoff, and Arthur Konnerth. In vivo two-photon calcium imaging of neuronal networks. *Proc Natl Acad Sci U S A*, 100(12):7319–24, Jun 2003.

[21] Kevin L Briggman and Thomas Euler. Bulk electroporation and population calcium imaging in the adult mammalian retina. *J Neurophysiol*, 105(5):2601–9, May 2011.

[22] Joshua L Morgan and Rachel O L Wong. Ballistic labeling with fluorescent dyes and indicators. *Curr Protoc Neurosci*, Chapter 2:Unit 2.11, Apr 2008.

[23] Hatim A Zariwala, Bart G Borghuis, Tycho M Hoogland, Linda Madisen, Lin Tian, Chris I De Zeeuw, Hongkui Zeng, Loren L Looger, Karel Svoboda, and Tsai-Wen Chen. A cre-dependent gcamp3 reporter mouse for neuronal imaging in vivo. *J Neurosci*, 32(9):3131–41, Feb 2012.

[24] Oded Tour, Stephen R Adams, Rex A Kerr, Rene M Meijer, Terrence J Sejnowski, Richard W Tsien, and Roger Y Tsien. Calcium green flash as a genetically targeted small-molecule calcium indicator. *Nat Chem Biol*, 3(7):423–31, Jul 2007.

[25] Lin Tian, Yunlei Yang, Laura M Wysocki, Alma C Arnold, Amy Hu, Balaji Ravichandran, Scott M Sternson, Loren L Looger, and Luke D Lavis. Selective esterase-ester pair for targeting small molecules with cellular specificity. *Proc Natl Acad Sci U S A*, 109(13):4756–61, Mar 2012.

[26] Joel M Kralj, Adam D Douglass, Daniel R Hochbaum, Dougal Maclaurin, and Adam E Cohen. Optical recording of action potentials in mammalian neurons using a microbial rhodopsin. *Nat Methods*, 9(1):90–5, Jan 2012.

[27] Lin Tian, S Andrew Hires, Tianyi Mao, Daniel Huber, M Eugenia Chiappe, Sreekanth H Chalasani, Leopoldo Petreanu, Jasper Akerboom, Sean A McKinney,

Eric R Schreiter, Cornelia I Bargmann, Vivek Jayaraman, Karel Svoboda, and Loren L Looger. Imaging neural activity in worms, flies and mice with improved gcamp calcium indicators. *Nat Methods*, 6(12):875–81, Dec 2009.

[28] Tsai-Wen Chen, Trevor J Wardill, Yi Sun, Stefan R Pulver, Sabine L Renninger, Amy Baohan, Eric R Schreiter, Rex A Kerr, Michael B Orger, Vivek Jayaraman, Loren L Looger, Karel Svoboda, and Douglas S Kim. Ultrasensitive fluorescent proteins for imaging neuronal activity. *Nature*, 499(7458):295–300, Jul 2013.

[29] Lei Jin, Zhou Han, Jelena Platisa, Julian R A Wooltorton, Lawrence B Cohen, and Vincent A Pieribone. Single action potentials and subthreshold electrical events imaged in neurons with a fluorescent protein voltage probe. *Neuron*, 75(5):779–85, Sep 2012.

[30] Guan Cao, Jelena Platisa, Vincent A Pieribone, Davide Raccuglia, Michael Kunst, and Michael N Nitabach. Genetically targeted optical electrophysiology in intact neural circuits. *Cell*, 154(4):904–13, Aug 2013.

[31] Walther Akemann, Alicia Lundby, Hiroki Mutoh, and Thomas Knöpfel. Effect of voltage sensitive fluorescent proteins on neuronal excitability. *Biophys J*, 96(10):3959–76, May 2009.

[32] Walther Akemann, Hiroki Mutoh, Amélie Perron, Jean Rossier, and Thomas Knöpfel. Imaging brain electric signals with genetically targeted voltage-sensitive fluorescent proteins. *Nat Methods*, 7(8):643–9, Aug 2010.

[33] Thomas Knöpfel. Genetically encoded optical indicators for the analysis of neuronal circuits. *Nat Rev Neurosci*, 13(10):687–700, Oct 2012.

[34] M A Neil, R Juskaitis, and T Wilson. Method of obtaining optical sectioning by using structured light in a conventional microscope. *Opt Lett*, 22(24):1905–7, Dec 1997.

[35] Mats G L Gustafsson, Lin Shao, Peter M Carlton, C J Rachel Wang, Inna N Golubovskaya, W Zacheus Cande, David A Agard, and John W Sedat. Three-dimensional resolution doubling in wide-field fluorescence microscopy by structured illumination. *Biophys J*, 94(12):4957–70, Jun 2008.

[36] Robert Prevedel, Young-Gyu Yoon, Maximilian Hoffmann, Nikita Pak, Gordon Wetzstein, Saul Kato, Tina Schrödel, Ramesh Raskar, Manuel Zimmer, Edward S Boyden, and Alipasha Vaziri. Simultaneous whole-animal 3d imaging of neuronal activity using light-field microscopy. *Nat Methods*, May 2014.

[37] Vasilis Ntziachristos. Going deeper than microscopy: the optical imaging frontier in biology. *Nat Methods*, 7(8):603–14, Aug 2010.

[38] Wolfgang Mittmann, Damian J Wallace, Uwe Czubayko, Jan T Herb, Andreas T Schaefer, Loren L Looger, Winfried Denk, and Jason N D Kerr. Two-photon calcium imaging of evoked activity from l5 somatosensory neurons in vivo. *Nat Neurosci*, 14(8):1089–93, Aug 2011.

[39] Henry Lütcke and Fritjof Helmchen. Two-photon imaging and analysis of neural network dynamics. *Reports on Progress in Physics*, 74(8):086602, 2011.

[40] Werner Göbel, Björn M Kampa, and Fritjof Helmchen. Imaging cellular network dynamics in three dimensions using fast 3d laser scanning. *Nat Methods*, 4(1):73–9, Jan 2007.

[41] Adrian Cheng, J Tiago Gonçalves, Peyman Golshani, Katsushi Arisaka, and Carlos Portera-Cailliau. Simultaneous two-photon calcium imaging at different depths with spatiotemporal multiplexing. *Nat Methods*, 8(2):139–42, Feb 2011.

[42] Terrence F Holekamp, Diwakar Turaga, and Timothy E Holy. Fast three-dimensional fluorescence imaging of activity in neural populations by objective-coupled planar illumination microscopy. *Neuron*, 57(5):661–72, Mar 2008.

[43] James Pawley. *Handbook of biological confocal microscopy*. Springer, 2010.

[44] J Bewersdorf, R Pick, and S W Hell. Multifocal multiphoton microscopy. *Opt Lett*, 23(9):655–7, 1998.

[45] Volodymyr Nikolenko, Brendon O Watson, Roberto Araya, Alan Woodruff, Darcy S Peterka, and Rafael Yuste. Slm microscopy: Scanless two-photon imaging and photostimulation with spatial light modulators. *Front Neural Circuits*, 2:5, 2008.

[46] Benjamin F Grewe, Dominik Langer, Hansjörg Kasper, Björn M Kampa, and Fritjof Helmchen. High-speed in vivo calcium imaging reveals neuronal network activity with near-millisecond precision. *Nat Methods*, 7(5):399–405, May 2010.

[47] José-Angel Conchello and Jeff W Lichtman. Optical sectioning microscopy. *Nat Methods*, 2(12):920–31, Dec 2005.

[48] Takeo Tanaami, Shinya Otsuki, Nobuhiro Tomosada, Yasuhito Kosugi, Mizuho Shimizu, and Hideyuki Ishida. High-speed 1-frame/ms scanning confocal microscope with a microlens and nipkow disks. *Appl Opt*, 41(22):4704–8, Aug 2002.

[49] H. Siedentopf and R. Zsigmondy. Uber sichtbarmachung und größenbestimmung ultramikoskopischer teilchen, mit besonderer anwendung auf goldrubingläser. *Annalen der Physik*, 315(1):1–39, 1902.

[50] A H Voie, D H Burns, and F A Spelman. Orthogonal-plane fluorescence optical sectioning: three-dimensional imaging of macroscopic biological specimens. *J Microsc*, 170(Pt 3):229–36, Jun 1993.

[51] Makio Tokunaga, Naoko Imamoto, and Kumiko Sakata-Sogawa. Highly inclined thin illumination enables clear single-molecule imaging in cells. *Nat Methods*, 5(2):159–61, Feb 2008.

[52] C Dunsby. Optically sectioned imaging by oblique plane microscopy. *Opt Express*, 16(25):20306–16, Dec 2008.

[53] R. Wolleschensky. Arrangement for microscopic observation and/or detection in a light scanning microscope with line scanning and use, February 7 2008. US Patent App. 11/812,991.

[54] Diwakar Turaga and Timothy E Holy. Miniaturization and defocus correction for objective-coupled planar illumination microscopy. *Opt Lett*, 33(20):2302–4, Oct 2008.

[55] Christoph J Engelbrecht, Fabian Voigt, and Fritjof Helmchen. Miniaturized selective plane illumination microscopy for high-contrast in vivo fluorescence imaging. *Opt Lett*, 35(9):1413–5, May 2010.

[56] J Durnin, J J Miceli, Jr, and J H Eberly. Comparison of bessel and gaussian beams. *Opt Lett*, 13(2):79, Feb 1988.

[57] Thomas A Planchon, Liang Gao, Daniel E Milkie, Michael W Davidson, James A Galbraith, Catherine G Galbraith, and Eric Betzig. Rapid three-dimensional isotropic imaging of living cells using bessel beam plane illumination. *Nat Methods*, 8(5):417–23, May 2011.

[58] Jonas Binding, Juliette Ben Arous, Jean-François Léger, Sylvain Gigan, Claude Boccara, and Laurent Bourdieu. Brain refractive index measured in vivo with high-na defocus-corrected full-field oct and consequences for two-photon microscopy. *Optics express*, 19(6):4833–4847, 2011.

[59] Jingjing Sun, Sung Jin Lee, Lei Wu, Malisa Sarntinoranont, and Huikai Xie. Refractive index measurement of acute rat brain tissue slices using optical coherence tomography. *Optics express*, 20(2):1084–1095, 2012.

[60] Diwakar Turaga and Timothy E Holy. Aberrations and their correction in light-sheet microscopy: a low-dimensional parametrization. *Biomed Opt Express*, 4(9):1654–61, 2013.

[61] Thai V Truong, Willy Supatto, David S Koos, John M Choi, and Scott E Fraser. Deep and fast live imaging with two-photon scanned light-sheet microscopy. *Nat Methods*, 8(9):757–60, Sep 2011.

[62] Eran A Mukamel, Axel Nimmerjahn, and Mark J Schnitzer. Automated analysis of cellular signals from large-scale calcium imaging data. *Neuron*, 63(6):747–60, Sep 2009.

[63] Daniel A Dombeck, Christopher D Harvey, Lin Tian, Loren L Looger, and David W Tank. Functional imaging of hippocampal place cells at cellular resolution during virtual navigation. *Nat Neurosci*, 13(11):1433–40, Nov 2010.

[64] Elizabeth Pennisi. Breakthrough of the year. human genetic variation. *Science*, 318(5858):1842–3, Dec 2007.

[65] Greg Miller. Mysteries of the brain. why are you and your brain unique? *Science*, 338(6103):35–6, Oct 2012.

[66] D Samuel Schwarzkopf, Chen Song, and Geraint Rees. The surface area of human v1 predicts the subjective experience of object size. *Nat Neurosci*, 14(1):28–30, Jan 2011.

[67] Ryota Kanai and Geraint Rees. The structural basis of inter-individual differences in human behaviour and cognition. *Nat Rev Neurosci*, 12(4):231–42, Apr 2011.

[68] Raja Parasuraman and Yang Jiang. Individual differences in cognition, affect, and performance: behavioral, neuroimaging, and molecular genetic approaches. *Neuroimage*, 59(1):70–82, Jan 2012.

[69] Sophia Mueller, Danhong Wang, Michael D Fox, B T Thomas Yeo, Jorge Sepulcre, Mert R Sabuncu, Rebecca Shafee, Jie Lu, and Hesheng Liu. Individual variability in functional connectivity architecture of the human brain. *Neuron*, 77(3):586–95, Feb 2013.

[70] Ya-Hui Chou, Maria L Spletter, Emre Yaksi, Jonathan C S Leong, Rachel I Wilson, and Liqun Luo. Diversity and wiring variability of olfactory local interneurons in the drosophila antennal lobe. *Nat Neurosci*, 13(4):439–49, Apr 2010.

[71] Diwakar Turaga and Timothy E Holy. Organization of vomeronasal sensory coding revealed by fast volumetric calcium imaging. *J Neurosci*, 32(5):1612–21, Feb 2012.

[72] Gary F Hammen, Diwakar Turaga, Timothy E Holy, and Julian P Meeks. Functional organization of glomerular maps in the mouse accessory olfactory bulb. *Nat Neurosci*, Jun 2014.

[73] J B Powers and S S Winans. Vomeronasal organ: critical role in mediating sexual behavior of the male hamster. *Science*, 187(4180):961–3, Mar 1975.

[74] A N Clancy, A Coquelin, F Macrides, R A Gorski, and E P Noble. Sexual behavior and aggression in male mice: involvement of the vomeronasal system. *J Neurosci*, 4(9):2222–9, Sep 1984.

[75] Lisa Stowers, Timothy E Holy, Markus Meister, Catherine Dulac, and Georgy Koentges. Loss of sex discrimination and male-male aggression in mice deficient for trp2. *Science*, 295(5559):1493–500, Feb 2002.

[76] Bradley G Leypold, C Ron Yu, Trese Leinders-Zufall, Michelle M Kim, Frank Zufall, and Richard Axel. Altered sexual and social behaviors in trp2 mutant mice. *Proc Natl Acad Sci U S A*, 99(9):6376–81, Apr 2002.

[77] Tali Kimchi, Jennings Xu, and Catherine Dulac. A functional circuit underlying male sexual behaviour in the female mouse brain. *Nature*, 448(7157):1009–14, Aug 2007.

[78] Karina Del Punta, Trese Leinders-Zufall, Ivan Rodriguez, David Jukam, Charles J Wysocki, Sonoko Ogawa, Frank Zufall, and Peter Mombaerts. Deficient pheromone responses in mice lacking a cluster of vomeronasal receptor genes. *Nature*, 419(6902):70–4, Sep 2002.

[79] Matthieu Keller, Sylvie Pierman, Quentin Douhard, Michael J Baum, and Julie Bakker. The vomeronasal organ is required for the expression of lordosis behaviour, but not sex discrimination in female mice. *Eur J Neurosci*, 23(2):521–30, Jan 2006.

[80] E Marianne Norlin, Fredrik Gussing, and Anna Berghard. Vomeronasal phenotype and behavioral alterations in g alpha i2 mutant mice. *Curr Biol*, 13(14):1214–9, Jul 2003.

[81] Sachiko Haga, Tatsuya Hattori, Toru Sato, Koji Sato, Soichiro Matsuda, Reiko Kobayakawa, Hitoshi Sakano, Yoshihiro Yoshihara, Takefumi Kikusui, and Kazushige Touhara. The male mouse pheromone esp1 enhances female sexual receptive behaviour through a specific vomeronasal receptor. *Nature*, 466(7302):118–22, Jul 2010.

[82] David M Ferrero, Lisa M Moeller, Takuya Osakada, Nao Horio, Qian Li, Dheeraj S Roy, Annika Cichy, Marc Spehr, Kazushige Touhara, and Stephen D Liberles. A juvenile mouse pheromone inhibits sexual behaviour through the vomeronasal system. *Nature*, Oct 2013.

[83] J A Maruniak, C J Wysocki, and J A Taylor. Mediation of male mouse urine marking and aggression by the vomeronasal organ. *Physiol Behav*, 37(4):655–7, 1986.

[84] C J Wysocki and J J Lepri. Consequences of removing the vomeronasal organ. *J Steroid Biochem Mol Biol*, 39(4B):661–9, Oct 1991.

[85] Pablo Chamero, Tobias F Marton, Darren W Logan, Kelly Flanagan, Jason R Cruz, Alan Saghatelian, Benjamin F Cravatt, and Lisa Stowers. Identification of protein pheromones that promote aggressive behaviour. *Nature*, 450(7171):899–902, Dec 2007.

[86] Kashiko S Tachikawa, Yoshihiro Yoshihara, and Kumi O Kuroda. Behavioral transition from attack to parenting in male mice: a crucial role of the vomeronasal system. *J Neurosci*, 33(12):5120–6, Mar 2013.

[87] Fabio Papes, Darren W Logan, and Lisa Stowers. The vomeronasal organ mediates interspecies defensive behaviors through detection of protein pheromone homologs. *Cell*, 141(4):692–703, May 2010.

[88] N J Bean and C J Wysocki. Vomeronasal organ removal and female mouse aggression: the role of experience. *Physiol Behav*, 45(5):875–82, May 1989.

[89] Stéphane Rivière, Ludivine Challet, Daniela Fluegge, Marc Spehr, and Ivan Rodriguez. Formyl peptide receptor-like proteins are a novel family of vomeronasal chemosensors. *Nature*, 459(7246):574–7, May 2009.

[90] Stephen D Liberles, Lisa F Horowitz, Donghui Kuang, James J Contos, Kathleen L Wilson, Jessica Siltberg-Liberles, David A Liberles, and Linda B Buck. Formyl peptide receptors are candidate chemosensory receptors in the vomeronasal organ. *Proc Natl Acad Sci U S A*, 106(24):9842–7, Jun 2009.

[91] Kazushige Touhara and Leslie B Vosshall. Sensing odorants and pheromones with chemosensory receptors. *Annu Rev Physiol*, 71:307–32, 2009.

[92] Roberto Tirindelli, Michele Dibattista, Simone Pifferi, and Anna Menini. From pheromones to behavior. *Physiol Rev*, 89(3):921–56, Jul 2009.

[93] C Dulac and R Axel. A novel family of genes encoding putative pheromone receptors in mammals. *Cell*, 83(2):195–206, Oct 1995.

[94] H Matsunami and L B Buck. A multigene family encoding a diverse array of putative pheromone receptors in mammals. *Cell*, 90(4):775–84, Aug 1997.

[95] G Herrada and C Dulac. A novel family of putative pheromone receptors in mammals with a topographically organized and sexually dimorphic distribution. *Cell*, 90(4):763–73, Aug 1997.

[96] E Pantages and C Dulac. A novel family of candidate pheromone receptors in mammals. *Neuron*, 28(3):835–45, Dec 2000.

[97] Francesco Nodari, Fong-Fu Hsu, Xiaoyan Fu, Terrence F Holekamp, Lung-Fa Kao, John Turk, and Timothy E Holy. Sulfated steroids as natural ligands of mouse pheromone-sensing neurons. *J Neurosci*, 28(25):6407–18, Jun 2008.

[98] S Firestein. How the olfactory system makes sense of scents. *Nature*, 413(6852):211–8, Sep 2001.

[99] Alexander Gimelbrant, John N Hutchinson, Benjamin R Thompson, and Andrew Chess. Widespread monoallelic expression on human autosomes. *Science*, 318(5853):1136–40, Nov 2007.

[100] Takeshi Yagi. Genetic basis of neuronal individuality in the mammalian brain. *J Neurogenet*, 27(3):97–105, Sep 2013.

[101] J K Young. A comparison of hypothalami of rats and mice: lack of gross sexual dimorphism in the mouse. *Brain Res*, 239(1):233–9, May 1982.

[102] B Cooke, C D Hegstrom, L S Villeneuve, and S M Breedlove. Sexual differentiation of the vertebrate brain: principles and mechanisms. *Front Neuroendocrinol*, 19(4):323–62, Oct 1998.

[103] Richard B Simerly. Wired for reproduction: organization and development of sexually dimorphic circuits in the mammalian forebrain. *Annu Rev Neurosci*, 25:507–36, 2002.

[104] John A Morris, Cynthia L Jordan, and S Marc Breedlove. Sexual differentiation of the vertebrate nervous system. *Nat Neurosci*, 7(10):1034–9, Oct 2004.

[105] Nirao M Shah, David J Pisapia, Silas Maniatis, Monica M Mendelsohn, Adriana Nemes, and Richard Axel. Visualizing sexual dimorphism in the brain. *Neuron*, 43(3):313–9, Aug 2004.

[106] Cory A Wolfe, Margaret Van Doren, Heather J Walker, Marianne L Seney, Kristy M McClellan, and Stuart A Tobet. Sex differences in the location of immunochemically defined cell populations in the mouse preoptic area/anterior hypothalamus. *Brain Res Dev Brain Res*, 157(1):34–41, Jun 2005.

[107] Melody V Wu, Devanand S Manoli, Eleanor J Fraser, Jennifer K Coats, Jessica Tollkuhn, Shin-Ichiro Honda, Nobuhiro Harada, and Nirao M Shah. Estrogen masculinizes neural pathways and sex-specific behaviors. *Cell*, 139(1):61–72, Oct 2009.

[108] Xiaohong Xu, Jennifer K Coats, Cindy F Yang, Amy Wang, Osama M Ahmed, Maricruz Alvarado, Tetsuro Izumi, and Nirao M Shah. Modular genetic control of sexually dimorphic behaviors. *Cell*, 148(3):596–607, Feb 2012.

[109] Cindy F Yang, Michael C Chiang, Daniel C Gray, Mahalakshmi Prabhakaran, Maricruz Alvarado, Scott A Juntti, Elizabeth K Unger, James A Wells, and Nirao M Shah. Sexually dimorphic neurons in the ventromedial hypothalamus govern mating in both sexes and aggression in males. *Cell*, 153(4):896–909, May 2013.

[110] Mimi Halpern and Alino Martínez-Marcos. Structure and function of the vomeronasal system: an update. *Prog Neurobiol*, 70(3):245–318, Jun 2003.

[111] Catherine Dulac and Tali Kimchi. Neural mechanisms underlying sex-specific behaviors in vertebrates. *Curr Opin Neurobiol*, 17(6):675–83, Dec 2007.

[112] S Segovia and A Guillamón. Effects of sex steroids on the development of the vomeronasal organ in the rat. *Brain Res*, 281(2):209–12, Oct 1982.

[113] E M Dawley and J Crowder. Sexual and seasonal differences in the vomeronasal epithelium of the red-backed salamander (plethodon cinereus). *J Comp Neurol*, 359(3):382–90, Aug 1995.

[114] Xiaohong Zhang, Florencia Marcucci, and Stuart Firestein. High-throughput microarray detection of vomeronasal receptor gene expression in rodents. *Front Neurosci*, 4:164, 2010.

[115] H A Halem, J A Cherry, and M J Baum. Vomeronasal neuroepithelium and forebrain fos responses to male pheromones in male and female mice. *J Neurobiol*, 39(2):249–63, May 1999.

[116] H A Halem, M J Baum, and J A Cherry. Sex difference and steroid modulation of pheromone-induced immediate early genes in the two zones of the mouse accessory olfactory system. *J Neurosci*, 21(7):2474–80, Apr 2001.

[117] S K Woodley, A L Cloe, P Waters, and M J Baum. Effects of vomeronasal organ removal on olfactory sex discrimination and odor preferences of female ferrets. *Chem Senses*, 29(8):659–69, Oct 2004.

[118] Avshalom Caspi, Karen Sugden, Terrie E Moffitt, Alan Taylor, Ian W Craig, HonaLee Harrington, Joseph McClay, Jonathan Mill, Judy Martin, Antony Braithwaite, and Richie Poulton. Influence of life stress on depression: moderation by a polymorphism in the 5-htt gene. *Science*, 301(5631):386–9, Jul 2003.

[119] Wun Chey Sin, Kurt Haas, Edward S Ruthazer, and Hollis T Cline. Dendrite growth increased by visual activity requires nmda receptor and rho gtpases. *Nature*, 419(6906):475–80, Oct 2002.

[120] Steven W Flavell and Michael E Greenberg. Signaling mechanisms linking neuronal activity to gene expression and plasticity of the nervous system. *Annu Rev Neurosci*, 31:563–90, 2008.

[121] Daniel E Feldman. Synaptic mechanisms for plasticity in neocortex. *Annu Rev Neurosci*, 32:33–55, 2009.

[122] H Zhao and R R Reed. X inactivation of the ocnc1 channel gene reveals a role for activity-dependent competition in the olfactory system. *Cell*, 104(5):651–60, Mar 2001.

[123] Stephen W Santoro and Catherine Dulac. The activity-dependent histone variant h2be modulates the life span of olfactory neurons. *Elife*, 1:e00070, 2012.

[124] Kevin D Broad and Eric B Keverne. The post-natal chemosensory environment induces epigenetic changes in vomeronasal receptor gene expression and a bias in olfactory preference. *Behav Genet*, 42(3):461–71, May 2012.

[125] Silke Hagendorf, Daniela Fluegge, Corinna Engelhardt, and Marc Spehr. Homeostatic control of sensory output in basal vomeronasal neurons: activity-dependent expression of ether-à-go-go-related gene potassium channels. *J Neurosci*, 29(1):206–21, Jan 2009.

[126] Michael Weber and Jan Huisken. Light sheet microscopy for real-time developmental biology. *Curr Opin Genet Dev*, 21(5):566–72, Oct 2011.

[127] Philipp J Keller, Annette D Schmidt, Joachim Wittbrodt, and Ernst H K Stelzer. Reconstruction of zebrafish early embryonic development by scanned light sheet microscopy. *Science*, 322(5904):1065–9, Nov 2008.

[128] Yicong Wu, Alireza Ghitani, Ryan Christensen, Anthony Santella, Zhuo Du, Gary Rondeau, Zhirong Bao, Daniel Colón-Ramos, and Hari Shroff. Inverted selective plane illumination microscopy (ispim) enables coupled cell identity lineaging and neurodevelopmental imaging in caenorhabditis elegans. *Proc Natl Acad Sci U S A*, 108(43):17708–13, Oct 2011.

[129] Jan Huisken, Jim Swoger, Filippo Del Bene, Joachim Wittbrodt, and Ernst H K Stelzer. Optical sectioning deep inside live embryos by selective plane illumination microscopy. *Science*, 305(5686):1007–9, Aug 2004.

[130] Jan Huisken and Didier Y R Stainier. Even fluorescence excitation by multidirectional selective plane illumination microscopy (mspim). *Opt Lett*, 32(17):2608–10, Sep 2007.

[131] Pei Sabrina Xu and Timothy E Holy. Whole-mount imaging of responses in mouse vomeronasal neurons. *Methods Mol Biol*, 1068:201–10, 2013.

[132] Julian P Meeks, Hannah A Arnson, and Timothy E Holy. Representation and transformation of sensory information in the mouse accessory olfactory system. *Nat Neurosci*, 13(6):723–30, Jun 2010.

[133] Jie He, Limei Ma, Sangseong Kim, Junichi Nakai, and C Ron Yu. Encoding gender and individual information in the mouse vomeronasal organ. *Science*, 320(5875):535–8, Apr 2008.

[134] Jinsong Li, Tomohiro Ishii, Paul Feinstein, and Peter Mombaerts. Odorant receptor gene choice is reset by nuclear transfer from mouse olfactory sensory neurons. *Nature*, 428(6981):393–9, Mar 2004.

[135] Hannah A Arnson, Xiaoyan Fu, and Timothy E Holy. Multielectrode array recordings of the vomeronasal epithelium. *J Vis Exp*, (37), 2010.

[136] Jeff Bezanson, Stefan Karpinski, Viral B. Shah, and Alan Edelman. Julia: A fast dynamic language for technical computing. *CoRR*, abs/1209.5145, 2012.

[137] Dorin Comaniciu and Peter Meer. Mean shift: A robust approach toward feature space analysis. *IEEE Trans. Pattern Anal. Mach. Intell.*, 24(5):603–619, 2002.

[138] P McCullagh and JA Nelder. *Generalized Linear Models. 1989 London.* Chapman and Hall, 1989.

[139] Timothy E Holy and Zhongsheng Guo. Ultrasonic songs of male mice. *PLoS Biol*, 3(12):e386, Dec 2005.

[140] Zhongsheng Guo and Timothy E Holy. Sex selectivity of mouse ultrasonic songs. *Chem Senses*, 32(5):463–73, Jun 2007.

[141] R Hedewig. [comparative anatomical studies on the organs of jacobson of nycticebus coucang boddaert, 1785 (prosimiae, lorisidae) and galago crassicandatus e. geoffroy, 1812 (prosimiae, lorisidae).ii.galago crassicaudatus]. *Gegenbaurs Morphol Jahrb*, 126(5):676–722, 1980.

[142] K C Wilson and G Raisman. Age-related changes in the neurosensory epithelium of the mouse vomeronasal organ: extended period of postnatal growth in size and evidence for rapid cell turnover in the adult. *Brain Res*, 185(1):103–13, Mar 1980.

[143] S M Breedlove. Sexual dimorphism in the vertebrate nervous system. *J Neurosci*, 12(11):4133–42, Nov 1992.

[144] Margaret M McCarthy and Arthur P Arnold. Reframing sexual differentiation of the brain. *Nat Neurosci*, 14(6):677–83, Jun 2011.

[145] O V Alekseyenko, M J Baum, and J A Cherry. Sex and gonadal steroid modulation of pheromone receptor gene expression in the mouse vomeronasal organ. *Neuroscience*, 140(4):1349–57, Jul 2006.

[146] Cristian Bodo. A role for the androgen receptor in the sexual differentiation of the olfactory system in mice. *Brain Res Rev*, 57(2):321–31, Mar 2008.

[147] Jessica D Gatewood, Aileen Wills, Savera Shetty, Jun Xu, Arthur P Arnold, Paul S Burgoyne, and Emilie F Rissman. Sex chromosome complement and gonadal sex influence aggressive and parental behaviors in mice. *J Neurosci*, 26(8):2335–42, Feb 2006.

[148] J B Thorpe, N Rajabi, and D Decatanzaro. Circadian rhythm and response to an acute stressor of urinary corticosterone, testosterone, and creatinine in adult male mice. *Horm Metab Res*, 44(6):429–35, Jun 2012.

[149] Carla Mucignat-Caretta, Michela Bondì, and Antonio Caretta. Endocrine status affects bladder size and postvoid residual urinary volume in mice. *Horm Behav*, 46(1):11–8, Jun 2004.

[150] A Coquelin and F H Bronson. Release of luteinizing hormone in male mice during exposure to females: habituation of the response. *Science*, 206(4422):1099–101, Nov 1979.

[151] Denys deCatanzaro, Elliott A Beaton, Ayesha Khan, and Emily Vella. Urinary oestradiol and testosterone levels from novel male mice approach values sufficient to disrupt early pregnancy in nearby inseminated females. *Reproduction*, 132(2):309–17, Aug 2006.

[152] Hannah A Arnson and Timothy E Holy. Chemosensory burst coding by mouse vomeronasal sensory neurons. *J Neurophysiol*, 106(1):409–20, Jul 2011.

[153] S Segovia, R Paniagua, M Nistal, and A Guillamon. Effects of postpuberal gonadectomy on the neurosensorial epithelium of the vomeronasal organ in the rat. *Brain Res*, 316(2):289–91, Jun 1984.

[154] A Guillamón, S Segovia, and A del Abril. Early effects of gonadal steroids on the neuron number in the medial posterior region and the lateral division of the bed nucleus of the stria terminalis in the rat. *Brain Res Dev Brain Res*, 44(2):281–90, Dec 1988.

[155] Ningdong Kang, Amy Janes, Michael J Baum, and James A Cherry. Sex difference in fos induced by male urine in medial amygdala-projecting accessory olfactory bulb mitral cells of mice. *Neurosci Lett*, 398(1-2):59–62, May 2006.

[156] S Segovia and A Guillamón. Searching for sex differences in the vomeronasal pathway. *Horm Behav*, 30(4):618–26, Dec 1996.

[157] P M Clissold, S Hainey, and J O Bishop. Messenger rnas coding for mouse major urinary proteins are differentially induced by testosterone. *Biochem Genet*, 22(3-4):379–87, Apr 1984.

[158] Arthur P Arnold. The end of gonad-centric sex determination in mammals. *Trends Genet*, 28(2):55–61, Feb 2012.

[159] 2013.

[160] Yoh Isogai, Sheng Si, Lorena Pont-Lezica, Taralyn Tan, Vikrant Kapoor, Venkatesh N Murthy, and Catherine Dulac. Molecular organization of vomeronasal chemoreception. *Nature*, 478(7368):241–5, Oct 2011.

[161] Fulvio Celsi, Anna D'Errico, and Anna Menini. Responses to sulfated steroids of female mouse vomeronasal sensory neurons. *Chem Senses*, Aug 2012.

[162] Pablo Chamero, Trese Leinders-Zufall, and Frank Zufall. From genes to social communication: molecular sensing by the vomeronasal organ. *Trends Neurosci*, 35(10):597–606, Oct 2012.

[163] Hannah A Arnson and Timothy E Holy. Robust encoding of stimulus identity and concentration in the accessory olfactory system. *J Neurosci*, 33(33):13388–97, Aug 2013.

[164] Michael J Baum and Julie Bakker. Roles of sex and gonadal steroids in mammalian pheromonal communication. *Front Neuroendocrinol*, 34(4):268–84, Oct 2013.

[165] Diana E Pankevich, Michael J Baum, and James A Cherry. Olfactory sex discrimination persists, whereas the preference for urinary odorants from estrous females disappears in male mice after vomeronasal organ removal. *J Neurosci*, 24(42):9451–7, Oct 2004.

[166] M Meredith and R J O'Connell. Efferent control of stimulus access to the hamster vomeronasal organ. *J Physiol*, 286:301–16, Jan 1979.

[167] Illya I Tolokh, Xiaoyan Fu, and Timothy E Holy. Reliable sex and strain discrimination in the mouse vomeronasal organ and accessory olfactory bulb. *J Neurosci*, 33(34):13903–13, Aug 2013.

[168] Lisa Stowers and Darren W Logan. Sexual dimorphism in olfactory signaling. *Curr Opin Neurobiol*, 20(6):770–5, Dec 2010.

[169] H M BRUCE. An exteroceptive block to pregnancy in the mouse. *Nature*, 184:105, Jul 1959.

[170] Carsten K Pfeffer, Mingshan Xue, Miao He, Z Josh Huang, and Massimo Scanziani. Inhibition of inhibition in visual cortex: the logic of connections between molecularly distinct interneurons. *Nat Neurosci*, 16(8):1068–76, Aug 2013.

[171] Jessica A Gorski, Tiffany Talley, Mengsheng Qiu, Luis Puelles, John L R Rubenstein, and Kevin R Jones. Cortical excitatory neurons and glia, but not gabaergic neurons, are produced in the emx1-expressing lineage. *J Neurosci*, 22(15):6309–14, Aug 2002.